Division of Solid Mechanics

ISRN LUTFD2/TFHF--05/5112--SE (1-132)

MICROMECHANICAL MODELING OF THERMOSET POWDER COATINGS USING FINITE ELEMENT ANALYSIS

Master's Dissertation by

PER JUNESTAM

Supervisors
Kristofer Gamstedt, Div. of Solid Mechanics, KTH
Matti Ristinmaa, Div. of Solid Mechanics, LTH
Daniel Ståhlberg, Scania CV AB

Copyright © 2005 by Div. of Solid Mechanics (LTH),
Dep. of Solid Mechanics (KTH),
Scania CV AB and
Per Junestam
Printed by KFS AB, Lund, Sweden.

For information, address:
Division of Solid Mechanics, Lund University, Box 118, SE-221 00 Lund, Sweden.
Homepage: http://www.solid.lth.se

ABSTRACT

To paint objects by using powder coatings, which have generally very good properties, is a widely used method within the industry. Studies have showed, however, that a screw joint reinforcement consisting of pre-coated components may, if the coating is not used properly, lose its clamping force, which might lead to fatigue failure of the joint. This is due to relaxation and setting of the powder coating, something that easier occurs at elevated temperatures.

The truck and bus manufacturer Scania CV AB uses a powder coating method to paint the involved components of some screw joint reinforcements and Scania wants to get a better understanding of the problem, which is useful when designing new components and setting the requirements on powder coatings. For this reason Scania started several projects on this subject of which this thesis is one. The aim of this study is to develop a method where the micromechanical properties of the powder coating are simulated using finite element analysis, and then links the micromechanical results with structural performance. This way it is possible to simulate clamping force losses, caused by the coatings, in screw joint reinforcements. The software ABAQUS is used for the finite element analyses.

The outcome of this work shows that it is possible to create this link between micromechanics and structural performance, which is demonstrated in an application where a powder coating layer is applied to an existing finite element model. The study also shows the importance of good material data inputs, which strongly influence the final results and the possibility to perform just comparisons between the simulations and experiments. The simulated results show a good agreement with the experimental results at room temperature, but show larger clamping force losses at elevated temperature. This indicates the existence of some properties of the material that the developed model can not simulate. A number of ideas that could explain this difference are presented in the report and may form the basis for further studies on the powder coatings. Another very interesting continuation of this project is to examine the properties of the binder materials slightly below their glass transition temperatures.

The developed method gives finally a possibility to compare clamping force losses between different combinations of, for example, binder material, filler material, shape of filler particles and to examine the influence of different values of Poisson's ratio, coefficient of thermal expansion etc. All together, this is useful when developing new powder coatings.

SAMMANFATTNING

Inom tillverkningsindustrin är det mycket vanligt att måla komponenter med pulverfärg, på grund av de många goda egenskaper hos den typen av färg. Undersökningar har dock visat att för klämförband vars komponenter har målats innan hopsättningen, finns det risk att klämkraften i förbandet minskar om inte färgen används på rätt sätt. Detta är ett allvarligt problem eftersom minskad klämkraft kan leda till utmattningsbrott i förbandet. Klämkraftsminskningen beror på relaxation och sättning i pulverfärgen och uppkommer främst vid förhöjd temperatur.

Buss och lastbilstillverkaren Scania CV AB använder sig av pulverfärger för att måla komponenterna i vissa skruvförband och därför önskar man få en ökad förståelse för problemet. Detta är viktigt när det gäller utveckling av nya komponenter och bestämning av pulverfärgers krav, och på grund av detta har Scania påbörjat flera projekt, däribland detta examensarbete. Syftet med projektet är att utveckla en metod där de mikromekaniska egenskaperna hos pulverfärger simuleras med finit elementanalys i programmet ABAQUS, och där de mikromekaniska resultaten kopplas ihop med en finit elementmodell på makronivå. På så sätt är det möjligt att simulera klämkraftsförlusten hos ett skruvförband, orsakad av pulverfärgslagren, genom att studera pulverfärgens mikromekaniska egenskaper.

Resultatet av projektet visar att det är möjligt att skapa denna länk mellan mikro- och makronivå, vilket också visas i en tillämpning där ett pulverfärgslager appliceras på en redan befintlig modell. Undersökningen visar även hur viktigt det är med bra materialdata, vilket starkt påverkar resultaten och möjligheten att utföra rättvisa jämförelser mellan simuleringar och experiment. De simulerade resultaten visar god överensstämmelse med de experimentella resultaten vid rumstemperatur, medan de visar större klämkraftsförluster vid hög temperatur. Detta tyder då på någon egenskap hos materialet som den utvecklade modellen inte kan simulera. En rad idéer till denna skillnad presenteras i rapporten och kan ligga till grund för fortsatta studier av pulverfärgerna. En mycket intressant fortsättning på det här projektet är dessutom att undersöka bindemedlens egenskaper strax under deras glastemperaturer.

Den utvecklade metoden ger slutligen en möjlighet att jämföra klämkraftsförluster mellan olika kombinationer av t.ex. bindemedel, fyllmedel, form på fyllmedelspartiklar samt undersöka effekterna av olika Poissons tal, värmeutvidgningskoefficient etc. Tillsammans är allt detta användbart vid framtagning av nya pulverfärger.

PREFACE

This thesis is the final assignment for the examination as Master of Science in Mechanical Engineering at the Institute of Technology in Lund, Sweden. The work was initiated by Scania CV AB in Södertälje, in collaboration with the Department of Solid Mechanics at the Royal Institute of Technology in Stockholm where the greater part of the work was carried out.

Lund in April 2005

Per Junestam

CONTENTS

1 INTRODUCTION

The traditional way to improve durability, appearance and resistance from the environment is to protect the object with some kind of coating, i.e. a protective layer. Traditionally, the most common manner was to use liquid coatings (i.e. wet paints). Recently, the powder coating method, with its many advantages, has become more and more adopted in the industry. Powder coating is the process of coating a surface in which a powder material is applied using an electrostatic method. The applied powder is then heated to its melting point, after which it flows to form a smooth film and then heated further to initiate curing, resulting in a firm, durable finish [1, 2]. Figure 1.1 shows a schematic representation of the different layers that normally cover the object, with the powder coating layer on top.

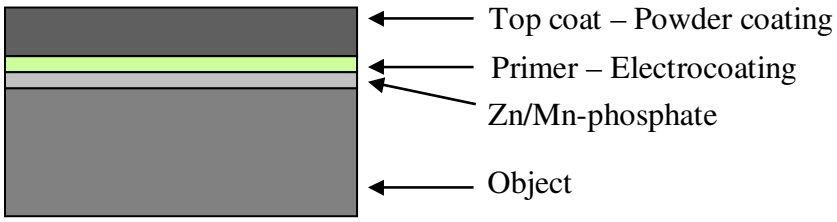

Figure 1.1 Object and protective layers

To save time in the manufacturing process and to improve the properties of objects, Scania applies coatings on objects before they are assembled into final products [2]. This is particularly used in products consisting of large structures, like chassis of buses and trucks. The powder coatings may have excellent properties in some fields but studies at Scania have showed that the coatings may impair the mechanical properties of the construction, if the coating is not used properly.

One such device is the screw joint reinforcement, which is a very important component of the structure. As seen in figure 1.2, screw joint reinforcements are extensively used in the chassis structure of the truck and play an important role of both the global and local performance of the chassis. The screw reinforcement can be used as a load carrying member of the chassis and as a support for smaller components, for example fuel tanks.

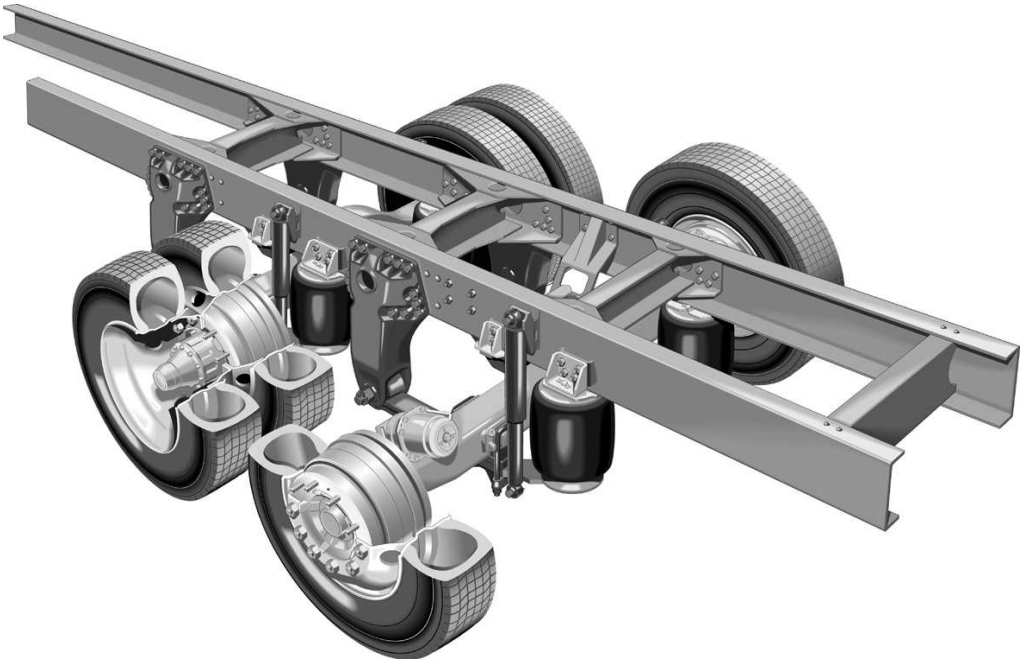

Figure 1.2 Truck chassis, containing several screw joint reinforcements

The screwed or bolted joint must withstand high forces during its lifetime, and it is very important that these high forces can be kept during the entire lifetime of the joint. Figure 1.3 shows a schematic representation of a screw joint reinforcement that is exposed to external loads, such as shear and tensile load [3].

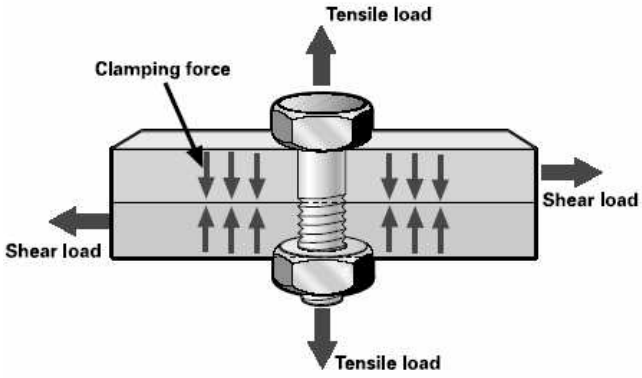

Figure 1.3 Schematic representation of a screw joint reinforcement [3]

The most important factor in a screw joint reinforcement is the clamping force. The external shear loads are not supported by the screw but by the friction between the two plates and the clamping force. If the clamping force decreases, the screw joint reinforcement may get loose, leading to fatigue failure of the screw with serious consequences.

If the two plates involved in the screw joint reinforcement in figure 1.3 were painted before being assembled, two layers of powder coating will be in contact with each other. These coatings must also withstand the stress; otherwise the clamping force may decrease.

The studies at Scania showed that some coatings might set with time, especially at elevated temperatures, which decreases the clamping force in the joint. The setting is explained by the relaxation of the powder coating, a phenomenon that occurs to all viscoelastic materials, for example polymers that are used in these powder coatings.

Therefore, Scania started a project with the aim to get a better understanding of the powder coatings and among other things be able to predict the mechanical behavior of the coatings. Studies within the chemical field as well as the macromechanical field were performed, and later there was a request for a study of the micromechanical properties of the coatings. This request forms the basis of the present work that came up by collaboration between the department of Materials Technology at Scania and the Department of Solid Mechanics at the Royal Institute of Technology in Stockholm, where the greater part of this work was done with docent Kristofer Gamstedt as supervisor. External supervisor at Scania was Daniel Ståhlberg who also acted as a continuous discussion partner throughout the project.

1.1 OBJECTIVES

The aim of this work is to examine the micromechanical properties of coatings using finite element analysis and later on use the micromechanical results in models on a macromechanical level. This line of thought is illustrated below in figure 1.4 and will be explained further in the theoretical part of this report.

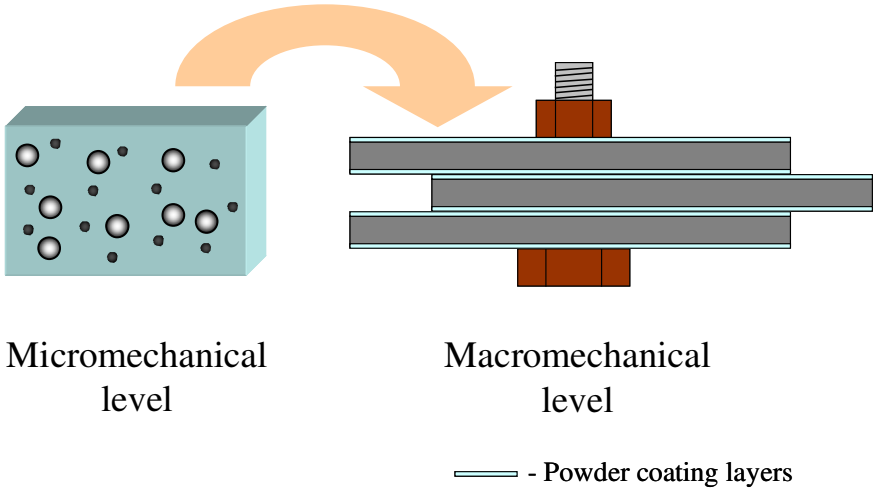

Figure 1.4 Illustration of the main aim of this thesis; to link simulated micromechanical material properties with models

One can say this far that it is not generally practicable to combine micromechanical models with macromechanical models on a large scale due to the tremendously high computation costs this would lead to. Instead, one is interested in finding a way between a relatively simple micromechanical model and a model of an object on a macromechanical level, for example a screw joint reinforcement. The wish is to use the results from the simplified micromechanical model as material properties in the screw joint reinforcement as shown in figure 1.4. This way, the model of the screw joint reinforcement is not much more complex than it was without the added layers of coating.

The first task is consequently to simulate the properties of the coatings on a micromechanical level and to compare the results with experimentally obtained results. The following task is to transform the constitutive properties of the microstructure and assign them to a homogeneous monolithic material, i.e. a continuum object to be used in a finite element (FE) model. By that moment it should be possible to do FE simulations of the coatings on a macromechanical level, i.e. to simulate the loss in clamping force in a screw

joint reinforcement. The simulated results will then be compared to results from real experiments performed at Scania. If the results agree to one another, the simulations make a good description of the mechanical behavior of the powder coating. To get a more practical approach within this thesis, this method will finally be applied to an FE model that is already in use at Scania.

Finally it will be possible to change parameters of the micromechanical model, such as size, shape and material data of the components in the coatings to obtain new elastic material parameters of the coating configuration and examine how it performs in the macromechanical model. This way it should be possible to examine different coatings and determine the best combination for a coating, to make it as capable as possible to withstand the stress in the screw joint reinforcement and keep a high clamping force.

1.2 OUTLINE OF THE REPORT

Chapter 2 treats the theories that form the basis of this work. It begins with information on general subjects such as powder coatings and linear viscoelasticity and continues with the specialized ideas for this study, namely the assumed micromechanical properties of the powder coating and the methods on how to simulate the viscoelastic properties of the powder coating.

Chapter 3 describes how the theories and ideas were implemented and transformed into methods that simulate the micromechanical behavior of the powder coatings and simulate clamping force loss measurements. Finally a case is shown where the developed method is applied to an existing finite element model.

Chapter 4 presents the simulated results and compares them with experimental results where such results are available. The simulated micromechanical results are presented first, followed by clamping force loss simulations.

The notations are presented in the end of this report, and also a glossary with some explained terms related to finite element analysis, which might be useful for the reader.

2 THEORY

The theoretical part treats some general subjects like powder coatings and viscoelasticity as well as some more specialized thoughts and theories that are used in this thesis.

2.1 POWDER COATINGS IN GENERAL

Powder coatings may be thermoplastics or thermosets but in this study, only the latter will be considered because of its generally better performance against chemicals, heat, wear and stress [2].

Thermoset powder coatings contain five major elements, namely: resin, curing agent, filler, pigments and additives. Resin and curing agent form the binder, which is the backbone of the coating and defines many of its properties, and is therefore a very important component of the powder coating. The binder works as a polymer matrix structure that has viscoelastic properties.

The filler consists of particles that are included in the coating, mainly to reduce the cost because of its lower price. The size, shape and chemistry of the filler affect the total performance of the coating and the particles may act as reinforcements. Pigments and additives are added to give the coating certain properties, such as a specific color, hardness, etc. Figure 2.1 shows a picture of the cross-section of a powder coating containing 25% of filler. The sample is embedded in a dark plastic that is shown at the top of the picture while the grey section at the bottom is the steel object. The light grey particles are filler particles surrounded by the polymer matrix and the thickness of the coating is approximately 120 µm.

A schematic representation of a powder coating on microlevel is shown in figure 2.2, showing the binder as a matrix surrounding larger filler particles and smaller pigment particles.

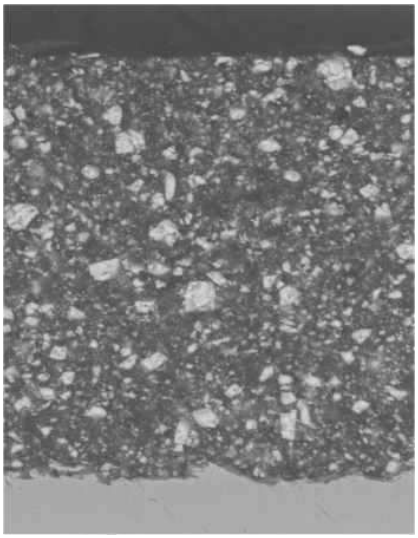

Figure 2.1 Picture showing the cross-section of a powder coating, thickness is approximately 120 µm

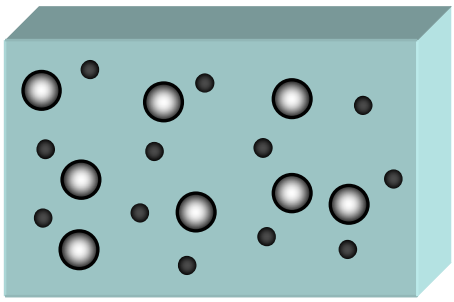

Figure 2.2 Schematic representation of a powder coating, showing the binder matrix surrounding the larger filler particles and smaller pigments

2.2 LINEAR VISCOELASTICITY

Viscoelasticity has been given its own section in the report since the powder coatings contain polymer materials that show viscoelastic properties. There are many sources about linear viscoelasticity and the references [4] to [8], which were used for this study, are some of them.

The theory of viscoelasticity describes the relation between stresses and deformations with respect to time in materials that show both elastic and viscous effects. The material behaves therefore like an elastic material in the beginning of a deformation but has also a time-dependent stress response to the deformation. A viscoelastic material acts like an elastic material in the beginning when a load or a strain is applied to the object. With time, the polymer chains reorganize within the material and the stress within the object decreases until an equilibrium state is reached, and the material has now relaxed.

One example of a viscoelastic behavior is the creep behavior that occurs for example when a heavy load is applied to a plastic bag. Although the load is constant, the handles of the bag extend and may finally break. The corresponding behavior when a strain, instead of a load, is kept constant is called relaxation, which is the case for the screw joint reinforcement. That is to say the stress in the object decreases although the deformation is constant.

A schematic diagram of a relaxation curve can be seen in figure 2.3 below, where the left figure shows the applied strain that is kept constant while the right figure shows how the elastic modulus of the material relaxes.

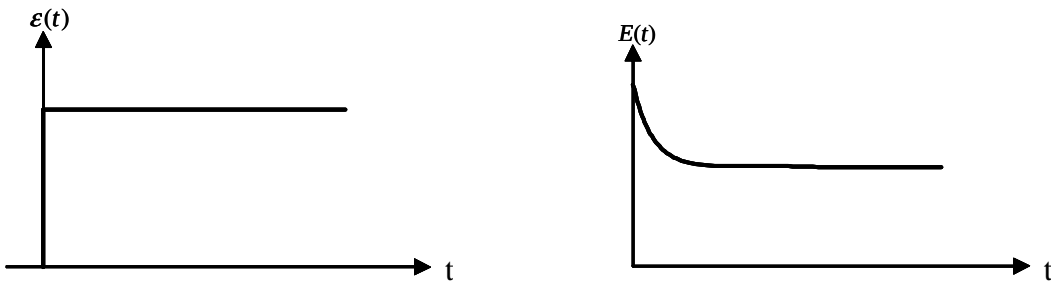

Figure 2.3 Relaxation curve of the elastic modulus to the right and its corresponding strain curve to the left.

Although the examined binder material in this study may have non-linear viscoelastic effects in reality, it will be approximated as a linear viscoelastic material. The main reason for this simplification is the insufficient data on the polymer material. The data is not accurate enough to fully describe the non-linear viscoelastic behavior. Non-linear viscoelasticity would also add a large number of parameters making it a task too complex for this study. Another reason to use linear viscoelastic theory is the fact that the strains are small for the application. In this regime the polymer is linearly viscoelastic. This assumption will give a simpler model and less calculation costs but will hopefully still deliver results with sufficient accuracy. The binder is also assumed to show isotropic behavior.

2.2.1 Viscoelastic models

Material models consisting of springs and dampers, where the spring represents the elastic behavior and the damper represents the viscous behavior of the material, can describe viscoelasticity.

The model used to describe a material should be as simple as possible, yet have a sufficient accuracy. The simplest models are the Maxwell and Kelvin models, shown in figure 2.4.

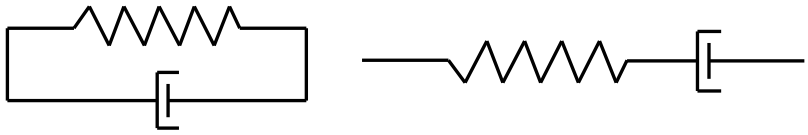

Figure 2.4 Kelvin model to the left and Maxwell model to the right

The Maxwell model works fine in the beginning of a relaxation test, as it is capable of handling instantaneous strains. It cannot, however, represent the long-term elasticity, i.e. the elastic modulus after a long time when the stresses are in equilibrium. The Kelvin model, on the other hand, can express the long-term elastic modulus but it cannot handle an instantaneous strain since the damper is infinitely stiff when a sudden strain is applied.

When none of these two models alone are sufficiently accurate they can be used as units in a larger model. One such example is the Standard Linear Solid model, shown in figure 2.5.

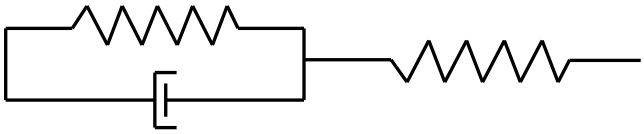

Figure 2.5 Standard Linear Solid model

In the present case, an even higher accuracy is desired. To obtain this accuracy more Maxwell units can be added in parallel as seen in figure 2.6. This model is called the generalized Maxwell model and the FE program, named ABAQUS, which is used in this study, uses the same model to describe viscoelastic properties of materials.

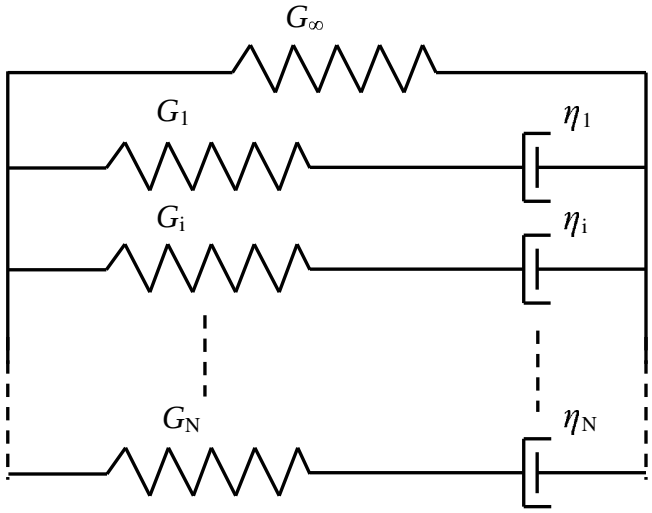

Figure 2.6 The generalized Maxwell model

The generalized Maxwell model consists of an arbitrary number of rows with springs and dampers, 1…*N*, and one chooses the number that gives a sufficient accuracy. ABAQUS supports a maximum of 13 rows. G_∞ denotes the equilibrium shear modulus, i.e. the shear modulus that takes effect after a long period of time when all dampers are drawn out and the material has lost its viscous properties.

2.2.2 Viscoelasticity in uniaxial tension

In a uniaxial relaxation test, the test specimen is exposed to a constant strain ε_0, at time $t = 0$ and the stress is then measured as a function of time. The stress can then be described as:

$$\sigma(t) = \varepsilon_0 E(t) \tag{2.1}$$

where $E(t)$ is the relaxation modulus.

For infinitesimally small time increments $\Delta\tau$, the stress to an arbitrary strain history is given by:

$$\sigma(t) = \int_{0-}^{t} E(t-\tau)\frac{d\varepsilon}{d\tau}d\tau \tag{2.2}$$

2.2.3 Viscoelasticity in multiaxial loading

Since the powder coatings are exposed to loads in all dimensions, multiaxial viscoelastic constitutive laws must be defined. In a general isotropic elastic case, the stiffness tensor can be divided into two parts, one hydrostatic and one deviatoric part. Then the stiffness of a linear isotropic material is defined by:

$$\mathbf{s} = 2G\,\mathbf{D}_s^{-1}\mathbf{e} \tag{2.3}$$

and

$$\sigma_h = K\varepsilon_v \tag{2.4}$$

In the elastic case, the shear and bulk modulus found in equations 2.3 and 2.4 are respectively defined as:

$$G = \frac{E}{2(1+\nu)} \tag{2.5}$$

and

$$K = \frac{E}{3(1-2\nu)} \tag{2.6}$$

In equation 2.3, **s** denotes the stress deviator vector, **e** the strain deviator vector and $\mathbf{D}_s$ a diagonal matrix that describes the relations between the elements in the s and e vectors, respectively. The relative volume change and hydrostatic stress in equation 2.4 are defined by $\varepsilon_v = \varepsilon_x + \varepsilon_y + \varepsilon_z$ and $\sigma_k = (\sigma_x + \sigma_y + \sigma_z)/3$, respectively. The shear modulus, G (equation 2.5), and bulk modulus, K (equation 2.6), are expressions that depend only on Young's modulus E and Poisson's ratio ν.

By using equations 2.3 and 2.4 above and to assume that the binder is made of an isotropic material, this leads to the multiaxial viscoelastic constitutive laws:

$$\mathbf{s}(t) = \int_{0-}^{t} 2G(t-\tau)\mathbf{D}_s^{-1}\frac{d\mathbf{e}}{d\tau}d\tau \tag{2.7}$$

and

$$\sigma_h(t) = \int_{0-}^{t} K(t-\tau)\frac{d\varepsilon_v}{d\tau}d\tau \tag{2.8}$$

where $G(t)$ and $K(t)$ now denote the time-dependent shear and bulk relaxation moduli, respectively.

The corresponding relations in tensor notation read respectively:

$$s_{ij}(t) = \int_{0-}^{t} 2G(t-\tau)\frac{de_{ij}}{d\tau}d\tau \tag{2.9}$$

$$\sigma_{kk}(t) = \int_{0-}^{t} 3K(t-\tau)\frac{d\varepsilon_{kk}}{d\tau}d\tau \tag{2.10}$$

For the special case of constant strain these equations can be written in the following way:

$$s_{ij}(t) = 2G(t)e_{ij} \tag{2.11}$$

and

$$\sigma_{kk}(t) = 3K(t)\varepsilon_{kk} \tag{2.12}$$

The shear modulus $G(t)$ can be interpreted as the relaxation modulus for shear stress and the bulk modulus $K(t)$ as the relaxation modulus for hydrostatic stress.

2.3 MICROMECHANICS

The contribution to the mechanical behavior of the pigments and additives are minor compared to those of the binder and filler, and their influence will therefore be neglected in the micromechanical model. With these assumptions, the micromechanical appearance of the powder coating can be simplified to a composite consisting of only the binder as matrix material and the filler as particles surrounded by the matrix, see figure 2.7.

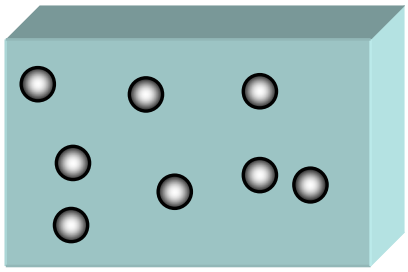

Figure 2.7 Schematic representation of the simplified powder coating consisting of a binder matrix and filler particles

The powder coating is assumed to globally show an isotropic behavior. Of course the filler particles may collect in lumps causing higher concentrations locally, but since the filler particles are randomly distributed within the binder the assumption of isotropic behavior should be acceptable. The already simplified micromechanical representation is simplified further by being homogenized to meet the criterion of isotropic behavior. In this case the homogenization is done by distributing the filler particles evenly within the binder and giving all particles the same shape and size. Figure 2.8 shows the final micromechanical representation after homogenization, which is valid for all directions.

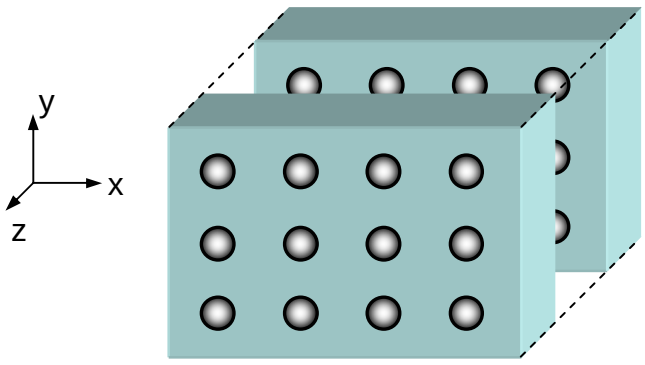

Figure 2.8 Representation of the homogenized powder coating consisting of a

Since the powder coating is assumed to be homogenized, the elastic properties for one small part of the coating are the same as for the whole coating. Consequently, next step is to isolate a small part of this micromechanical model, i.e. a unit cell.

The unit cell must have a shape that allows it to build up a lattice of unit cells that creates the same model as in figure 2.8. The simplest shape that fulfills this criterion is the cubical shape, seen in figure 2.9. By dividing the homogenized micromechanical model in equally sized cubes and finally isolate one cell, the final micromechanical model that will be used in this study is obtained, which is shown in figure 2.10.

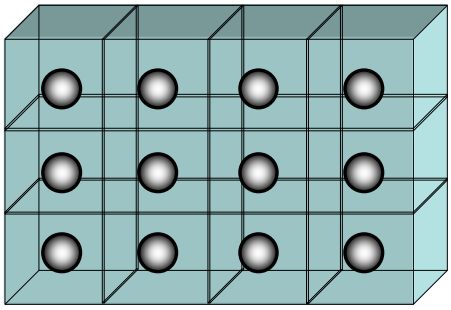

Figure 2.9 Micromechanical structure divided into cubical unit cells

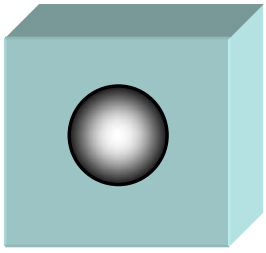

Figure 2.10 The unit cell that will be used in the micromechanical simulations

As seen in figure 2.10 the unit cell consists of a cubical matrix containing the binder material, and the matrix has a spherical void in its center where the filler particle is located. The spherical shape of the filler particle functions as an average shape of all the real randomly shaped filler particles that exist in the powder coatings. When looking at elastic properties only, the exact shape of the filler particle has a minor role. A case where the particle has a cubical shape was examined but not presented in this report. The examination

showed, however, that the percentage difference in the final results was much lower than the distribution of the experimental material measurements. Therefore, the assumption of a spherical particle is acceptable.

One of the aims is to examine the influence of increased particle volume concentration (PVC), by varying the total volume percentage of the filler. It is important to consider that there is no length factor involved in this elastic model. Figure 2.11 shows two representations of powder coatings containing the same total amount of PVC, but the powder coating A to the left contains more particles than powder coating B to the right.

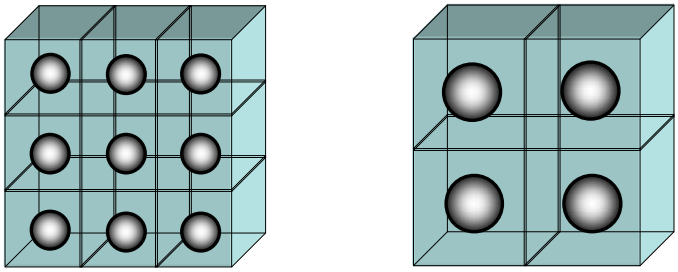

Figure 2.11 Two representations of powder coatings with PVC = 20% but with different number of particles

Since the filler particle is assumed to be perfectly attached to the matrix, powder coating A would, in reality, have better performance than coating B. This is a result of the ratio between the surface area and volume of the filler particle, which is increased with decreased size of the filler particle. Together with the assumption of perfect adhesion this would give rise to a stiffening effect from the interaction between the filler particle and binder. But while staying within the elastic case, a unit cell from powder coating A shows the same elastic properties as a unit cell from powder coating B. This discussion consequently leads to the fact that varying the PVC in the model is the same as varying the size of the spherical particle.

2.3.1 Boundary conditions for the unit cell

While the cubical unit cell is undeformed it is clearly a part of the lattice that builds up the imagined structure of the powder coating, shown in figure 2.9. The unit cell must also fulfill this criterion while it is deformed, i.e. it must still be a part of a continuous lattice that builds up the powder coating structure although the unit cell is deformed.

This criterion is fulfilled by periodic boundary conditions, which means that two opposite surfaces of the unit cell deform equally and this is a criterion for all six surfaces of the cube. This way one unit cell will always fit to its neighbor if they are placed adjacently to each other, and will consequently be able to build up the required structure.

The discussion of boundary conditions of the unit cell is done in the section treating the simulations of the unit cells, namely sections *3.1.1 Final micromechanical models* and *3.1.2.4 Boundary conditions*. The general idea is, however, that the unit cell should be able to act as naturally as possible, i.e. have as few constraints as possible. Periodic boundary conditions function also like constraints but are necessary. The finite element analysis also needs certain constraints to make calculations viable. Consequently the result of this must lead to a compromise that is believed to fulfill all criterions.

2.3.2 Material properties of the filler

The filler material used in this study is barium sulphate, $BaSO_4$, also called barite. Barite has an orthorhombic crystal structure that gives it anisotropic elastic properties, but is assumed to have isotropic elastic properties when the material forms a polycrystalline structure.

2.3.2.1 Elastic properties

Barite has an orthorhombic structure that gives a single crystal nine different elastic constants. The elastic constants, which can be found in [9], are tabulated below in table 2.1.

Table 2.1 Single crystal elastic constants (c_{ij}) for barite, $BaSO_4$ [9]

c_{ij}	(10^{11} Pa)
c_{11}	0.8941
c_{22}	0.7842
c_{33}	1.0548
c_{44}	0.1190
c_{55}	0.2874
c_{66}	0.2778
c_{12}	0.4614
c_{13}	0.2691
	0.2676

The average isotropic elastic modulus E is calculated from the anisotropic single crystal elastic constants (c_{ij}). The Voigt and Reuss assumptions result in the theoretical maximum and minimum values of the isotropic elastic modulus, respectively [10].

For an orthorhombic crystal like barite, the Voigt shear modulus G_V and bulk modulus K_V are given respectively by:

$$G_V = \frac{1}{15}(c_{11} + c_{22} + c_{33} - c_{12} - c_{13} - c_{23}) + \frac{1}{5}(c_{44} + c_{55} + c_{66}) \qquad (2.13)$$

and

$$K_V = \frac{1}{9}(c_{11} + c_{22} + c_{33}) + \frac{2}{9}(c_{12} + c_{13} + c_{23}) \qquad (2.14)$$

The expressions for the Reuss shear modulus G_R and bulk modulus K_R are the following:

$$G_R = \frac{15}{4(s_{11} + s_{22} + s_{33}) - 4(s_{12} + s_{13} + s_{23}) + 3(s_{44} + s_{55} + s_{66})} \qquad (2.15)$$

and

$$K_R = \frac{1}{s_{11} + s_{22} + s_{33} + 2(s_{12} + s_{13} + s_{23})} \qquad (2.16)$$

where s_{ij} are the elastic compliance constants.

The matrix for the compliance constants, S, is expressed as:

$$\mathbf{S} = \begin{bmatrix} c_{11} & c_{12} & c_{13} & 0 & 0 & 0 \\ c_{12} & c_{22} & c_{23} & 0 & 0 & 0 \\ c_{13} & c_{23} & c_{33} & 0 & 0 & 0 \\ 0 & 0 & 0 & c_{44} & 0 & 0 \\ 0 & 0 & 0 & 0 & c_{55} & 0 \\ 0 & 0 & 0 & 0 & 0 & c_{66} \end{bmatrix}^{-1} \qquad (2.17)$$

For an isotropic material, Young's modulus, E, and Poisson's ratio, v, are given respectively by:

$$E = \frac{9KG}{3K + G} \tag{2.18}$$

and

$$v = \frac{3K - 2G}{2(3K + G)} \tag{2.19}$$

The best estimation for the average values of G and K would then be the arithmetic means of the extremes, i.e. the average values of the Voigt and Reuss moduli, which consequently are expressed as:

$$G = \frac{G_V + G_R}{2} \tag{2.20}$$

and

$$K = \frac{K_V + K_R}{2} \tag{2.21}$$

It is now possible to calculate the elastic properties of the barite filler particles and use them as input parameters in the FE analysis.

2.3.3 Material properties of the binder

The binder material of the examined powder coating is a cross-linked polyester, more precisely a saturated thermoset, and belongs to the category of polymer materials. Polymers show viscoelastic behavior and viscoelasticity is treated in section 2.2 of this report. In this section only the theory on how to determine the viscoelastic parameters of the binder will be discussed.

2.3.3.1 Viscoelastic properties

ABAQUS requires a number of parameters to describe the viscoelastic behavior of a material and they are divided in an elastic part and a viscous part.

The elastic part consists of the initial elastic modulus, E_0, and the initial value of Poisson's ratio, v_0. The viscous part requires a description of the relaxation of the bulk modulus, K, or the shear modulus, G, or both of them. It should be remembered that among the four parameters; E, G, K and v, only two can be independent, see [11] for example.

Since the test specimens are thin layers relaxation of the material is measured in uniaxial tension tests and the relaxation modulus for uniaxial load, $E(t)$, is consequently obtained. The initial value of Poisson's ratio is known from an earlier study [12]. The same study also showed that the value may differ and different values of Poisson's ratio will therefore be examined.

Many polymers, however, show a much larger viscoelastic effect in shear compared to compression [13, 14]. A good approximation would therefore be to assume that K is time-independent, i.e. K takes a constant value $K = K_0$ where K_0 is given by the expression for K using the initial values of Young's modulus E_0 and Poisson's ratio, v_0:

$$K_0 = \frac{E_0}{3(1-2v_0)} \tag{2.22}$$

This equation also shows that if K is time-independent and E is time-dependent, $E(t)$, then Poisson's ratio must also be time-dependent, i.e. $v(t)$. Poisson's ratio can consequently be calculated for any point of time by the following equation:

$$v(t) = \frac{1}{2} - \frac{E(t)}{6K} \tag{2.23}$$

By knowing E and v for any point of time the relaxation curve for the shear modulus, G, can finally be determined from:

$$G(t) = \frac{E(t)}{2(1+v(t))} \tag{2.24}$$

Figure 2.12 shows a typical example of a relaxation curve. The elastic modulus is measured during a uniaxial tension test and is plotted against time. The first dot represents the initial value of the elastic modulus, which is marked in the plot as $E_{0.}$

Following the initial value is an arbitrary number of points of measuring marked E_i, where the index i represents the number of the point of measuring. The curve finally reaches an equilibrium state and its corresponding value is marked as E_∞. If no steady equilibrium state is reached, for example if the asymptote oscillates slightly, one can calculate an equilibrium value as the average value of a series containing the last values.

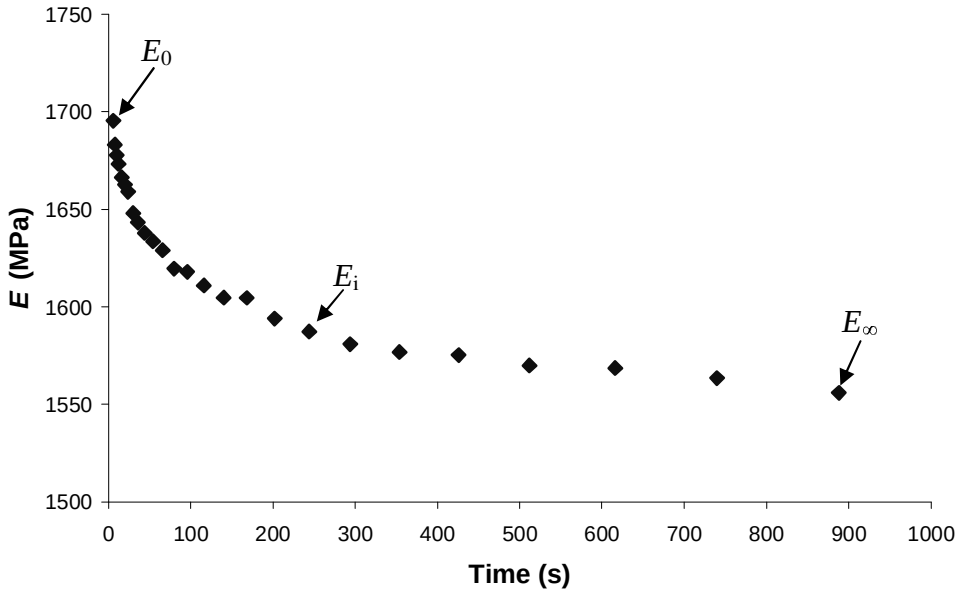

Figure 2.12 Typical relaxation curve created with measurements of the elastic modulus plotted against time

In section *2.2.1 Viscoelastic models*, the generalized Maxwell model was introduced as the model being used by ABAQUS to describe the viscoelastic behavior of a material. Figure 2.6 shows that the relaxation modulus for shear for a viscoelastic material can be expressed as:

$$G(t) = G_0\left[1 - \sum_{i=1}^{N} \alpha_i \left(1 - e^{-t/\tau_i}\right)\right] \tag{2.25}$$

where

$$G_0 = G_\infty + \sum_{i=1}^{N} G_i \tag{2.26}$$

$$\alpha_i = \frac{G_i}{G_0} \tag{2.27}$$

$$\tau_i = \frac{\eta_i}{G_i} \tag{2.28}$$

Equation 2.25 shows that $G(t=0) = G_0$ and $G(t=\infty) = G_\infty$. The appearance of the curve is determined by α_i and τ_i, where the index i represents each point of measuring.

The demanded input parameters to describe relaxation in ABAQUS are α_i for all points of measuring, i.e. the ratio between the shear modulus at a certain point of measuring, G_i, and the initial shear modulus G_0. The corresponding time for every point of measuring and a value for the shear modulus at the equilibrium state are also demanded. No input parameters are required for the bulk modulus since it is defined to be constant, which is fulfilled by E_0 and v_0.

When the ratio and time for each point of measuring is entered, ABAQUS performs a curve fit by adjusting the parameter τ_i for each point of measuring by using the least square method. This results in a time-dependent function that fully describes the relaxation of the binder material and ends up at the equilibrium level, defined in the material input section.

2.3.4 Material properties of extreme binders

Analyses using binder materials that relax extremely little and extremely much will also be performed. The purpose is to find extreme values of the clamping force loss at room temperature. Therefore, an exact representation of the relaxation lapse is not necessary but initial and relaxed values only.

A polymer that relaxes strongly is polypropylene and the following relaxation data can be found in [15]:

$E_{0,\ \text{polypropylene}} = 715$ MPa
$E_{\infty,\ \text{polypropylene}} = 535$ MPa

Poisson's ratio for polypropylene can be found in [16] and is defined as the initial value of Poisson's ratio:

$\nu_{0,\ \text{polypropylene}} = 0.32$

An epoxy polymer is chosen as the second extreme polymer and [17] gives the following relaxation data at room temperature for a degree of cure of 0.89:

$E_{0,\ \text{epoxy}} = 2.80$ GPa
$E_{\infty,\ \text{epoxy}} = 2.67$ GPa

The initial value of Poisson's ratio for the epoxy polymer is assumed to be:

$\nu_{0,\ \text{epoxy}} = 0.38$

2.4 VISCOELASTIC PROPERTIES OF THE POWDER COATING

The constitutive properties of each component, i.e. the binder and filler, are quite easily obtained but the constitutive properties of the powder coating, i.e. the composite, are not known. Of course one can carry out experimental measurements of the powder coatings to obtain the desired material data but the wish is to be able to do this by simulations instead. That would save time and make it easier to obtain new material configurations. This section explains the idea on how simulations of the micromechanical model will obtain these constitutive properties.

As concluded earlier, a viscoelastic material has two constitutive laws that describe its viscoelastic properties, namely equations 2.11 and 2.12. The task is consequently to obtain the bulk modulus K and shear modulus G for the material. When they are known, E and v are obtained by equations 2.18 and 2.19. Firstly the method on how to determine the bulk modulus K is presented.

2.4.1 Determination of bulk modulus *K*(t)

The composite will have a time-dependent bulk modulus although the bulk modulus of the viscoelastic binder material is assumed to be time-independent. This is because of the influence of the filler particle that creates shear stresses within the matrix, and the shear modulus is already established as time-dependent.

As declared earlier, the bulk modulus K is interpreted as the relaxation modulus for a hydrostatic case and it will therefore be obtained by a hydrostatic stress or hydrostatic deformation state. When an object made of a homogeneous material is exposed to hydrostatic pressure, it is deformed proportionally. A cube will still have the shape of a cube although the volume is smaller. In this case the cubical cell consists of two different types of material and therefore the surfaces of the cell will not remain plane when it is exposed to hydrostatic pressure. This would interfere with the criterion of cells that must fit to one another since the surfaces would be deformed unequally. This can be avoided by defining constraints that force the plane surfaces to remain plane after deformation.

As seen in equation 2.12 for the bulk modulus, both hydrostatic pressure and relative volume change are used in the expression. Consequently by applying an equally large displacement on each surface in the normal direction of the

after deformation is fulfilled, at the same time as the relative volume change is determined.

By dividing the hydrostatic pressure and the relative volume change into their components, equation 2.12 can be transformed into the following expression for the bulk modulus:

$$K(t)=\frac{\sigma_x(t)+\sigma_y(t)+\sigma_z(t)}{3(\varepsilon_x+\varepsilon_y+\varepsilon_z)} \qquad (2.29)$$

In equation 2.29 one can see that the bulk modulus and the stresses are time-dependent while the deformations are constant. The idea is that the viscoelastic material starts to relax while the displacements in the *x*-, *y*- and *z*-directions are kept constant.

If one looks at the unit cell from the outside, the cell is influenced by hydrostatic pressure, i.e. the pressure is the same on all surfaces. The pressure in the *x*-direction is the same as the stress σ_x at the surface in the *x*-direction. So by measuring the stresses σ_x, σ_y and σ_z at their respective normal surfaces, like figure 2.13 shows, at different points of time and inserting the results in the expression for *K* above (equation 2.29), one should be able to describe the bulk modulus of the unit cell, as seen in the representation in figure 2.14. By intuition the bulk modulus should show weak time dependence.

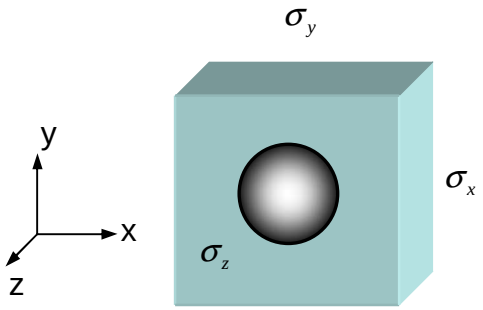

Figure 2.13 Normal stresses indicated at their respective surfaces

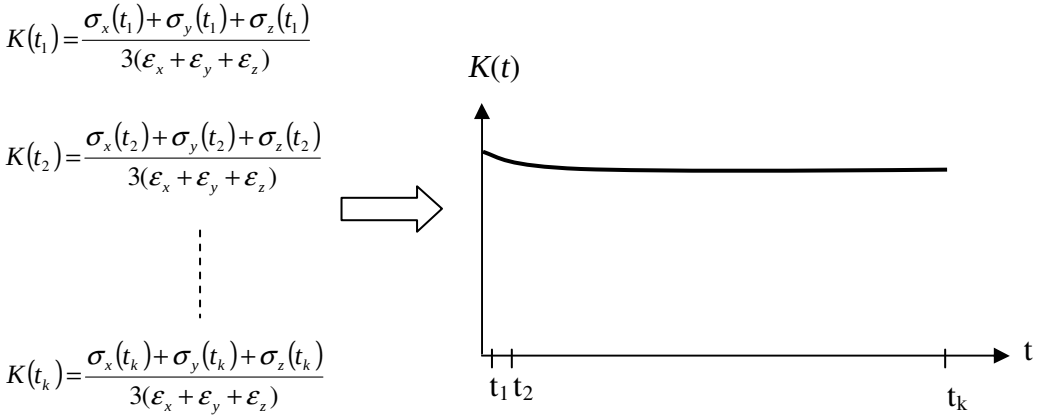

Figure 2.14 Representation of how to obtain the relaxation of the bulk modulus $K(t)$ for the unit cell

2.4.2 Determination of shear modulus *G*(t)

The method to obtain the shear modulus $G(t)$ is based on the same idea as for the bulk modulus, but this time the unit cell is exposed to shear. The boundary condition problem is more complex this time, and will be discussed later in sections *3.1.1 Final micromechanical models* and *3.1.2.4 Boundary conditions.* Here, only the general idea on how to obtain the shear modulus will be presented.

Equation 2.11 that contains the shear modulus contains also the stress and strain deviators s_{ij} and e_{ij}, respectively. If the shear deformation occurs in the *xy*-direction the equation can be expressed as:

$$\tau_{xy}(t) = 2G(t)\varepsilon_{xy} \tag{2.30}$$

and takes the following form as an expression for $G(t)$:

$$G(t) = \frac{\tau_{xy}(t)}{2\,\varepsilon_{xy}} \tag{2.31}$$

The shear strain ε_{xy} in equation 2.31 is given by:

$$\varepsilon_{xy} = \frac{1}{2}\left[\frac{\partial u_x}{\partial x_y} + \frac{\partial u_y}{\partial x_x}\right] \tag{2.32}$$

where u_x and u_y represent the displacements in the x- and y-directions caused by the shear. $G(t)$ would then be obtained by applying a constant shear deformation to the unit cell, measuring the shear stress τ_{xy} and inserting these values into the expression for $G(t)$ (equation 2.31). The shear stress τ_{xy} should have the same magnitude on all four surfaces that are perpendicular to the xy-plane and consequently anyone of them could be investigated with respect to the sign of the magnitude. In figure 2.15 the upper surface in the xz-plane is chosen as an example.

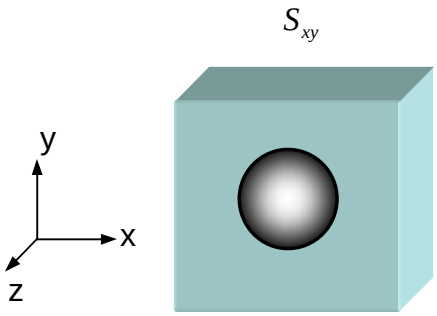

Figure 2.15 One possible surface where to measure the shear stress

Figure 2.16 shows, in the same manner as for the bulk modulus $K(t)$, how the shear modulus $G(t)$ will be obtained. By intuition the shear modulus should show stronger time dependence than the bulk modulus.

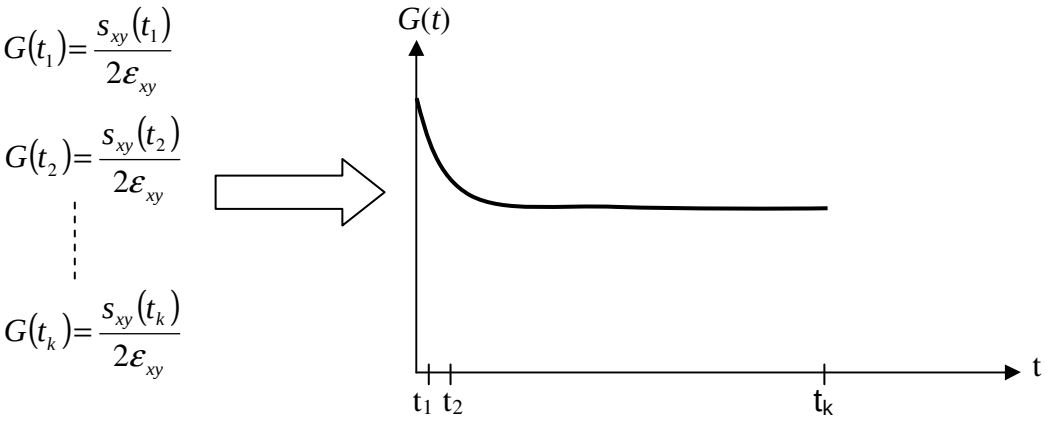

Figure 2.16 Representation of how to obtain the relaxation of the shear modulus $G(t)$ for the unit cell

2.5 COEFFICIENT OF THERMAL EXPANSION FOR THE COMPOSITE

As mentioned in the introductory section, macromechanical simulations will also be performed. Some of these simulations will be performed at increased temperatures and the coefficient of thermal expansion (CTE) for the composite must therefore be calculated.

Schapery developed a thermo elastic model for predicting thermal expansion behavior of particle-reinforced composites. The following expression originates from that model and is used to calculate the CTE for a composite [18]:

$$\alpha_c = \alpha_p + (\alpha_m - \alpha_p) \cdot \frac{\frac{1}{K_c} - \frac{1}{K_p}}{\frac{1}{K_m} - \frac{1}{K_p}} \tag{2.33}$$

where the following parameters are included:

α_c: CTE for the composite
α_p: CTE for the particle
α_m: CTE for the matrix
K_c: Bulk modulus for the composite
K_p: Bulk modulus for the particle
K_m: Bulk modulus for the matrix

For low volume concentrations of fillers (PVC: 10 - 40%) the bulk modulus for the composite can be calculated by solving K_c in the following equation [19]:

$$\frac{K_c - K_m}{K_p - K_m} = c \cdot \left(1 + \frac{(1-c)(K_p - K_m)}{K_m + \frac{4G_m}{3}} \right)^{-1} \tag{2.34}$$

where c represents the particle volume concentration (PVC) and G_m is the shear modulus for the matrix material.

Consequently, K_c can be obtained from equation 2.34 if the particle volume concentration, the elastic modulus K and Poisson's ratio v of the particle and matrix material are known. Finally the coefficient of thermal expansion for the composite can be obtained from equation 2.33.

According to [20] the coefficient of thermal expansion for the filler may be expressed as:

$$\alpha_p(T) = \alpha_0 + \alpha_1 T + \alpha_2 T^{-2} \qquad (2.35)$$

where α_0, α_1 and α_2 are constants determined by fitting experimental data. The same reference gives the corresponding values for the volumetric thermal expansion, which are:

$\alpha_0 = 63.7 \cdot 10^{-6}$
$\alpha_1 = 0$
$\alpha_2 = 0$

Equation 2.35 now defines the volumetric coefficient of thermal expansion for barite to be:

$\alpha_p = 63.7 \cdot 10^{-6} \mathrm{C}^{-1}$

CTE below the glass transition temperature for the polyester binder is found in [21] and is approximated to:

$\alpha_m = 90 \cdot 10^{-6}\ \mathrm{C}^{-1}$

3 METHODS OF ANALYSIS

The following section explains the methods that were used to perform the micromechanical simulations, the clamping force loss simulations and finally the application to an already existing finite element model.

3.1 MICROMECHANICAL SIMULATIONS

The final micromechanical models are settled and are later created as FE models in the software ABAQUS 6.4 Standard. The results from the FE simulations are collected and treated in MATLAB. Reference [22] was mainly used for help on ABAQUS.

3.1.1 Final micromechanical models

The basic appearance of the unit cell is already settled and now two types of models for the finite element analysis need to be settled. To simplify the writing from now on the two models are given easier names. The model that is used to obtain the bulk modulus $K(t)$ will be called *The hydrostatic model* and the model that is used to obtain the shear modulus $G(t)$ will be called *The shear model*.

The hydrostatic model is a quite straightforward case since there is not many alternatives on how to create it. As the unit cell is exposed to hydrostatic deformation, symmetry conditions are used to make the model as simple as possible. Consequently, only one eighth of the unit cell is modeled with symmetry planes on the cut surfaces in the *x*-, *y*- and *z*-directions. The outer surfaces are exposed to equally large displacements in their respective normal directions. This is explained in detail later in section *3.1.2.4.1 Boundary conditions of the hydrostatic model* and can be seen in figures 3.15 and 3.17.

The task to choose a suitable model type for the shear model is more complex and a study of some possibilities is made. A rough selection of appropriate and inappropriate unit cells that fulfills the previous criterions can be made out of intuition. In the following figures; figure 3.1 to figure 3.3 some alternatives are illustrated. The spherical particle has been removed from the unit cells to make the figures more visible.

Plane boundaries

Figure 3.1 shows how the unit cell is exposed to shear deformation by applying positive and negative displacements in the *x*-direction at the two opposite surfaces in the *xz*-plane, respectively. Simultaneously, the two affected surfaces are constrained in the *y*-direction, i.e. they are not allowed to deform in the *y*-direction and will therefore remain plane. The two opposite surfaces in the *yz*-plane remain plane too and they will therefore deform equally and consequently fulfill the criterion of periodic boundary conditions. Small deformations are assumed to occur in the *z*-direction as a result of the shear deformation. Consequently the two opposite surfaces in the *xz*-plane will therefore be assumed to remain plane. With the resulting deformed shape as in figure 3.1 each unit cell would fit next to its neighbor and consequently build up the lattice of unit cells that creates the powder coating microstructure.

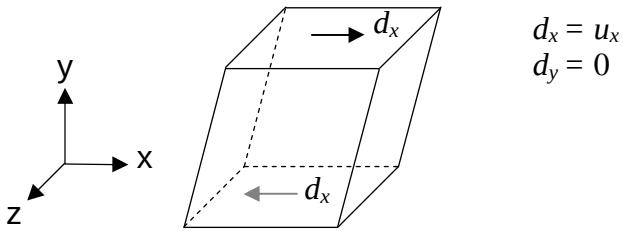

Figure 3.1 Unit cell exposed to shear deformation acting on the two surfaces in the *xz*-plane. Surfaces in the *xz*- and *yz*-planes are constrained to remain plane

Free vertical boundaries

The unit cell in figure 3.2 is exposed to a similar shear deformation as in figure 3.1. This unit cell, however, have no constraints acting on the two opposite surfaces in the *yz*-plane that make them remain plane. Instead they are allowed to deform freely with only one criterion; periodic deformation, i.e. that the two opposite surfaces deform equally. Small deformations are assumed to occur in the *z*-direction as a result of the shear deformation. Consequently the two opposite surfaces in the *xz*-plane will therefore be assumed to remain plane. With the resulting deformed shape as in figure 3.2 each unit cell will fit next to its neighbor and consequently build up the lattice of unit cells that creates the powder coating microstructure.

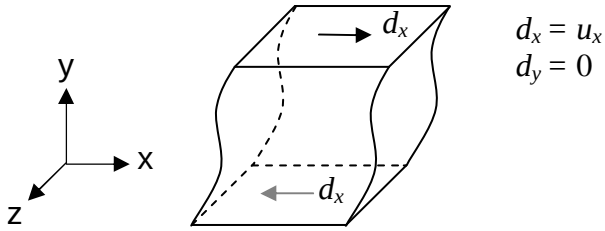

Figure 3.2 Unit cell exposed to shear deformation acting on the two surfaces in the *xz*-plane. Surfaces in the *xz*-plane are constrained to remain plane while the surfaces in the *yz*-plane are constrained by periodic boundary conditions

Free boundaries

The third alternative is shown in figure 3.3. The unit cell is exposed to shear deformation by applying positive respective negative displacements in the *x*-direction at the surfaces in the *xz*-plane, and displacements of the same magnitude but in the *y*-direction at the surfaces in the *yz*-plane. The affected surfaces are, with the exception of periodic boundary conditions, allowed to deform freely. With the assumption of small deformations in the *z*-direction as a result of the shear deformation, the cell will have the deformed shape that is shown in figure 3.3. Consequently the unit cell will fit next to its neighbor and build up the lattice of unit cells that creates the powder coating microstructure.

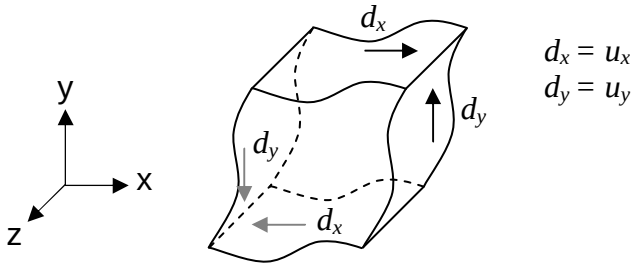

Figure 3.3 Unit cell exposed to shear deformation acting on the four surfaces in the *xz*- and *yz*-planes. The four surfaces are constrained by periodic boundary conditions

By judging these three alternatives the last one seems to act most naturally and is consequently the one that will define the global boundary conditions of the unit cell. If all applied displacements have the same magnitude, all opposite surfaces will deform as good as identically, which is because of the symmetry of the model. The displacements of the opposite nodes on each

side were controlled and the differences were of the size of 0.004%, which is negligible. The same control was made of the opposite nodes on the surfaces in the *xz*-plane and the differences were negligible too; about 0.2%. These errors are smaller than the distribution of the measurement data of the involved materials. Consequently, the desired shape of a unit cell with periodic boundary conditions was obtained without constraints. This is not the case, however, if the particle has an asymmetric shape where constraints are necessary to maintain the appearance of periodic boundaries. The resulting lattice of the deformed unit cell would then have the appearance shown in figure 3.4.

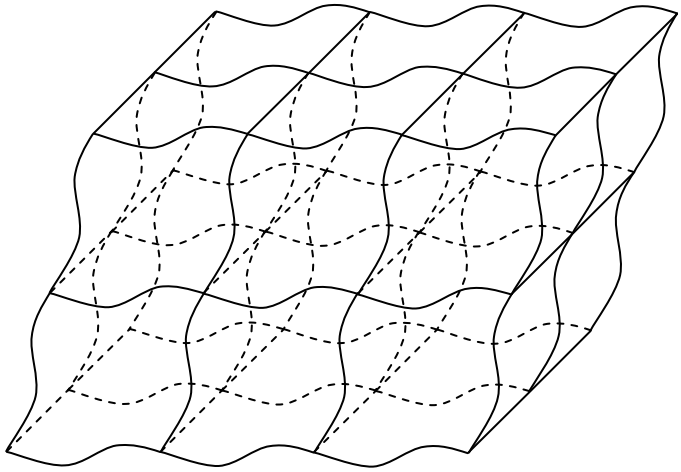

Figure 3.4 Lattice of unit cells representing the coating when the unit cell is exposed to shear deformation. Each surface on one cell fits to the surface of its neighbor

Now the type of boundary conditions is broadly defined. The FE model requires, however, that the model is constrained against rigid body motion such as translation and rotation along and around the *x*-, *y*- and *z*-axes. Since the shear deformation already is defined as displacements in the *x*- and *y*-directions, only one more constraint is needed, namely one in the *z*-direction. Several versions with the aim to make this as suitable and natural as possible are made and the results are presented here. Since the shear stress caused by the shear deformation is the wanted parameter, the behavior of the cell in the *xy*-direction is investigated and the shear stress τ_{xy} for different types of constraints is measured at the top surface of the unit cell like in figure 2.15. The shear deformation is the same for all alternatives, i.e. as in figure 3.3, and is not shown in the figures. Instead the following figures show only the constraints in the *z*-direction. The different alternatives are presented next:

Alternative A

The checked surfaces in figure 3.5 are constrained in the *z*-direction with the result that all edges are constrained in this direction. The two surfaces in the *xy*-plane, however, are free to deform except for their edges.

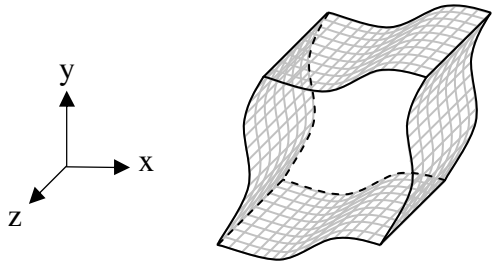

Figure 3.5 Unit cell where checked surfaces are constrained in the *z*-direction

Measured τ_{xy}: 18.50 MPa

Alternative B

This alternative is the same as the previous one with the additional constraints on the two surfaces in the *xy*-plane, as shown in figure 3.6. This way these two surfaces remain plane.

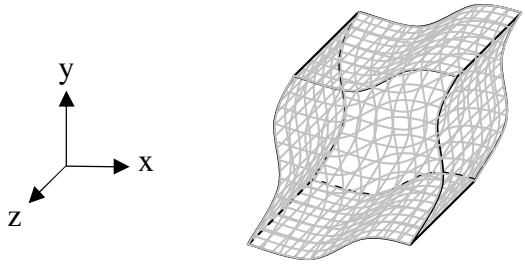

Figure 3.6 Unit cell where all surfaces are constrained in the *z*-direction

Measured τ_{xy}: 18.48 MPa

The cells in alternative A and B are now cut in half by defining a cutting surface in the *xy*-plane as described in figure 3.7, and the displacements in the *z*-direction of the nodes on the cutting plane are measured.

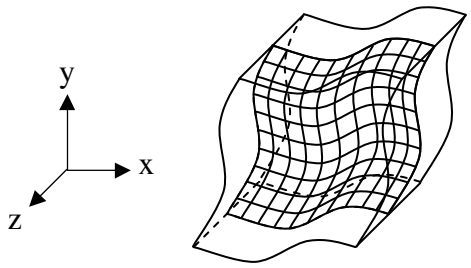

Figure 3.7 Unit cell cut in half by a cutting plane in the *xy*-plane, represented by the checked plane in the figure

Since the nodal displacements are extremely small it would be possible to simplify the model by defining a symmetry plane where the cut is made and consequently examine only one half of the cell. This would decrease the calculation time and since the model is now constrained in the *z*-direction by the symmetry plane, it is possible to test other combinations of boundary conditions. This generates the following alternatives:

Alternative C

The same as alternative A but only one half of the original cell is being used and a symmetry plane is placed in the *xy*-plane defining symmetry conditions in the *z*-direction. This model is shown in figure 3.8.

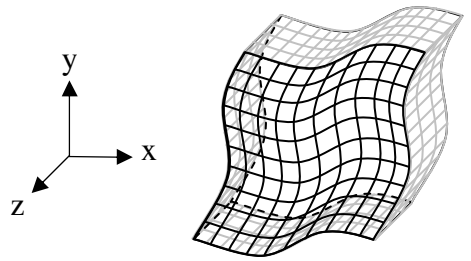

Figure 3.8 Unit cell whose grey-checked surfaces are constrained in the *z*-direction. The black-checked surface represents the symmetry plane

Measured τ_{xy}: 18.46 MPa

Alternative D

The same model as alternative C with the additional constraint on the surface in the *z*-direction that is unconstrained in alternative C. This way, all surfaces

are constrained and the two surfaces in the *xy*-plane remain plane due to the constraint and the defined symmetry conditions, as shown in figure 3.9.

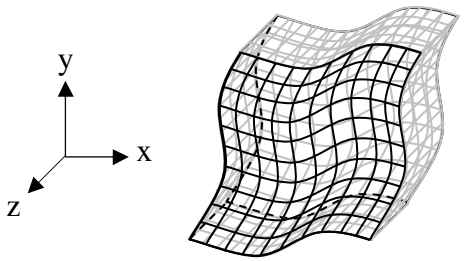

Figure 3.9 Unit cell whose grey-checked surfaces are constrained in the *z*-direction. The black-checked surface represents the symmetry plane

Measured τ_{xy}: 18.46 MPa

Alternative E

This alternative uses the defined symmetry plane as the only constraint in the *z*-direction, shown in figure 3.10.

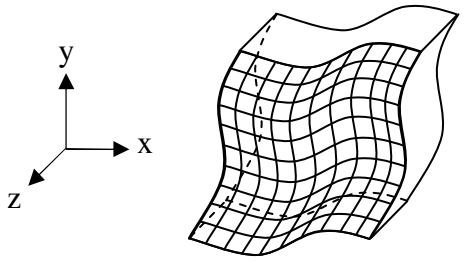

Figure 3.10 Unit cell where the black-checked surface represents the symmetry plane

Measured τ_{xy}: 18.41 MPa

As seen, the shear stress in the *xy*-direction shows no great influence from the constraints in the *z*-direction. As a consequent, alternative E is selected to be the final model of the unit cell exposed to shear deformation. It involves as favorable constraints as possible for a minimum calculation cost. The final models are now determined and are ready to be created as FE models.

3.1.2 FE micromechanical models

This section deals with the creation of the finite element models of the hydrostatic model and the shear model. Some subjects such as geometries and boundary conditions are different for the two models and are treated in individual sections. Subjects such as material data input, load steps, mesh and interactions are the same for both model types and are discussed in common sections.

3.1.2.1 Geometry

Since the constitutive laws contain ratios between strains and stresses, the units of the geometry have no importance as long as they are consistent. To make the modeling as simple as possible the unit cell is modeled in meters (m), which can be regarded as an arbitrary length unit since there is no length-scale dependence in the present model.

The unit cell is given the shape of a cube with the dimensions $100\times100\times100$ (m) and a spherical void is situated in the center of the cube. The void has the exact same radius as the spherical particle. The radius is varied depending on the simulated particle volume concentration, which was discussed in section 2.3. The radius for different particle volume concentrations are listed below in table 3.1.

Table 3.1 Radius of sphere and void at different particle volume concentrations

PVC (%)	Radius, *r* (m)
10	28.794
15	32.961
20	36.278
25	39.080
30	41.528

3.1.2.1.1 Geometry of the hydrostatic model

As explained in section 3.1.1, the hydrostatic model takes the shape of one eighth of the whole unit cell and gets consequently the appearance that is shown in figure 3.11 below.

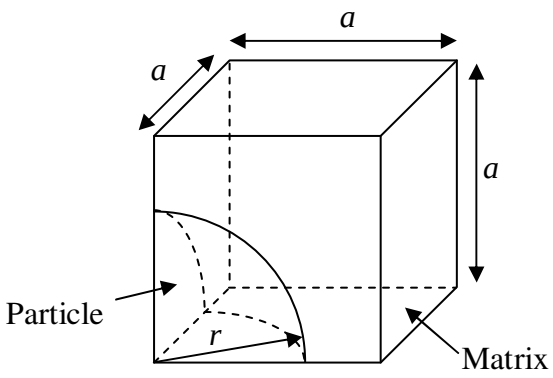

Figure 3.11 Geometry of the hydrostatic model

One eighth of the unit cell consequently gives the dimension a the value a = 50 (m) and the radius r takes the value presented in table 3.1 depending of the particle volume concentration in the simulation.

3.1.2.1.2 Geometry of the shear model

As mentioned, the shear model involves one half of the unit cell and its dimensions are shown in figure 3.12.

Dimension a and radius r are the same as for the hydrostatic model while dimension b = 100 (m).

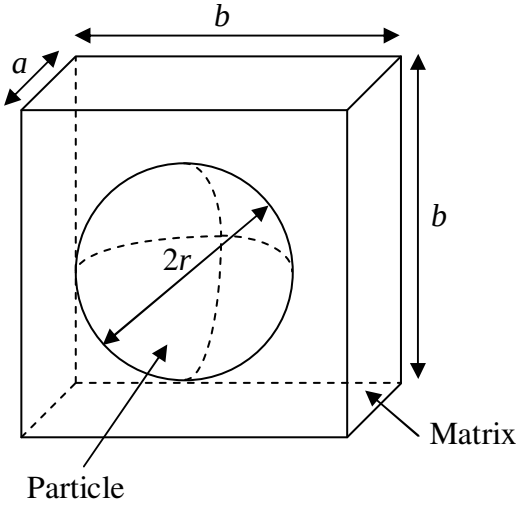

Figure 3.12 Geometry of the shear model

3.1.2.2 Mesh and elements

A rather fine mesh, consisting of 8-node, reduced integration, linear hexahedral (brick-shaped) elements (C3D8R), is used. Brick-shaped elements give the best results for the minimum costs. The mesh is a bit denser around the boundary of the particle where the stress gradients are higher and the appearance of the mesh is different for models with different PVC to avoid distorted elements that might cause solver problems. Inspection of the stress plots (Appendix A) shows no oddities around the particle boundary. Fully integrated elements that handle large stress gradients better could be used locally in the region around the particle but this was found not to be necessary.

The meshes of the hydrostatic and shear models are shown in figure 3.13 and 3.14 respectively. In both figures the particle is separated from the matrix just to get a better view of the mesh.

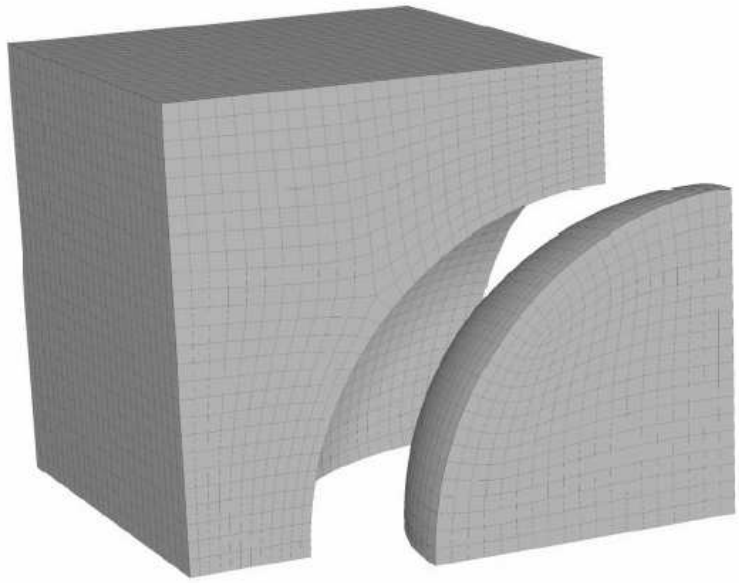

Figure 3.13 Mesh of the hydrostatic model

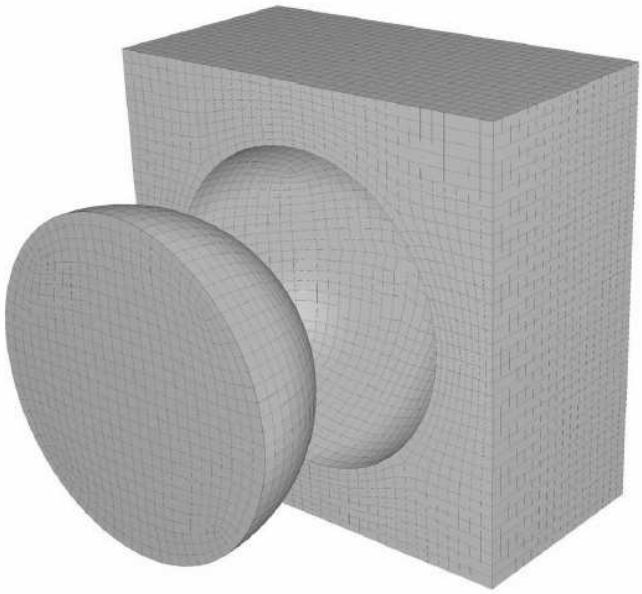

Figure 3.14 Mesh of the shear model

3.1.2.3 Interactions

The binder is assumed to perfectly surround the filler particle and no contact occurs between them, which means that the nodes of the sphere are tied to the corresponding nodes of the matrix. This assumption may not be true in reality, but simplifies the modeling a lot. The approximation is mainly due to the large problem of obtaining the friction coefficient between the binder and particle, a task that would not be possible to perform in this limited work. To enforce this, the commando TIE that ties parts to one another has been used. This commando ties the nodes of the particle to the corresponding nodes of the matrix. Some models are instead made as one part and the particle and matrix are defined as two different regions. This way, the use of the TIE commando is not necessary.

3.1.2.4 Boundary conditions

The general criterions for the boundary conditions for the models have already been established in section 3.1.1 and are discussed in detail in this section.

3.1.2.4.1 Boundary conditions of the hydrostatic model

Since only one eighth of the whole unit cell is modeled, symmetry conditions

must be defined. Shown as checked surfaces in figure 3.15, symmetry planes are defined in the *x*-, *y*- and *z*-directions respectively at the cutting planes.

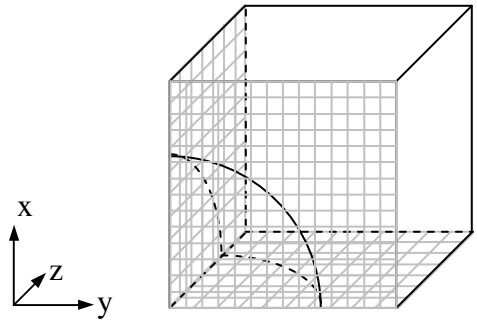

Figure 3.15 Symmetry planes in the *x*-, *y*- and *z*-directions on the hydrostatic model

The hydrostatic deformation is also applied as boundary conditions, namely as displacements of the outer surfaces in the negative normal directions of the surfaces. The concerned surfaces are shown as checked surfaces in figure 3.16.

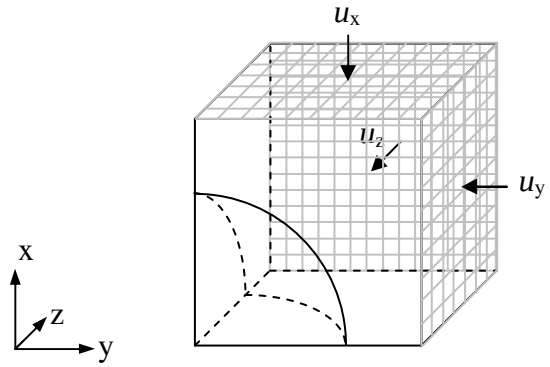

Figure 3.16 Displacements of the checked surfaces in their respective negative directions

All displacements have the same magnitude and are chosen to be $u_x = u_y = u_z = -0.5$ (m) resulting in the strains $\varepsilon_x = \varepsilon_y = \varepsilon_z = -0.01$ of the surfaces since $\varepsilon = \Delta l / l$.

To let the reader get a better understanding on how these boundary conditions function, a picture of the model after deformation is shown in figure 3.17.

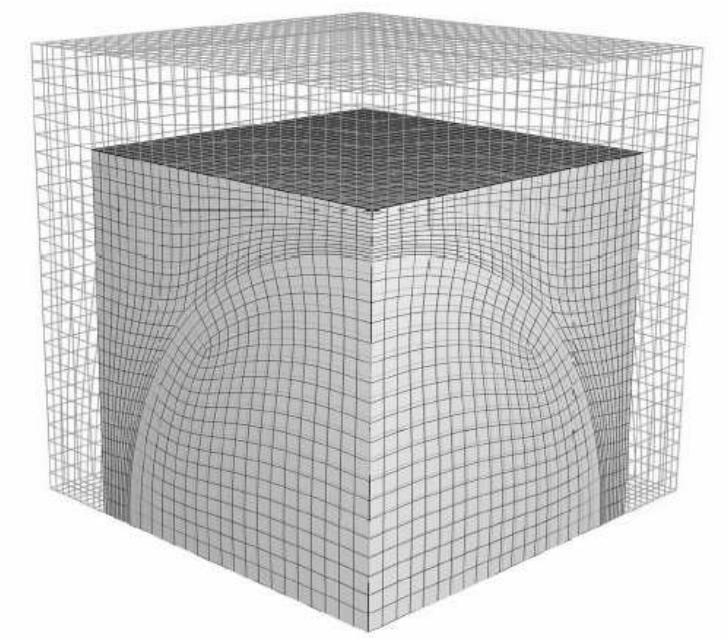

Figure 3.17 Initial and deformed shape of the hydrostatic model

3.1.2.4.2 Boundary conditions of the shear model

A symmetry plane is defined in the *z*-direction where the unit cell has been cut in half. The symmetry plane is shown in figure 3.18 as the checked surface.

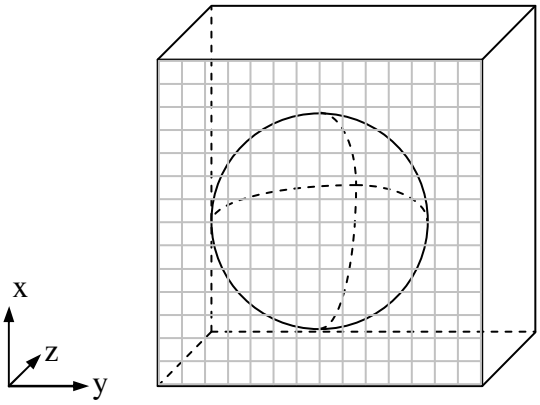

Figure 3.18 Symmetry plane in the *z*-direction on the shear model

The shear deformation is applied as boundary conditions on the surfaces that are checked in figure 3.19. The boundary conditions are defined as equally large displacements in the directions shown by the arrows in the figure.

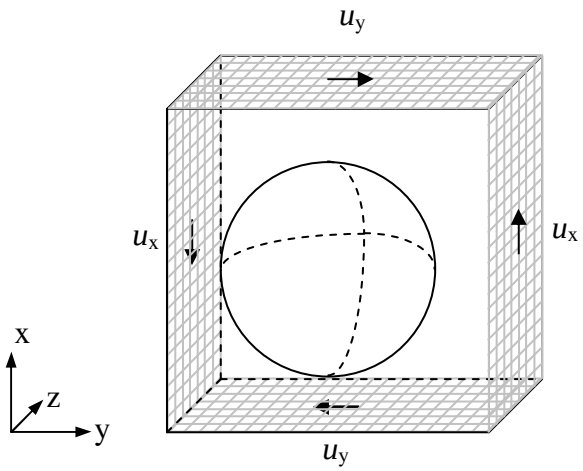

Figure 3.19 Displacements of the checked surfaces

Each displacement has the magnitude 0.5 (m) and by using equation 2.32 this gives the total shear strain ε_{xy} of the model:

$$\varepsilon_{xy} = \frac{1}{2}\left[\frac{0.5+0.5}{100} + \frac{0.5+0.5}{100}\right] = 0.01$$

A picture showing the resulting deformation of the shear model is shown in figure 3.20.

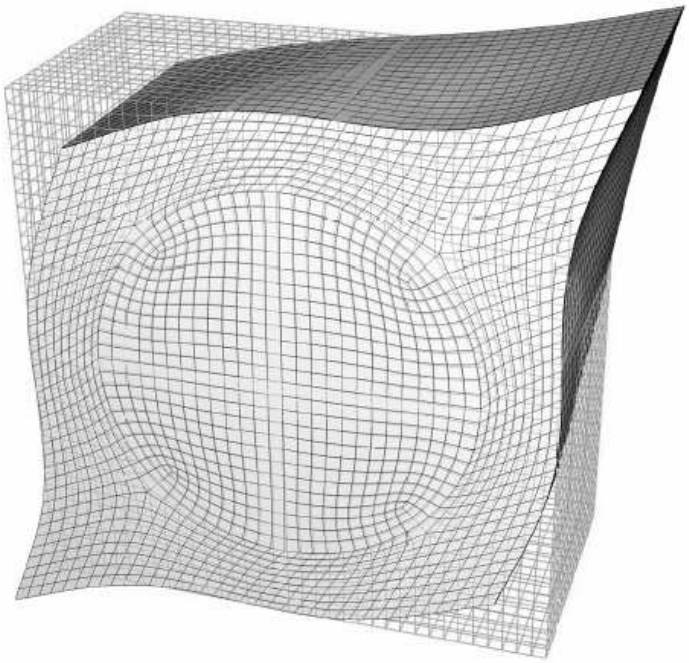

Figure 3.20 Initial and deformed shape of the shear model

3.1.2.5 Material data input

The material data input is the same for both models but is in this section divided into subsections; one for the filler material, barite, and one for the binder material, polyester.

3.1.2.5.1 Filler (barite)

The single crystal elastic constants for barite from table 2.1 are inserted into equations 2.13 and 2.14 and are also transformed into their corresponding elastic compliance constants by equation 2.17. The elastic compliance constants are on their part inserted into equations 2.15 and 2.16. This gives the following values of the Voigt and Reuss shear moduli and bulk moduli, respectively:

$$G_V = 0.2525 \cdot 10^{11} \text{ Pa}, \qquad K_V = 0.5255 \cdot 10^{11} \text{ Pa}$$
$$G_R = 0.2138 \cdot 10^{11} \text{ Pa}, \qquad K_R = 0.5236 \cdot 10^{11} \text{ Pa}$$

The average values of the shear and bulk moduli are consequently:

$$G = 0.2331 \cdot 10^{11} \text{ Pa}$$
$$K = 0.5245 \cdot 10^{11} \text{ Pa}$$

Young's modulus, E, and Poisson's ratio, ν, for barite are finally obtained by insertion of the previous values into equations 2.18 and 2.19, respectively, which give:

$$E = 0.6092 \cdot 10^{11} \text{ Pa}$$
$$\nu = 0.3064$$

3.1.2.5.2 Binder (polyester)

To obtain the required material data for the binder material, relaxation tests are performed of specimens of the material. If layers of a thickness greater than 150 µm are created voids will appear in the material during the curing process. Consequently, the test specimens can only be made with very small thicknesses. Because of the small thickness, the easiest way to obtain relaxation data of the material is to perform uniaxial tension tests.

Figure 3.21 shows a photo of a film of binder material. The test specimens that are used for the relaxation measurements have the following

Thickness: 100 µm
Width: 4-5 mm
Length: 40 mm (clamping length: 10-15 mm)

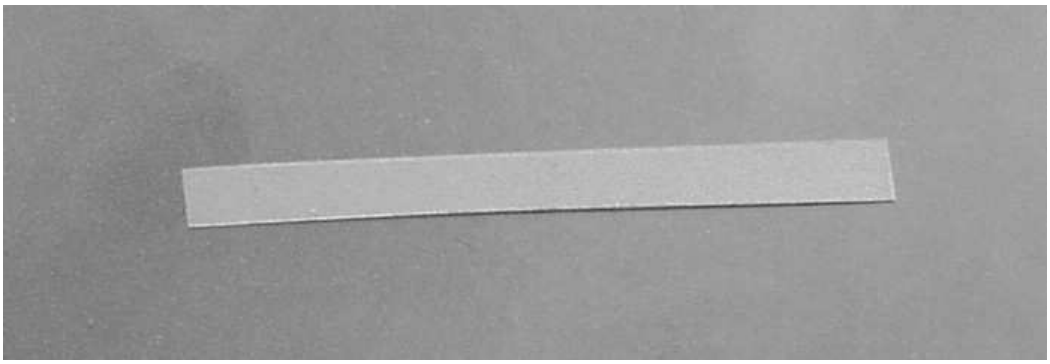

Figure 3.21 Film of binder material

The relaxation measurements are performed by using the Dynamic Mechanical Analysis (DMA) equipment shown in figure 3.22 and 3.23. The test specimen is exposed to a constant strain of 0.2-0.3% and the equipment measures the stress reduction against time. The magnitude of the strain is low enough to avoid plastic deformation of the test specimen. The strain magnitude must also be kept as low as possible to not interfere with the assumption of linear viscoelasticity, which normally occurs at small strains. An oven can be used to make relaxation tests at elevated temperatures.

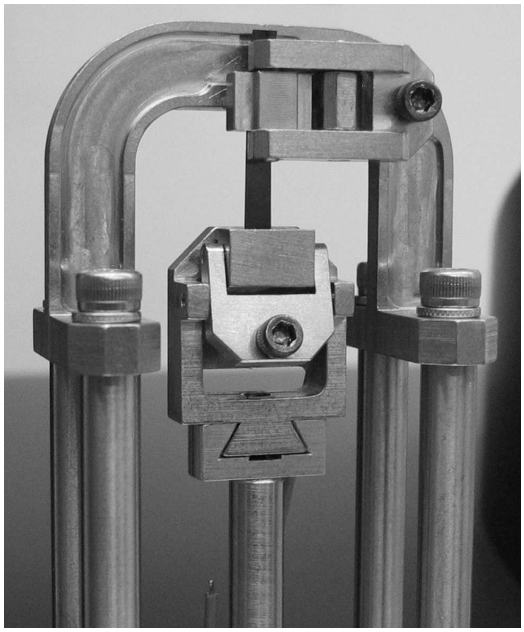

Figure 3.23 Test specimen clamped and ready to be analyzed

The procedure on how to determine the viscoelastic input parameters of the binder material will now be presented. The relaxation measurements are performed at different temperatures, but in an attempt to make this report easier to follow only the procedure for 25°C is explained. Relaxation curves for the other temperatures and tables of their corresponding input parameters are included in Appendix B and Appendix C.

The first step is to analyze the relaxation curve of the elastic modulus of the binder, which is shown in figure 3.24, and shows how the material has relaxed for approximately 12 hours. It can be seen that most of the relaxation occurs in the beginning and that the asymptote at the end is not perfectly stable but oscillates slightly in the region around E = 2000 MPa. An assumed value of the asymptote is calculated as the average value of the last points of measuring, resulting in a value of E_∞ = 1993.6 MPa. The beginning of the curve is examined to decide the initial value and figure 3.25 shows the appearance of the beginning of the curve.

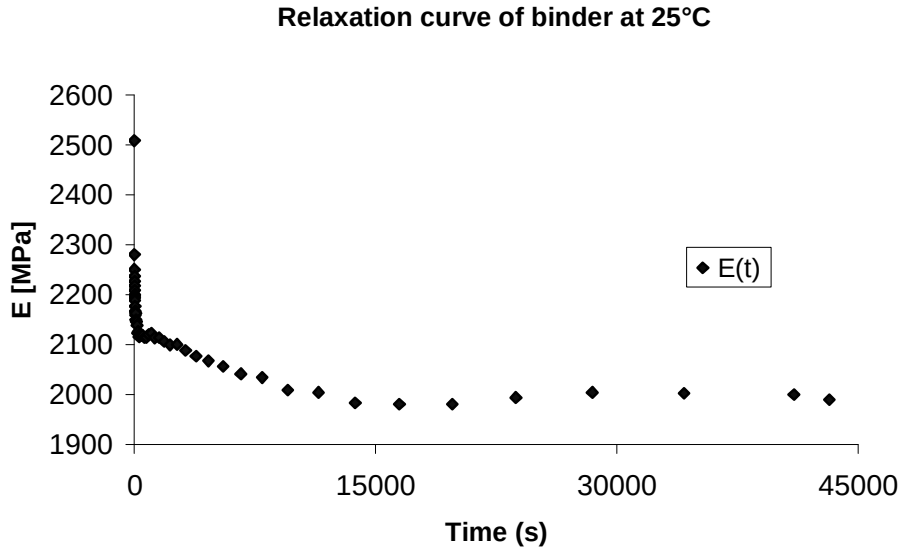

Figure 3.24 Relaxation curve of the binder

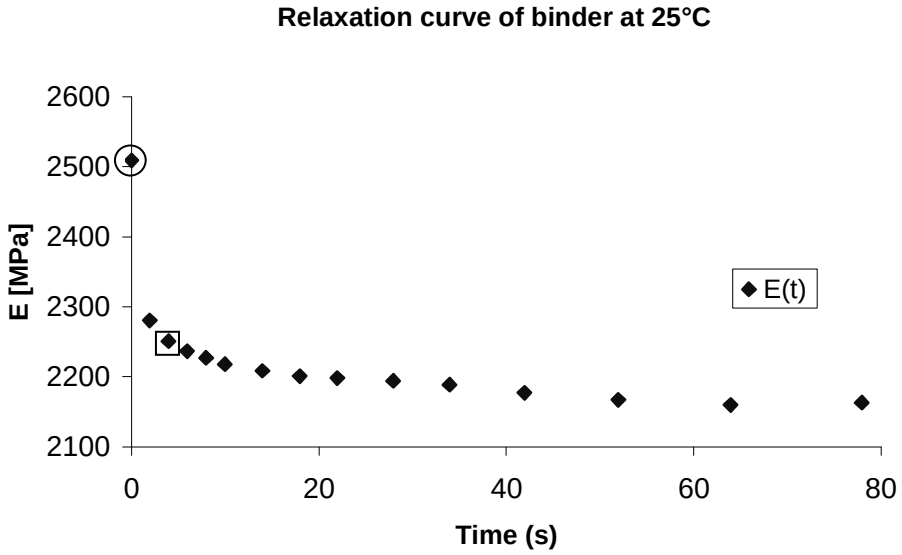

Figure 3.25 Beginning of relaxation curve of the binder. The circle marks the initial value while the square marks the value that actually will be used in the simulations

Since the clamping force loss is a comparison between the initial and final clamping force, the initial value of the elastic modulus plays an important role. As seen by the encircled dot in figure 3.25, the initial value is much larger than the second value, and will therefore not be used in the simulations. Instead the dot that is marked with a square, E = 2250.8 at 4 seconds, will act as the initial value.

By deleting the first and second points in the original curve and adding the calculated asymptotic relaxed value to the end of the original curve, the resulting curve now takes the form shown in figure 3.26. This curve is used in the simulations.

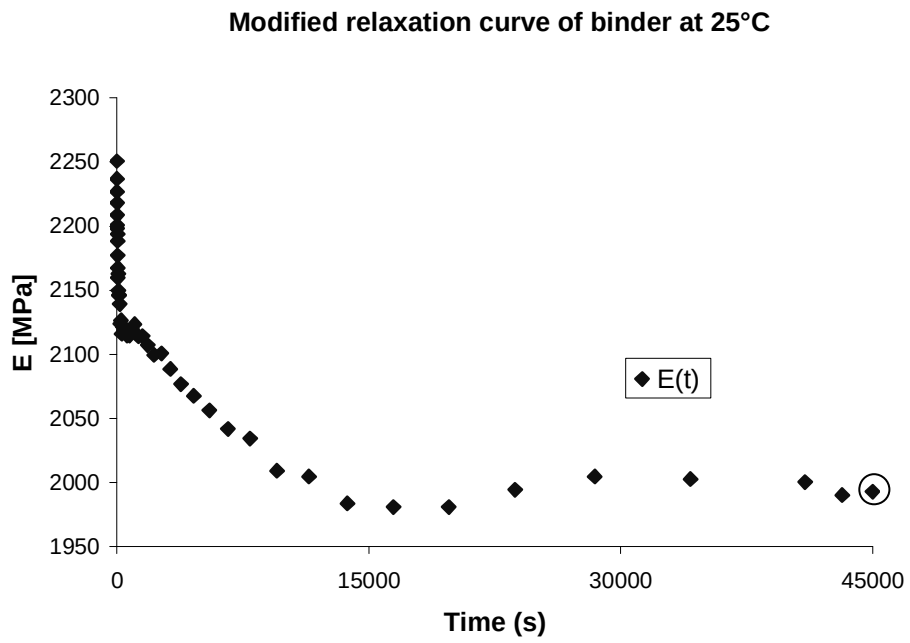

Figure 3.26 Modified relaxation curve for the simulations at 25°C. The encircled dot represents the calculated relaxed value

Next step is to transform this relaxation curve for the elastic modulus to a relaxation curve for the shear modulus, which is required by ABAQUS. The initial value of Poisson's ratio at 25°C for the binder is already determined to $v_0 = 0.38$, and together with equation 2.22 the constant value for the bulk modulus of the binder material can be determined to:

$$K_0 = \frac{2250.8}{3(1-2\cdot 0.38)} = 3126.1 \text{ MPa}$$

Since K is constant Poisson's ratio can be determined for every point of measuring with equation 2.23. When this is done the relaxation shear modulus $G(t)$ can be obtained with equation 2.24. Finally equation 2.27 is used to determine the value α_i for all points of measuring, which are the used values in ABAQUS together with the corresponding times, E_0 and v_0. Table 3.2 shows the resulting numbers for all these described steps from the initial relaxation values of the elastic modulus to the values of α_i and their corresponding times. The asymptotic value is also included, and the grey-

shaded areas in the table represent the data that are used as input parameters in ABAQUS.

Table 3.2 Transformed data from relaxation measurement to input data for ABAQUS. Grey-shaded areas represent the used input parameters

Time (s)	$E(t)$ (MPa)	$K(t)$ (MPa)	$v(t)$	$G(t)$ (MPa)	$\alpha_i(t)$
0	2251	3126	0.3800	815	0.999999
2	2237	3126	0.3807	810	0.993286
4	2227	3126	0.3813	806	0.988483
6	2218	3126	0.3817	803	0.984252
10	2209	3126	0.3822	799	0.979668
14	2201	3126	0.3827	796	0.975881
18	2198	3126	0.3828	795	0.974731
24	2194	3126	0.3830	793	0.972673
30	2188	3126	0.3833	791	0.969986
38	2177	3126	0.3839	787	0.964567
48	2167	3126	0.3844	783	0.959839
60	2160	3126	0.3848	780	0.956241
74	2163	3126	0.3847	781	0.957694
90	2150	3126	0.3854	776	0.951457
110	2146	3126	0.3856	774	0.949631
134	2146	3126	0.3856	774	0.949679
162	2139	3126	0.3859	772	0.946423
196	2124	3126	0.3868	766	0.938991
238	2126	3126	0.3866	767	0.940254
288	2116	3126	0.3872	763	0.935286
348	2122	3126	0.3869	765	0.937920
420	2119	3126	0.3870	764	0.936715
506	2119	3126	0.3870	764	0.936677
610	2115	3126	0.3873	762	0.934665
734	2115	3126	0.3872	762	0.934708
882	2120	3126	0.3870	764	0.937351
1060	2123	3126	0.3868	766	0.938838
1274	2114	3126	0.3873	762	0.934383
1530	2114	3126	0.3873	762	0.934450
1838	2107	3126	0.3877	759	0.931024
2208	2100	3126	0.3881	756	0.927438
2652	2101	3126	0.3880	757	0.928030
3184	2089	3126	0.3886	752	0.922152
3822	2077	3126	0.3893	747	0.916598
4588	2068	3126	0.3898	744	0.912187
5508	2057	3126	0.3904	740	0.906889

6612	2042	3126	0.3911	734	0.899890
7936	2034	3126	0.3915	731	0.896299
9526	2009	3126	0.3929	721	0.884393
11434	2005	3126	0.3931	720	0.882322
13722	1984	3126	0.3942	711	0.872365
16468	1981	3126	0.3944	710	0.871026
19764	1981	3126	0.3944	710	0.871045
23718	1994	3126	0.3937	716	0.877443
28464	2005	3126	0.3931	719	0.882251
34158	2003	3126	0.3932	719	0.881360
40992	2000	3126	0.3934	718	0.880214
43194	1990	3126	0.3939	714	0.875426
∞	1994	3126	0.3937	715	0.877049

By using the initial values for the elastic modulus and Poisson's ratio, the time points and corresponding values of α_i, and the asymptotic value, the viscoelastic properties of the binder material are fully described. The same transformation as in table 3.2 but with 0.40 as the initial value of Poisson's ratio for the polyester binder can be found in table D.1 in Appendix D. The previous example shows how the data for relaxation at 25°C is used but the procedure is the same for all temperatures. Caution is needed when initial and asymptotic values are selected.

All input parameters for the binder at different temperatures can be found in the appendices mentioned in the text. To let the reader get a clearer view of the quantities, the initial and long-term values of the elastic modulus and Poisson's ratio are listed in tables 3.3 and 3.4.

Table 3.3 Initial and relaxed values of the elastic modulus for the binder material at different temperatures

Temperature	25°C	60°C	100°C
E_0 (MPa)	2251	1451	2.33
E_∞ (MPa)	1994	17.0	1.29

Table 3.4 Initial and relaxed values of Poisson's ratio for the binder material at different temperatures

Temperature	25°C		60°C		100°C			
v_0	0.380	0.400	0.380	0.400	0.380	0.400	0.480	0.490

3.1.2.5.3 Extreme binder materials (polypropylene, epoxy)

The initial and relaxed material properties for the extreme binders are calculated in the same manner as in the previous section and are shown in table 3.5.

Table 3.5 Initial and relaxed material properties for the extreme binders at 25°C

Binder material	Polypropylene	Epoxy
E_0 (MPa)	715	2800
E_∞ (MPa)	535	2670
ν_0	0.320	0.380
ν_∞	0.365	0.386

3.1.2.6 Steps

The simulations are performed in two steps; one initial static step and a second viscous step. The first initial step is very short (0.01 seconds) and illustrates the initial strain that causes the initial stress in the relaxation test. The second step continues where the first step ended and describes the time-dependent viscous step. The time period starts at 0.01 seconds and ends a bit later than the last point of time in the measured relaxation curve for the binder. This way it is certain that the binder material in the model has reached its relaxed value. The length of the time period depends consequently on how fast the binder materials relax and is subsequently adapted to that. The increment length is adjusted automatically, which is the most reliable way to pace the time period. The length of each increment is allowed to vary between 0.01 seconds as the lower limit. and the final time of the period as the upper limit. This way the increments are small in the beginning when the relaxation rate is high and get larger by the end when the relaxation rate has decreased.

3.1.2.7 Outputs

For the hydrostatic model the sum of the reaction forces normal to the outer surfaces, where the displacements are applied, are obtained. That is the sum of all reaction forces in the *x*-direction on the surface with its normal in the *x*-direction, the sum of all reaction forces in the *y*-direction on the surface with its normal in the *y*-direction and the same for the surface in the *z*-direction.

increment. Since hydrostatic deformation gives rise to a symmetric stress state it would be sufficient to only obtain the forces on one surface but by collecting the result from all three surfaces it is possible to confirm the symmetric results.

The output for the shear model is the sum of all reaction forces in the *x*-direction on a surface whose normal is in the *y*-direction (figure 2.15 shows such a surface), which, divided by the surface area, is the definition of shear stress. The output is delivered for every time increment.

3.1.3 Treatment of the obtained results

A MATLAB program is made to treat the results that are written to the text file by ABAQUS. The program code depends on what simulation has been performed but one example can be found in Appendix E. The code will not be discussed in detail but is of importance as it is the last step to obtain the desired viscoelastic properties. To begin with, the way to obtain the bulk modulus $K(t)$ is explained.

The sums of the reaction forces acting on each surface (explained in section *3.1.2.7 Outputs*) are stored and divided by the surface area, which is the same for all three surfaces, namely 50 x 50 = 2500 (m^2). The three stresses σ_x, σ_y and σ_z acting on the unit cell are calculated and the bulk modulus can now be calculated for the first time increment. The strains acting on the unit cell in the three directions were calculated in section *3.1.2.4.1 Boundary conditions of the hydrostatic model* and equation 2.29 consequently becomes:

$$K(t) = \frac{\sigma_x(t) + \sigma_y(t) + \sigma_z(t)}{3((-0.01) + (-0.01) + (-0.01))} \qquad (3.1)$$

By inserting the obtained values for σ_x, σ_y and σ_z (which all have negative values because of the hydrostatic compression), the bulk modulus K is calculated. This is done for all time increments and the results are stored.

The way to calculate the shear modulus is almost the same. The sum of the reaction forces is stored and divided by the surface area 100 x 50 = 5000 (m^2), which consequently results in the shear stress τ_{xy}.

The shear strain that was calculated in section *3.1.2.4.2 Boundary conditions of the shear model* is inserted in equation 2.31, leading to the following form of the equation:

$$G(t) = \frac{\tau_{xy}(t)}{2 \cdot 0.01} \tag{3.2}$$

The shear modulus $G(t)$ is now calculated for all time increments by insertion of respective shear stress τ_{xy} in the expression.

Young's modulus and Poisson's ratio are finally calculated by equations 2.18 and 2.19. By this moment are the simulated viscoelastic properties of the powder coating obtained. The results are presented in section *4 Results.*

3.2 CLAMPING FORCE LOSS SIMULATIONS

The previous simulations have now obtained viscoelastic properties of powder coatings with different particle volume concentrations. Next step is to simulate the clamping force loss in a screw joint reinforcement by assigning the coating in a model the obtained results. The simulated clamping force loss results will be compared to experimentally obtained results. The test equipment used for the experiments represents a number of simplified screw joint reinforcements that can be seen in figure 3.27.

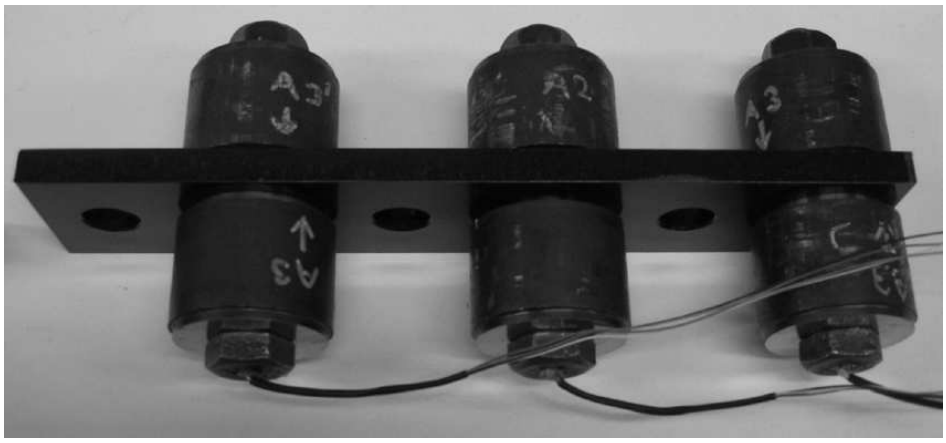

Figure 3.27 Equipment used to measure the clamping force loss

One joint consists of a steel plate with powder coatings on each side, two washers, one screw and one nut. A strain gauge is applied to the screw to measure the strain in the screw, which can be translated into the clamping force that acts on the screw. The screw joint reinforcement is tightened at room temperature until a certain clamping force is achieved. The equipment is then left for a long time either at room temperature or at an increased temperature in an oven. The equipment rests like that until the powder coating is fully relaxed and the final clamping force is finally measured. The final clamping force is then compared with the initial one and is described as the percentage of the initial clamping force.

Five main simulation cases are made and table 3.6 shows the configuration of initial and final temperatures, PVC and coating thickness for each one of them. These main cases will later be divided into sub-cases depending on material types and different values of Poisson's ratio for the binder material. Two coating thicknesses are used depending on the particle volume concentration. Consequently the FE models will vary slightly for some of the simulation cases.

Table 3.6 Cases for the clamping force simulations

Simulation case	Initial temperature (°C)	Final temperature (°C)	PVC (%)	Coating thickness (µm)
A	25	25	15	115
B	25	25	25	110
C	25	100	15	115
D	25	100	25	110
E	25	60	25	110

3.2.1 Creation of the FE model

Figure 3.28 shows a representation of one of the screw joint reinforcements that are shown in figure 3.27. The joint has been cut in half to make a clearer view of the involving parts.

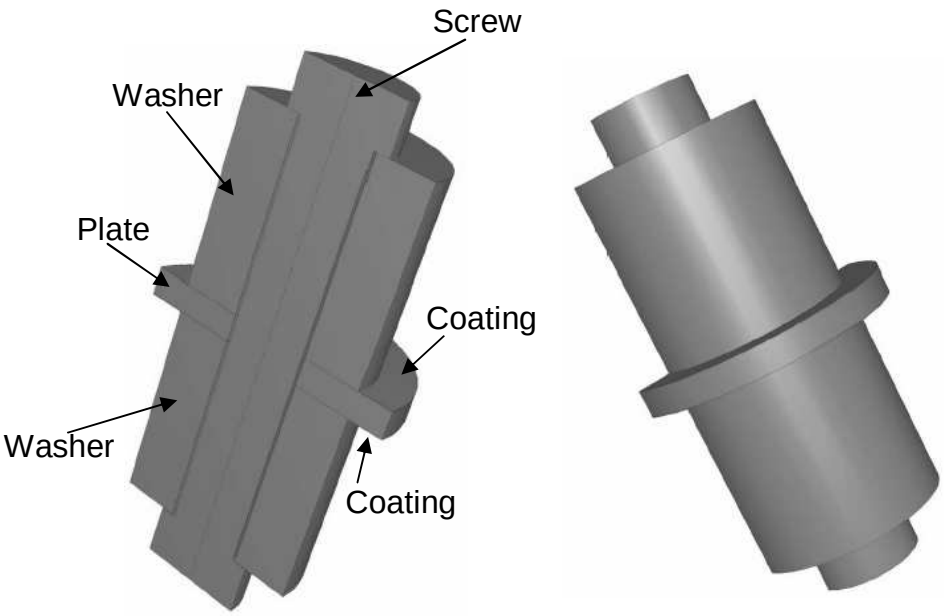

Figure 3.28 Representation of the screw joint reinforcement

The cylindrical washers have an outer diameter of 37 mm and a thickness of 35 mm. The thickness of the steel plate is 5 mm and has been assigned an outer diameter of 50 mm. The coating has the same outer diameter as the steel plate and all parts have a hole along the symmetry axis with a diameter of 15.2 mm. The M14 screw that traverse the axial hole is attached to a nut on the other side and both are in contact with respective washer. The resulting contact surface is limited on the inside by the diameter of the hole

3.2.1.1 Geometry

To decrease calculation costs, the axisymmetric properties of the joint are used to create a 2D axisymmetric model. The symmetric properties across the symmetry axis also help to simplify the model further. Consequently the FE model will have the appearance and dimensions shown in figure 3.29. The thickness of the coating will vary depending on simulation case.

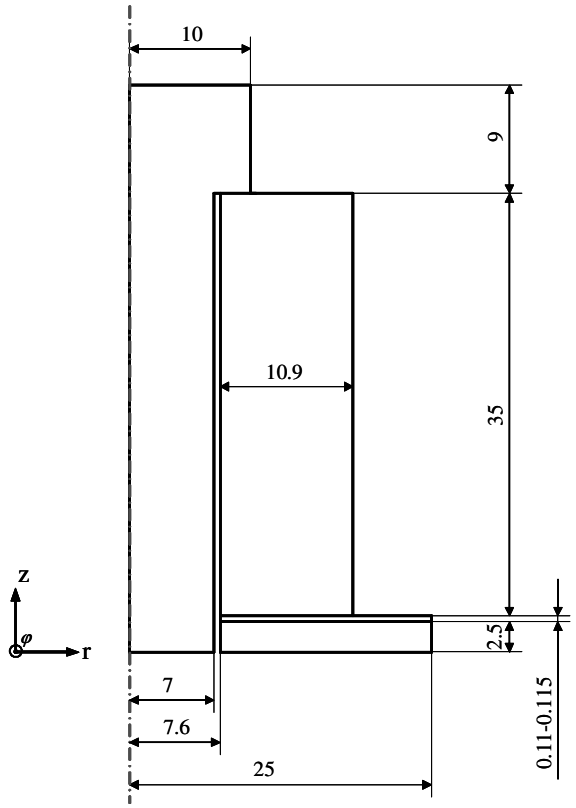

Figure 3.29 Geometry and dimensions of the FE model. The symmetry axis is shown to the left as a dotted line. All dimensions are in millimeters

3.2.1.2 Mesh and elements

The same mesh is used for all simulation cases and its appearance is shown in figure 3.30. The mesh is denser in the regions around the coating, the boundary between the screw head and the washer, and where the displacement is applied to the screw. The same figure also shows an enlarged view of the region around the coating where the difference in size between the elements can be seen. ABAQUS warns if the aspect ratio of an element is greater than 100 but that is not the case for the elements used in the coating.

In cases A and B, 8-node biquadratic axisymmetric quadrilateral (CAX8)

same as in the previous cases but are also coupled between temperature and displacements. Inspection of the stress plots (Appendix F) shows no oddities in the model.

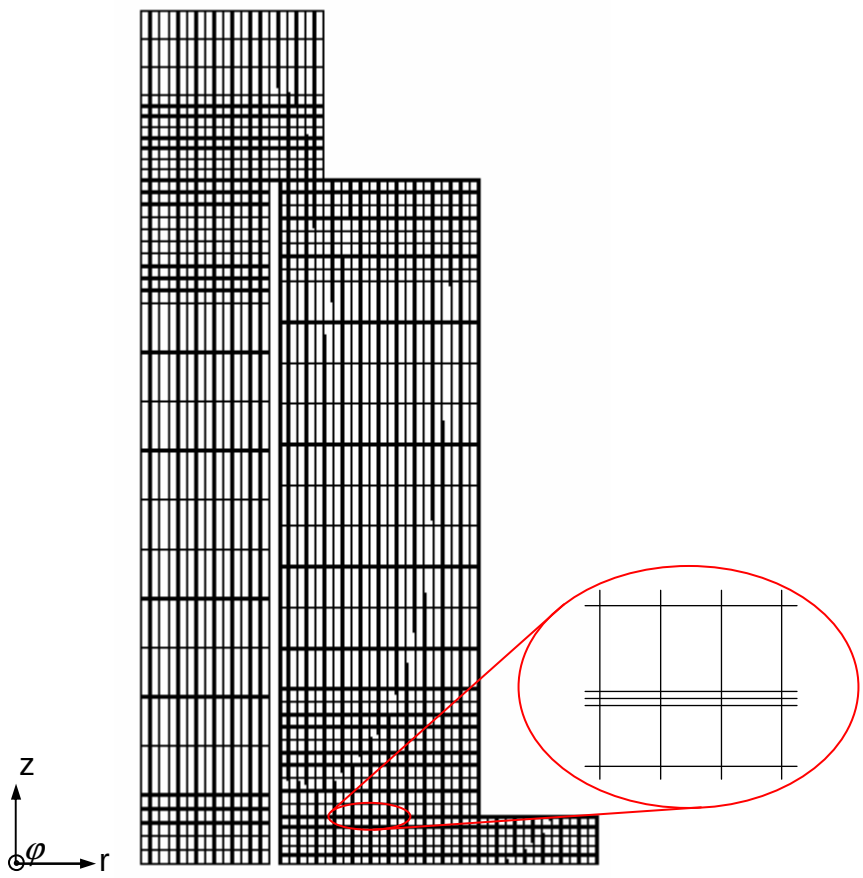

Figure 3.30 Mesh of the FE model and a magnified picture of the mesh in the region around the coating

3.2.1.3 *Interactions*

No interactions are defined in the model. The coating is assumed to be perfectly attached to the steel plate. In reality contact occurs between the top of the coating and the washer, and between the nut and washer. Since only axial load is applied to the screw no slipping is assumed to occur between the involved parts. Therefore it is possible to define the model as one single part and the nodes on the boundaries between the real parts, i.e. plate, coating, washer and screw head, are tied to one another. The FE part is, however, divided into regions to make meshing easier and to assign the steel parts and the coating their material properties.

3.2.1.4 Boundary conditions

The boundary conditions that are used in the model are shown in figure 3.31. A symmetry line is defined in the *z*-direction on the steel plate and displacements acting on the screw in the negative *z*-direction are applied too. These displacements generate the clamping force that can be measured as the sum of the reaction forces in the *z*-direction either on the screw or on the steel plate. The resulting deformation of the applied boundary conditions is shown in figure 3.32.

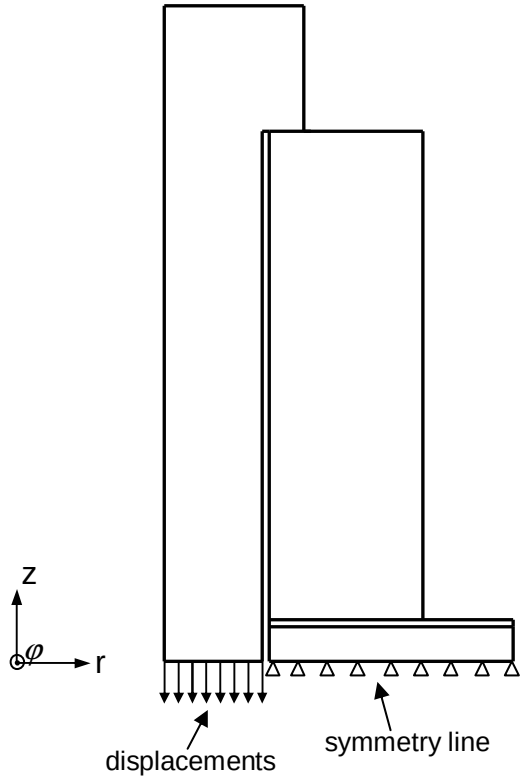

Figure 3.31 Boundary conditions defined on the model

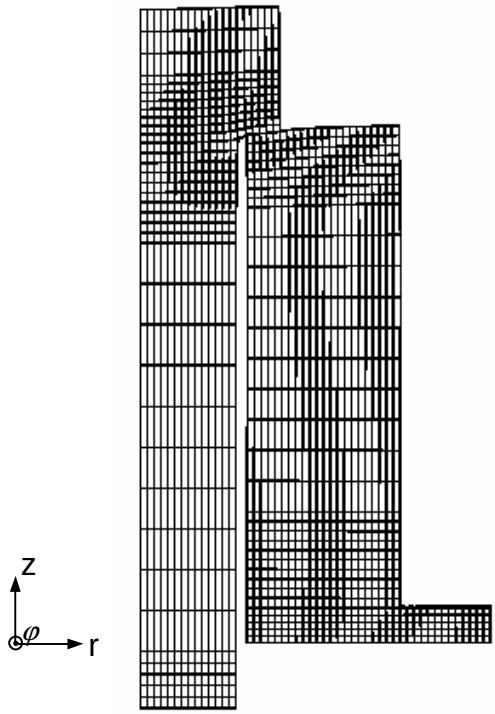

Figure 3.32 Resulting deformation

In simulation cases C, D and E, an additional boundary condition must be applied, namely an increased temperature for the entire model. The exact temperatures are of minor interest, instead the purpose is to examine how mush a certain increase of temperature influences the clamping force. In case C and D the temperature is increased from 25°C to 100°C and for case E from 25°C to 60°C, i.e. a temperature increase of 75°C and 35°C, respectively. The initial model is therefore defined as a reference and the temperature boundary conditions are 75°C for simulation cases C and D and 35°C for simulation case E.

3.2.1.5 Material data input

The steel parts and the screw are assumed to be made of the same material and are assigned an elastic modulus E = 209 GPa and a Poisson's ratio v = 0.29. The thermal expansion coefficient is set to $\alpha = 12.5 \cdot 10^{-6} C^{-1}$. The coefficient of thermal expansion and Poisson's ratio for the steel parts and the screw were calculated with J-Mat Pro at Materials Technology, Scania.

This is where the link to the micromechanical simulations is established by assigning the powder coating used in this model the results from the micromechanical simulations. The configuration of the material data inputs that is used in the simulations is showed in table 3.7. The table shows what

initial and final material properties will be used depending on temperature and particle volume concentration. Each simulation case will later be divided into sub-cases to make simulations of varying Poisson's ratios possible. These sub-cases are presented and explained in section *4 Results and discussion*.

The coefficient of thermal expansion for the powder coating, α_c, is calculated with equations 2.33 and 2.34 for PVC = 15% and PVC = 25%. The results can be found in table 3.7.

Table 3.7 Initial and final material properties for the powder coatings depending on temperature and PVC for the simulation cases

Simulation case	Initial properties	Final properties	CTE ($10^{-6} C^{-1}$)
A	$[E, \nu]_{t=0,\ 25°C,\ PVC=15\%}$	$[E, \nu]_{t=\infty,\ 25°C,\ PVC=15\%}$	-
B	$[E, \nu]_{t=0,\ 25°C,\ PVC=25\%}$	$[E, \nu]_{t=\infty,\ 25°C,\ PVC=25\%}$	-
C	$[E, \nu]_{t=0,\ 25°C,\ PVC=15\%}$	$[E, \nu]_{t=\infty,\ 100°C,\ PVC=15\%}$	85.0
D	$[E, \nu]_{t=0,\ 25°C,\ PVC=25\%}$	$[E, \nu]_{t=\infty,\ 100°C,\ PVC=25\%}$	81.9
E	$[E, \nu]_{t=0,\ 25°C,\ PVC=25\%}$	$[E, \nu]_{t=\infty,\ 60°C,\ PVC=25\%}$	81.9

The results from the micromechanical simulations using the extreme binder materials will also be used. The clamping force loss simulations for these materials will only be performed at room temperature and for PVC = 25%, i.e. case B in tables 3.6 and 3.7. Table 3.8 shows these sub-cases to case B and the material input data for these simulations.

Table 3.8 Initial and final material properties for the powder coatings using the extreme binder materials

Simulation case	Initial properties	Final properties
B-polypropylene	$[E, \nu]_{t=0,\ 25°C,\ PVC=25\%}$	$[E, \nu]_{t=\infty,\ 25°C,\ PVC=25\%}$
B-epoxy	$[E, \nu]_{t=0,\ 25°C,\ PVC=25\%}$	$[E, \nu]_{t=\infty,\ 25°C,\ PVC=25\%}$

3.2.1.6 Steps

Simulation cases A and B contain only one step, namely a static step where the displacements are applied to the screw. Simulation cases C, D and E, contain two steps; the same static step as in the previous cases and an additional coupled temperature-displacement step where the temperature boundary conditions are applied.

3.2.1.7 Outputs

The requested outputs are the magnitudes of the displacements of the screw and the sum of the reaction forces in the *z*-direction acting on the screw.

3.2.1.8 Procedure

The following procedure is carried out to simulate the clamping force loss:

The initial values of the elastic material properties for the corresponding powder coating are entered and an arbitrary displacement is applied to the screw. ABAQUS delivers the resulting clamping force, which is supposed to be the same as the initial clamping force in the experimental tests. Due to linearity the applied displacement is easily adjusted to make it generate the correct clamping force. The displacement is now kept constant but the elastic material properties are changed to the final values. By keeping the displacement of the screw constant the clamping force changes when the elastic properties of the powder coating have changed and the final clamping force is now obtained. If the model involves heating, the final clamping force is obtained after the heating step is performed.

3.3 APPLICATION TO AN EXISTING MODEL

This section describes how this method can be applied in reality by modifying an already existing FE model. The FE model that will be used can be seen in figure 3.33 and represents a structure that is already being used at Scania, for real experiments and also for FE analyses. The model consists of a frame and a "paddle" that is fixed to the frame with a screw joint reinforcement that is encircled in the figure.

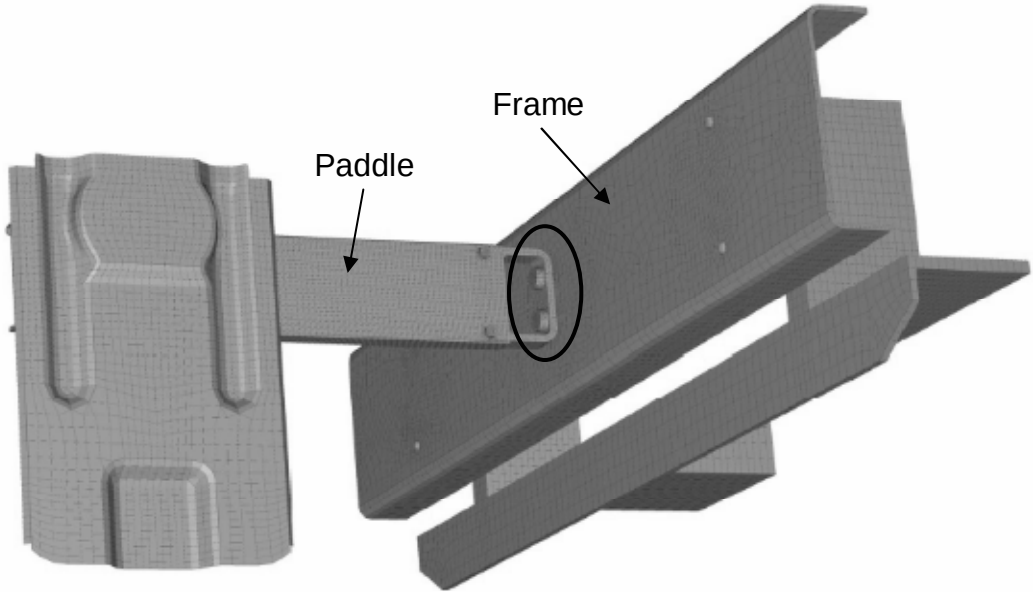

Figure 3.33 FE model of paddle fixed to frame with a screw joint reinforcement (encircled)

3.3.1 Creation of the FE model

The screw joint reinforcement is cut out off the existing model. Only the region closest to the contact area of the joint will be modeled since the interest is to examine the clamping force loss only. Therefore, the regions that are located far from the contact area, and consequently have no effect on the result, are deleted. Symmetry conditions of the joint make it possible to simplify the model even further, and only one quarter of the joint will be used. The involved parts of the final model are shown in figure 3.34 while the final model is shown in figure 3.35.

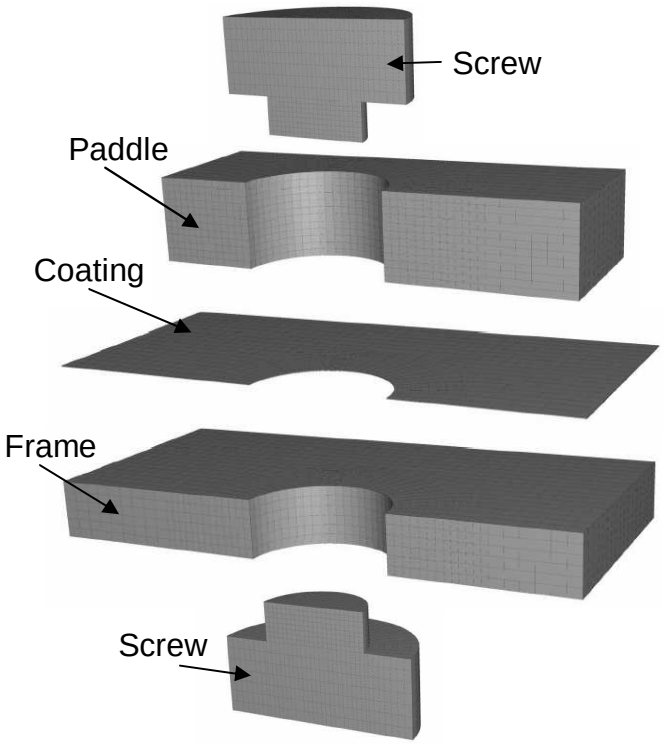

Figure 3.34 Involved parts of the model

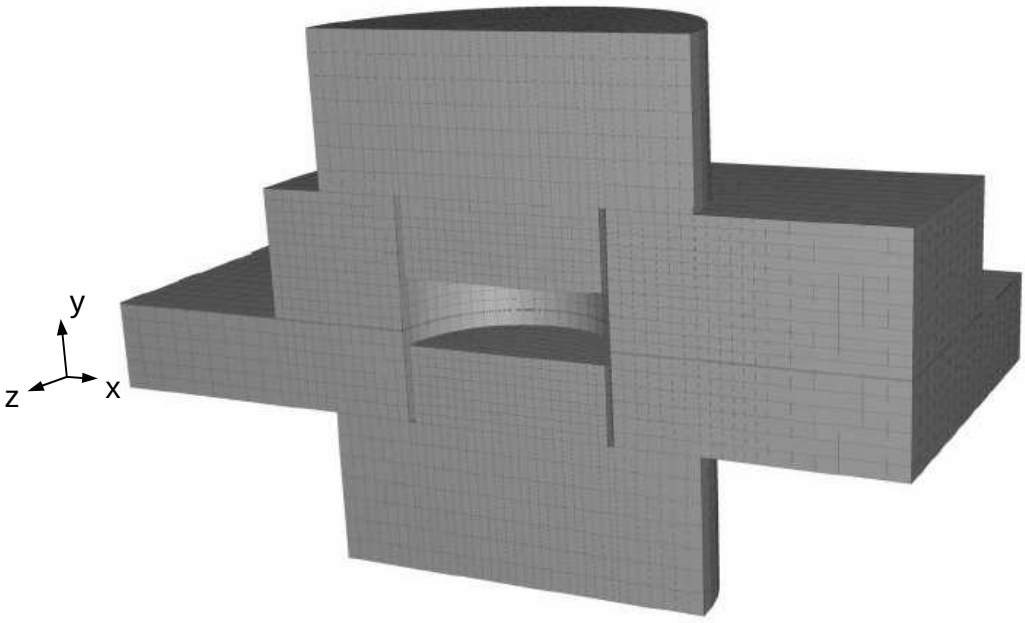

Figure 3.35 Model of the screw joint reinforcement

As seen in figure 3.34 the coating covers the frame completely and the contact surface area of the paddle is smaller than the area of the coating. Finally the screw is placed coaxially with the hole.

3.3.1.1 Geometry

The dimensions (*l* x *w* x *t*) in millimeters of the involved parts are presented below:

Paddle: 55 x 17.5 x 10
Coating: 65 x 30 x 0.11
Frame: 65 x 30 x 7

The diameter of the hole is the same for all parts: 17 mm. An M16 screw is used and a circle with a diameter of 30 mm describes the contact area of the screw head.

3.3.1.2 Mesh and elements

The overall mesh has already been showed in figure 3.35 and a close-up view of the mesh for the region around the coating is presented below in figure 3.36. The mesh consists of 8-node, reduced integration, linear hexahedral (brick-shaped) elements (C3D8R). Inspection of the stress plots (Appendix G) shows no oddities in the model.

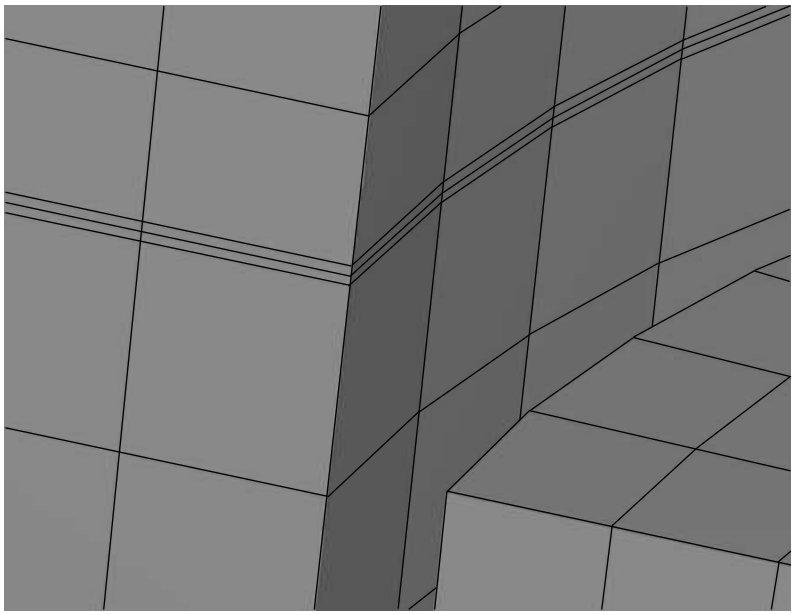

Figure 3.36 Close-up view of the mesh of the region around the coating

3.3.1.3 Interactions

Like in the previous model no interactions are defined in this model. The coating is assumed to be perfectly attached to the frame. In reality contact occurs between the coating and paddle, and between the screw and the frame and paddle, respectively. Since only axial load is applied to the screw no slipping contact is assumed to occur between the involved parts. The model is therefore defined as one single part so that the nodes on the boundaries between the parts are tied to one another. The part is, however, divided into regions to make meshing easier and to assign the steel parts and the coating their own material properties.

3.3.1.4 Boundary conditions

Symmetry conditions in the *z*-direction are defined for the cut surface of the joint in the *xy*-plane while symmetry conditions in the *x*-direction are defined for the cut in the *yz*-plane. The two outer surfaces of the frame are constrained in all directions and displacements in the *y*-direction are applied to the two screw parts, in the same manner as for the previous model in section *3.2 Clamping force loss simulation*. In this model the displacements act in the negative *y*-direction for the upper screw part and in the positive direction for the lower part. This model will be used at room temperature only and consequently no temperature boundary conditions are necessary. A picture showing the deformation of the model can be seen in figure 3.37. It is clearly visible how the screw joint reinforcement is clamped by applying displacements on the two screw parts.

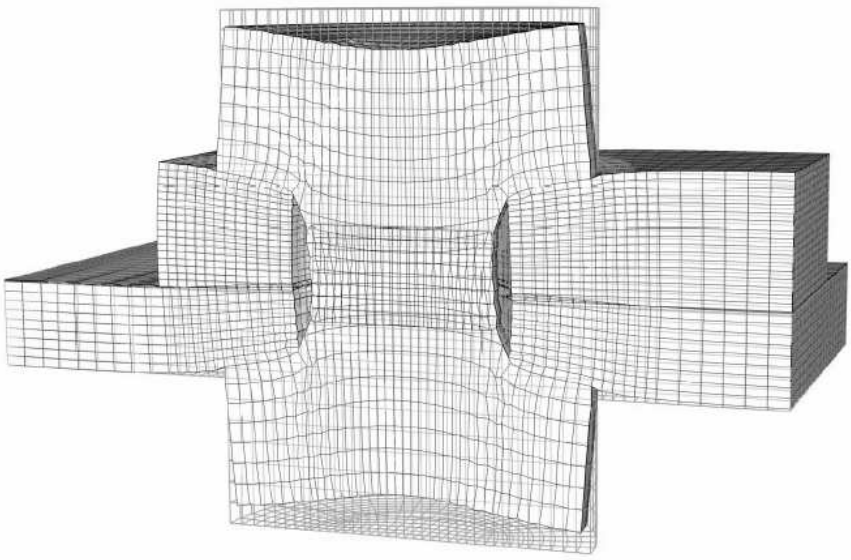

Figure 3.37 Deformed state of the screw joint reinforcement

3.3.1.5 Material data input

The steel parts and the screw are assumed to be made of the same material and are assigned an elastic modulus E = 209 GPa and a Poisson's ratio ν = 0.29. The thermal expansion coefficient is set to $\alpha = 12.5 \cdot 10^{-6} C^{-1}$.

This simulation will only be performed at room temperature and involves a powder coating with a particle volume concentration of 20%. Table 3.9 shows the configuration of the material data input for the coating.

Table 3.9 Initial and final material properties for the powder coating depending on temperature and PVC for the simulation case F

Simulation case	Initial properties	Final properties
F	$[E, \nu]_{t=0,\ 25°C,\ PVC=20\%}$	$[E, \nu]_{t=\infty,\ 25°C,\ PVC=20\%}$

3.3.1.6 Steps

The simulation involves a static step only where the displacements are applied to the two screw parts.

3.3.1.7 Outputs

The requested outputs are the magnitudes of the displacements of the screw and the sum of the reaction forces in the *z*-direction acting on the screw.

3.3.1.8 Procedure

The procedure is more or less the same as in the clamping force loss simulation in section *3.2 Clamping force loss simulation*. The values of the initial elastic properties of the powder coating are used and displacements are applied to the two screw parts. The obtained clamping force is measured and the displacements are adjusted until the desired initial clamping force is obtained.

When this is done the displacements of the screw are kept constant and the elastic properties of the coating are changed to the relaxed values. The obtained clamping force with this configuration is measured and compared with the initial one.

4 RESULTS AND DISCUSSION

It is now time to examine the obtained results from the three types of simulations; the micromechanical simulations and the clamping force loss simulations for the two different screw joint reinforcements.

4.1 MICROMECHANICAL SIMULATIONS

First of all it must be said that it was difficult to obtain good relaxation measurements of the binder material. Several relaxation curves were obtained for every temperature but the distribution of the results was large. A curve that best could describe the average behavior of all curves for a certain temperature was chosen for every temperature. At room temperature relaxation took a long time resulting in fewer measurements. At 100°C the binder relaxes more rapidly but the distribution of the results were larger. The curves obtained at 60°C had the best appearance overall but only one curve was obtained because of lack of time.

Problems occurred while performing relaxation measurements of the powder coatings too. At room temperature the test specimens often broke due to its brittleness. At 100°C the measurements showed a tendency to find a stable asymptotic value but later dropped in steps. As in the case for the binder material, the best curve was obtained at 60°C. Consequently it is desirable to perform more measurements of both the binder and powder coatings to create a sufficient statistical accuracy to make the comparisons between the simulations and experiments just.

The obtained results of the simulated viscoelastic properties of the powder coatings will here be presented for the three different temperatures. At every temperature different initial values of Poisson's ratio for the polyester binder were used to examine its influence on the final results.

The plots for PVC: 10, 15, 20, 25 and 30% in all diagrams show the simulated results for these particle volume concentrations. In the diagrams for the elastic modulus the plot for PVC: 0% represents the experimentally obtained relaxation curve for the binder material. In the diagrams for the bulk and shear moduli and Poisson's ratio, the plot for PVC: 0% represents the calculated values obtained from the experimentally obtained relaxation curve, which was described in section 3.1.2.5.2.

4.1.1 Simulations at 25°C

The results of the simulations at 25°C are presented in this section. Two simulations with different initial values of Poisson's ratio for the polyester binder are shown.

Results of simulations at 25°C, $v_{0,\ \text{binder}}$ = 0.38 and varying particle volume concentration:

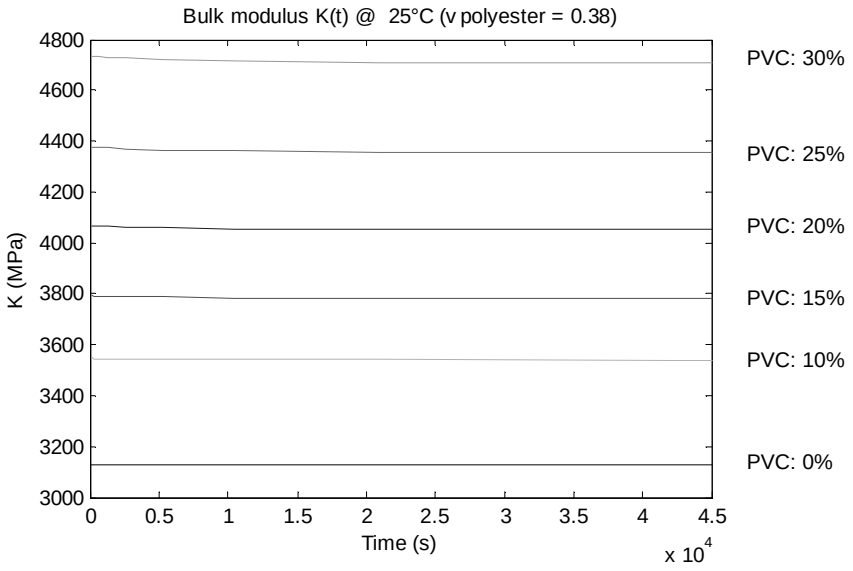

Figure 4.1 Plots of bulk modulus against time for different PVC (the plot for PVC: 0% is calculated from the experimentally obtained result of the binder material while the other plots are simulated)

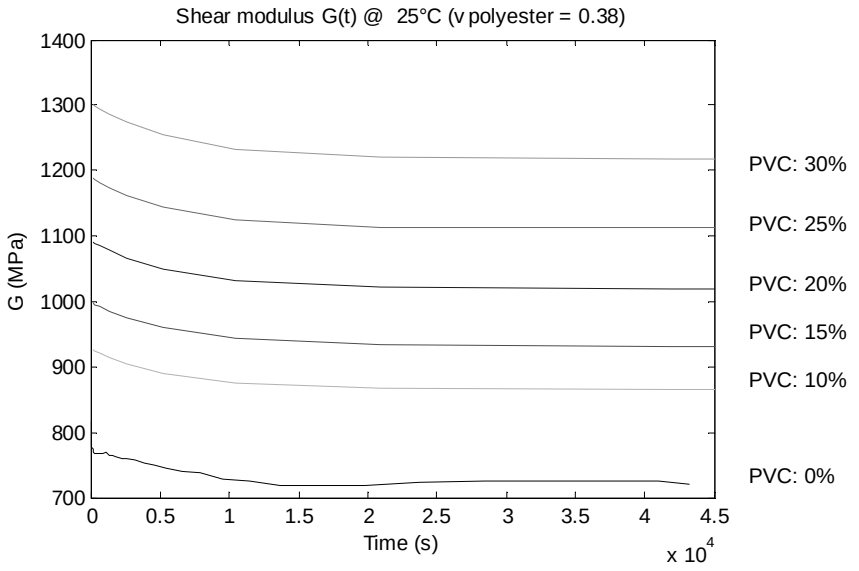

Figure 4.2 Plots of shear modulus against time for different PVC (the plot for PVC: 0% is calculated from the experimentally obtained result of the binder material while the other plots are simulated)

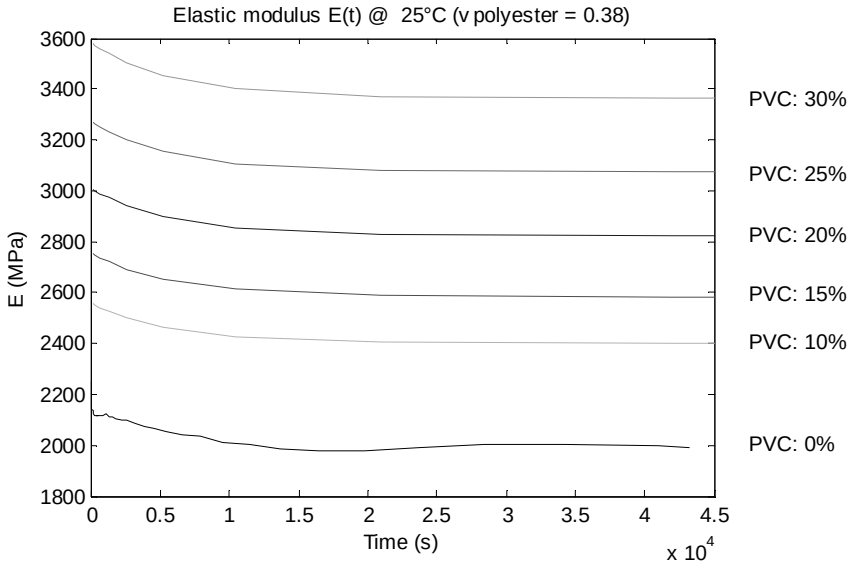

Figure 4.3 Plots of elastic modulus against time for different PVC (the plot for PVC: 0% shows the experimentally obtained result of the binder material while the other plots are simulated results)

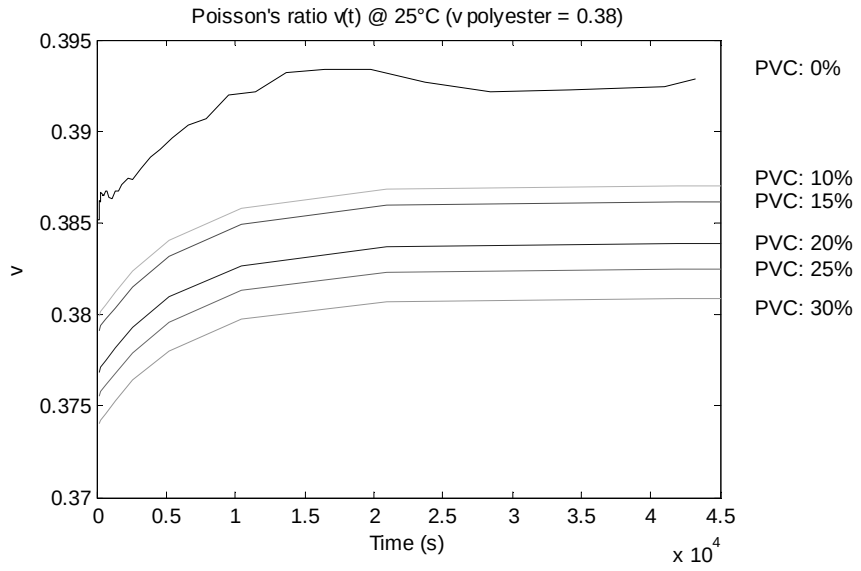

Figure 4.4 Plots of Poisson's ratio against time for different PVC (the plot for PVC: 0% is calculated from the experimentally obtained result of the binder material while the other plots are simulated)

Remarks: As expected the bulk modulus is increased by increased PVC and shows very small time-dependence, while the pure binder shows no time-dependence at all. The shear modulus also shows an increased stiffness for increased PVC and much greater time-dependence than the bulk modulus. The elastic modulus and Poisson's ratio are determined from the bulk and shear moduli and both show great time-dependence. As expected the elastic modulus is increased by increased PVC while Poisson's ratio is decreased, probably due to the lower value of Poisson's ratio for barite.

Results of simulations at 25°C, $v_{0,\ \text{binder}}$ = 0.40 and varying particle volume concentration:

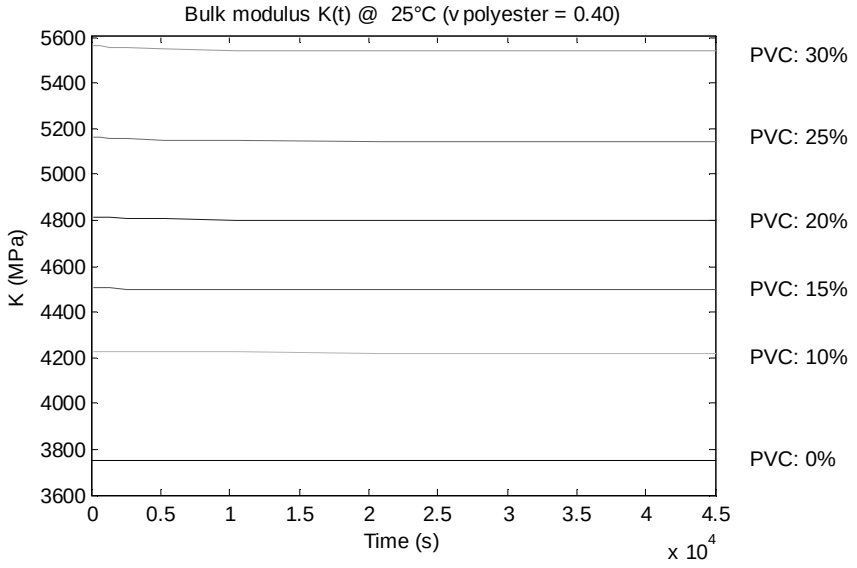

Figure 4.5 Plots of bulk modulus against time for different PVC (the plot for PVC: 0% is calculated from the experimentally obtained result of the binder material while the other plots are simulated)

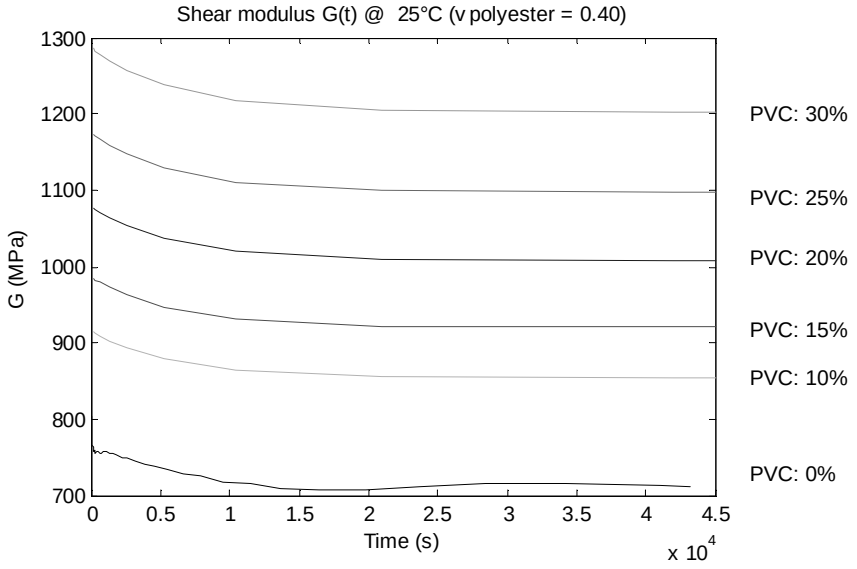

Figure 4.6 Plots of shear modulus against time for different PVC (the plot for PVC: 0% is calculated from the experimentally obtained result of the binder material while the other plots are simulated)

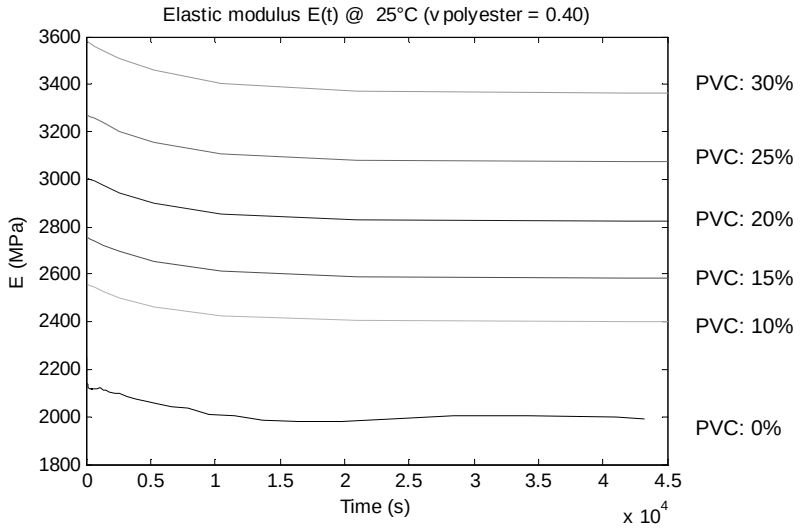

Figure 4.7 Plots of elastic modulus against time for different PVC (the plot for PVC: 0% shows the experimentally obtained result of the binder material while the other plots are simulated results)

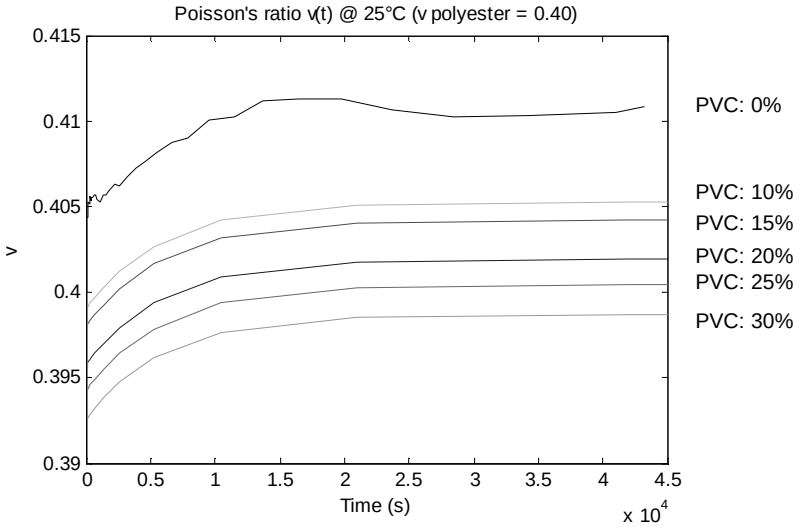

Figure 4.8 Plots of Poisson's ratio against time for different PVC (the plot for PVC: 0% is calculated from the experimentally obtained result of the binder material while the other plots are simulated)

Remarks: All plots are of the same appearance as in the previous simulation. The magnitudes, however, are different and especially the bulk modulus shows a large increase due to the higher Poisson's ratio for the binder material. The shear modulus is slightly decreased while the elastic modulus hardly has changed at all compared to the previous simulation. Poisson's ratio, however, has, of course, increased overall.

4.1.2 Simulations at 100°C

The results of the simulations at 100°C are presented in this section. Two simulations with different initial values of Poisson's ratio for the polyester binder are shown.

Results of simulations at 100°C, $v_{0,\ \text{binder}}$ = 0.38 and varying particle volume concentration:

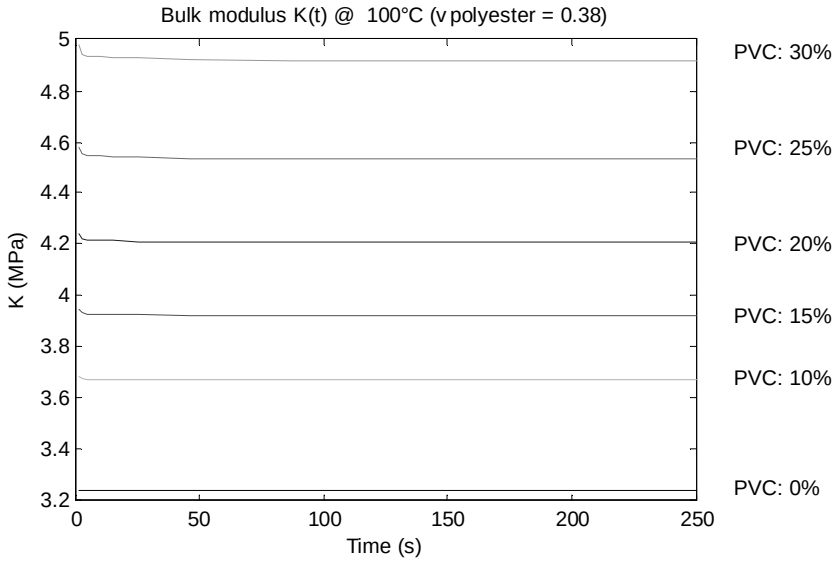

Figure 4.9 Plots of bulk modulus against time for different PVC (the plot for PVC: 0% is calculated from the experimentally obtained result of the binder material while the other plots are simulated)

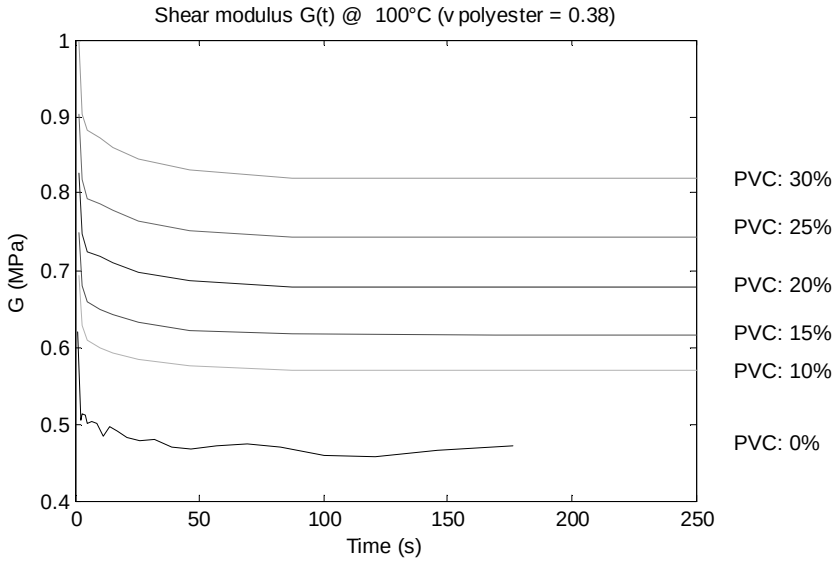

Figure 4.10 Plots of shear modulus against time for different PVC (the plot for PVC: 0% is calculated from the experimentally obtained result of the binder material while the other plots are simulated)

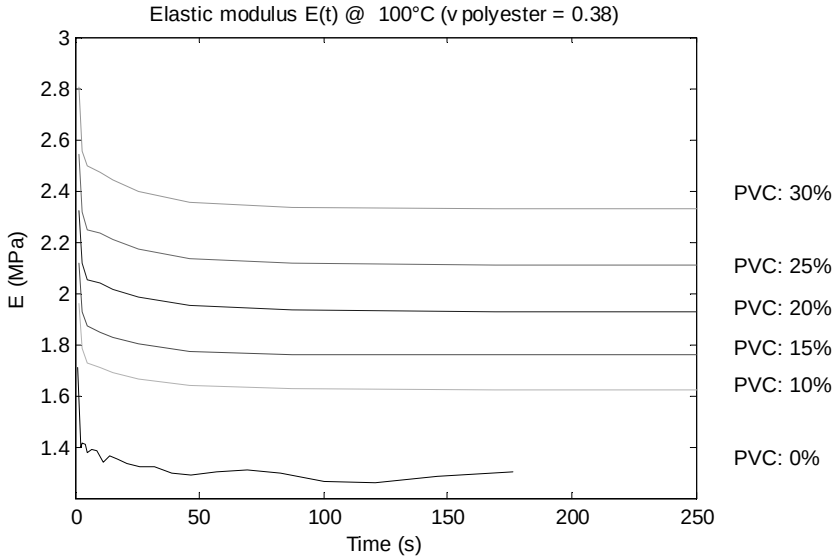

Figure 4.11 Plots of elastic modulus against time for different PVC (the plot for PVC: 0% shows the experimentally obtained result of the binder material while the other plots are simulated results)

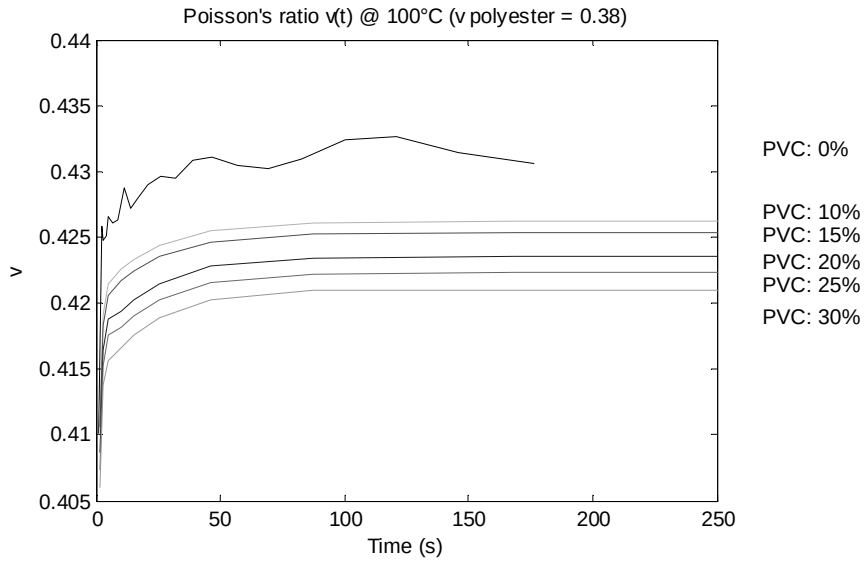

Figure 4.12 Plots of Poisson's ratio against time for different PVC (the plot for PVC: 0% is calculated from the experimentally obtained result of the binder material while the other plots are simulated)

Remarks: The results of the simulations at 100°C follow the same pattern as the results for 25°C but the values are of different magnitudes. Poisson's ratio increases more compared to its initial value compared to the case of 25°C. This is a result of the assumption of a time-independent bulk modulus, which in this case where the relaxation is greater than at 25°C, gives rise to a large long-term value of Poisson's ratio.

Results of simulations at 100°C, $v_{0,\ \text{binder}}$ = 0.40 and varying particle volume concentration:

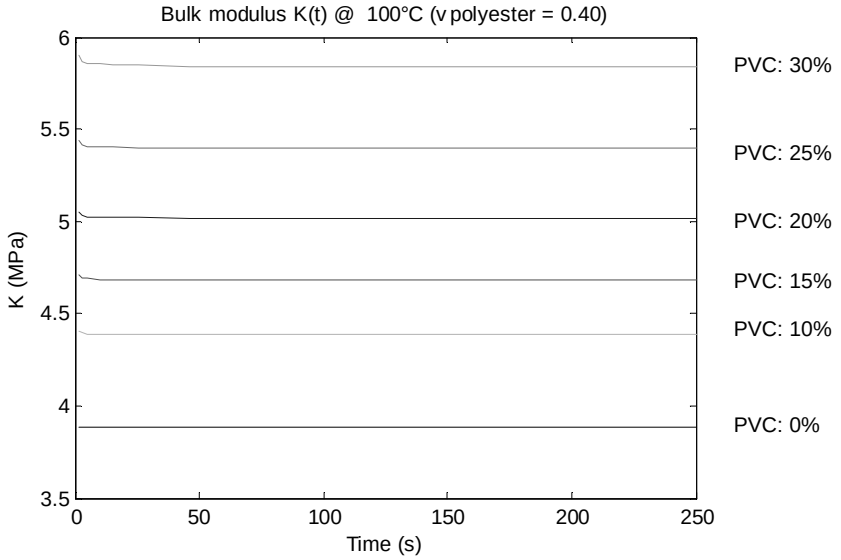

Figure 4.13 Plots of bulk modulus against time for different PVC (the plot for PVC: 0% is calculated from the experimentally obtained result of the binder material while the other plots are simulated)

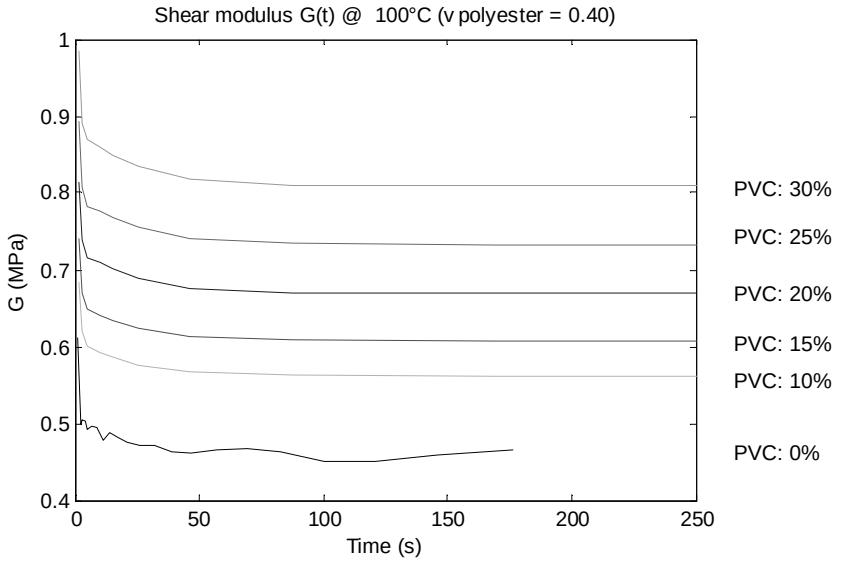

Figure 4.14 Plots of shear modulus against time for different PVC (the plot for PVC: 0% is calculated from the experimentally obtained result of the binder material while the other plots are simulated)

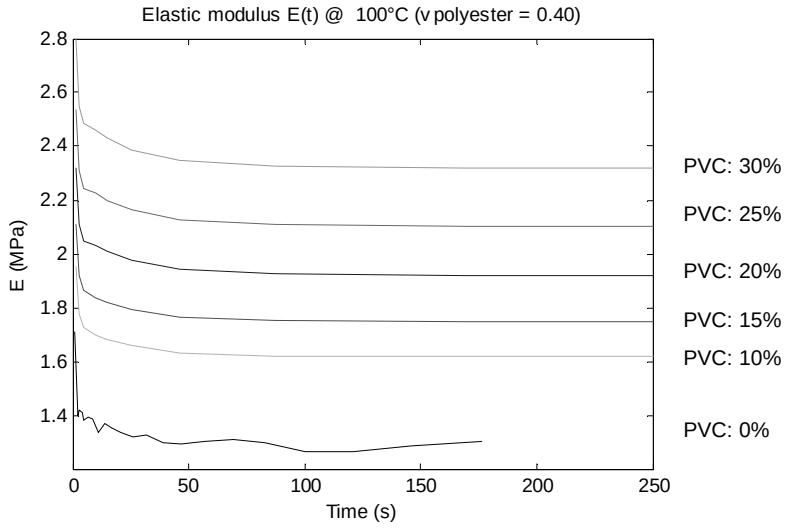

Figure 4.15 Plots of elastic modulus against time for different PVC (the plot for PVC: 0% shows the experimentally obtained result of the binder material while the other plots are simulated results)

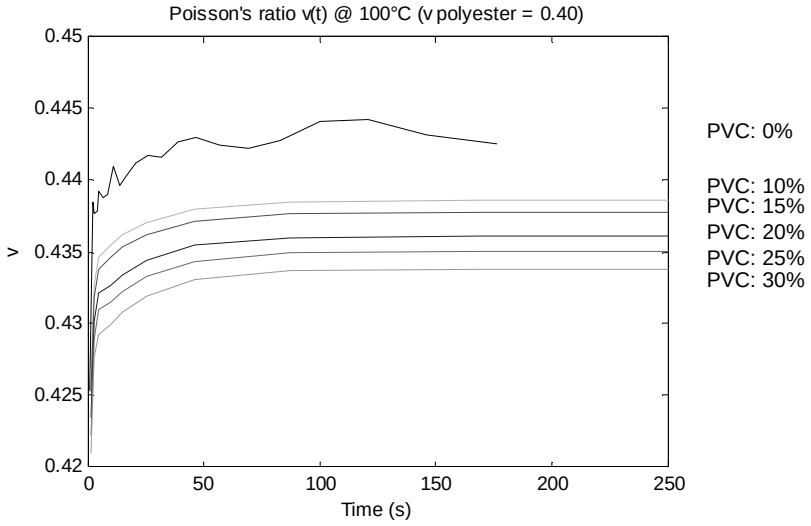

Figure 4.16 Plots of Poisson's ratio against time for different PVC (the plot for PVC: 0% is calculated from the experimentally obtained result of the binder material while the other plots are simulated)

Remarks: All plots have the same appearance as in the previous simulation. The magnitudes, however, are different and especially the bulk modulus shows an increase due to the higher Poisson's ratio for the binder material. The shear modulus is slightly decreased while the elastic modulus hardly has changed at all compared to the previous simulation. Poisson's ratio, however, has, of course, increased overall.

4.1.3 Simulations at 60°C

The results of the simulations at 60°C are presented in this section. Two simulations with different initial values of Poisson's ratio for the polyester binder are shown.

Results of simulations at 60°C, PVC = 25% and varying $\nu_{0,\,\text{binder}}$:

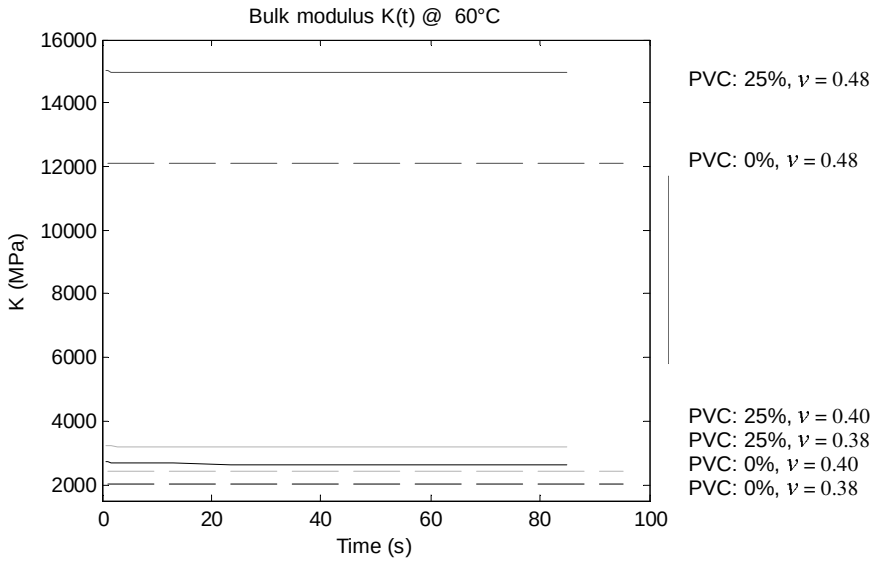

Figure 4.17 Plots of bulk modulus against time for different PVC (the plot for PVC: 0% is calculated from the experimentally obtained result of the binder material while the other plots are simulated)

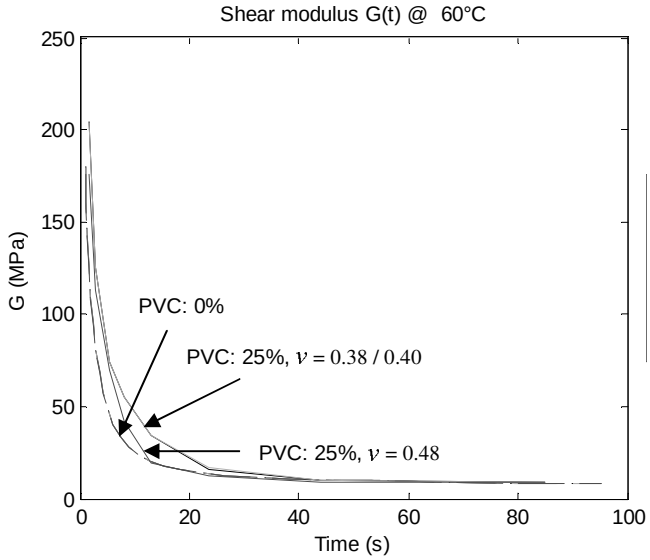

Figure 4.18 Plots of shear modulus against time for different PVC (the plot for PVC: 0% is calculated from the experimentally obtained result of the binder material while the other plots are simulated)

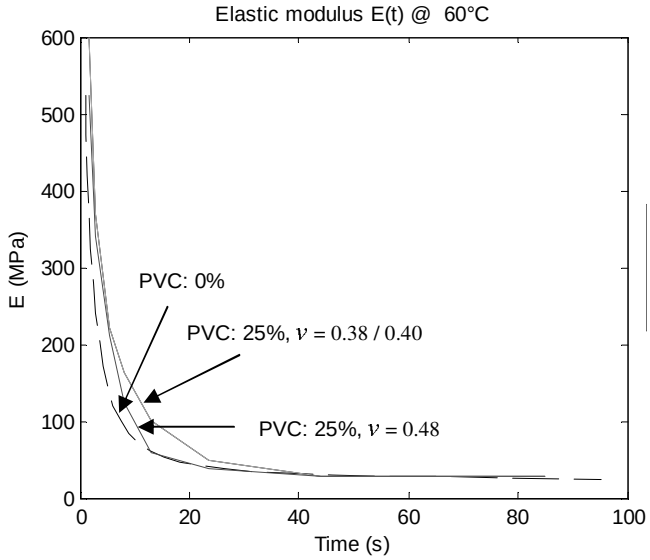

Figure 4.19 Plots of elastic modulus against time for different PVC (the plot for PVC: 0% shows the experimentally obtained result of the binder material while the other plots are simulated results)

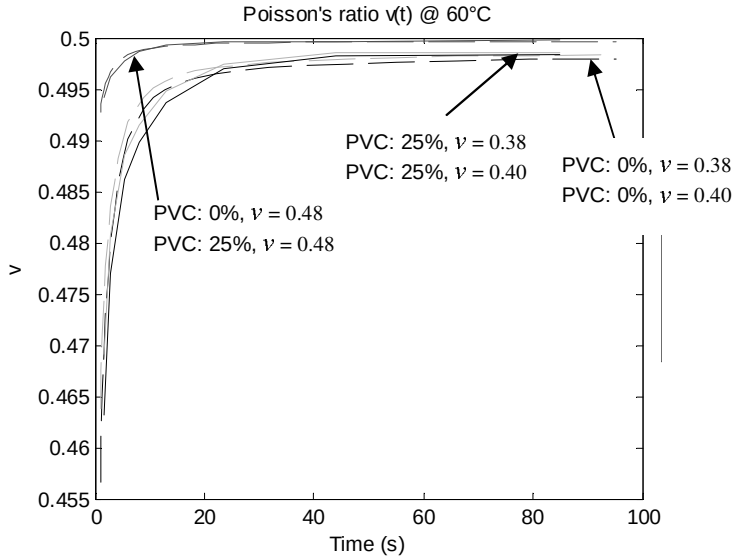

Figure 4.20 Plots of Poisson's ratio against time for different PVC (the plot for PVC: 0% is calculated from the experimentally obtained result of the binder material while the other plots are simulated)

Remarks: The simulation at 60°C was performed differently from the previous ones since only one particle volume concentration (PVC = 25%) was used. This is mainly because of lack of time and that the results will be used in a clamping force loss simulation where the particle volume concentration is supposed to be 25%. The plots show the same pattern as the previous ones but Poisson's ratio for the composite takes a very large magnitude, although the initial value is only 0.38. This is a result of the assumption of a time-independent bulk modulus, which in this case where the relaxation is very strong, gives rise to a large long-term value of Poisson's ratio.

Tables with the most important results from the micromechanical simulations are included in Appendix H. In Appendix I are diagrams of E, K, G and ν for the powder coatings plotted against PVC, to make it easier to see how these parameters are affected by the PVC. These diagrams show only the initial values for 25°C but the relative effects are all the same for the initial and long-term values at any temperature.

4.1.4 Simulations with extreme binders

The results from the simulations with polypropylene and epoxy as binder materials are shown in table 4.1. These simulations were only performed for PVC = 25% and at 25°C.

Table 4.1 Initial and long-term values of the material properties of a powder coating at 25°C and PVC = 25% with two different binder materials

Binder material	Polypropylene	Epoxy
E_0 (25°C) (MPa)	1108	4230
E_∞ (25°C) (MPa)	832	4041
ν_0 (25°C)	0.315	0.370
ν_∞ (25°C)	0.356	0.375

4.1.5 Comparison of results

Comparison with experimental relaxation measurements of the powder coating will be performed for a certain PVC only. The experimentally examined powder coating has a particle volume concentration of 25% and the simulated results for the same PVC are listed in table 4.2 below.

Table 4.2 Simulated initial and long-term values for the elastic modulus of the powder coating, PVC = 25%

Temperature	25°C	60°C	100°C
E_0 (MPa)	3424	2300	3.3
E_∞ (MPa)	3073	27	2.1

Figure 4.21 shows the relaxation curve at 25°C for the powder coating. The initial value is approximately 3850 MPa and the last two points of measuring show the same long-term value; approximately 3350 MPa.

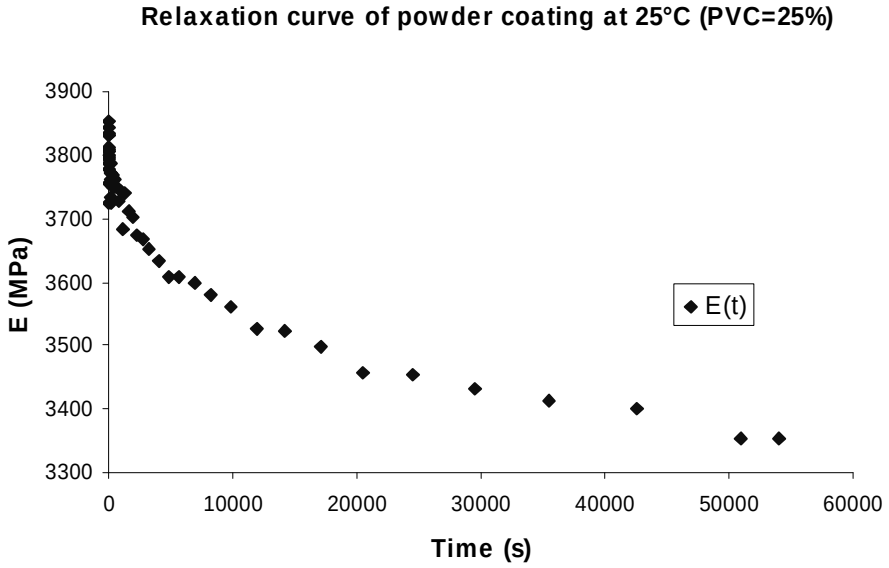

Figure 4.21 Experimentally obtained relaxation curve of powder coating at 25°C (PVC = 25%)

The relaxation measurement at 60°C in figure 4.22 is very neat and shows an initial value of approximately 3500 MPa. A close-up view of the final points of measuring, shown in figure 4.23, shows, however, that the curve does not reach a stable asymptotic value. A long-term value of approximately 60 MPa is assumed, though.

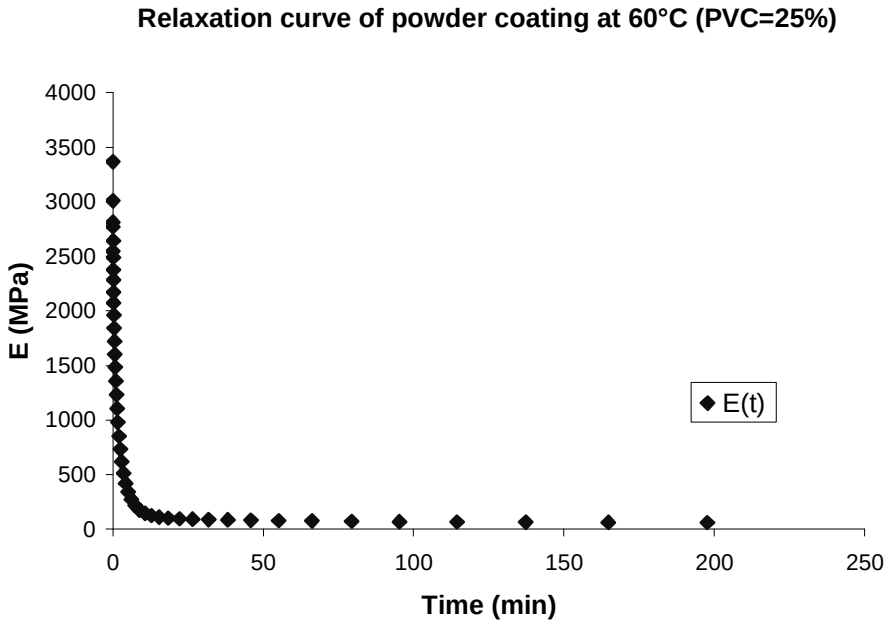

Figure 4.22 Experimentally obtained relaxation curve of powder coating at 60°C (PVC = 25%)

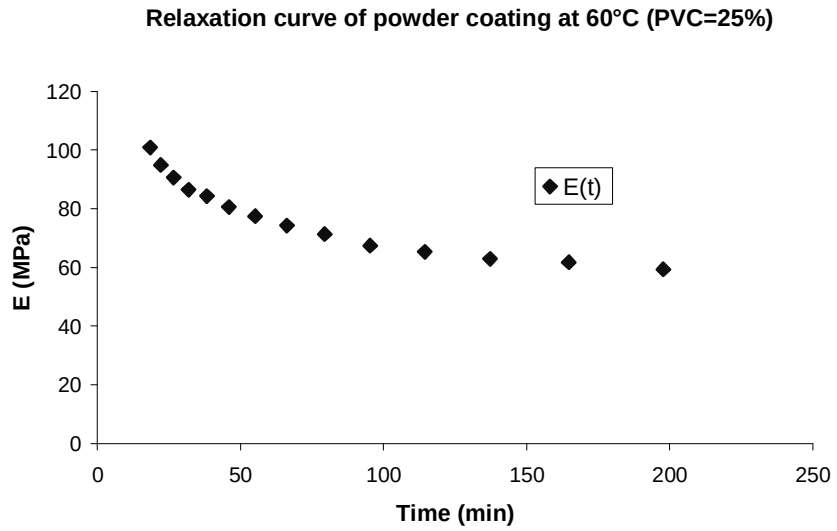

Figure 4.23 The final points of measuring of the curve in figure 4.22

Relaxation measurements of the powder coating at 100°C appeared to be the most difficult one. As shown in figures 4.24 and 4.25 the curves never find a stable asymptotic long-term value. Instead they show how the elastic modulus decreases in steps, which is probably due to mechanical faults by the DMA equipment, cracking of the test specimens or debounding between the particles and the matrix. Consequently it is impossible to establish a long-term value from these two figures. One could, however, imagine that the curves try to level away around 5-6 MPa, marked with the dotted lines in the two figures, before the first step occurs. This value is assumed to be the long-term value of the powder coating at 100°C.

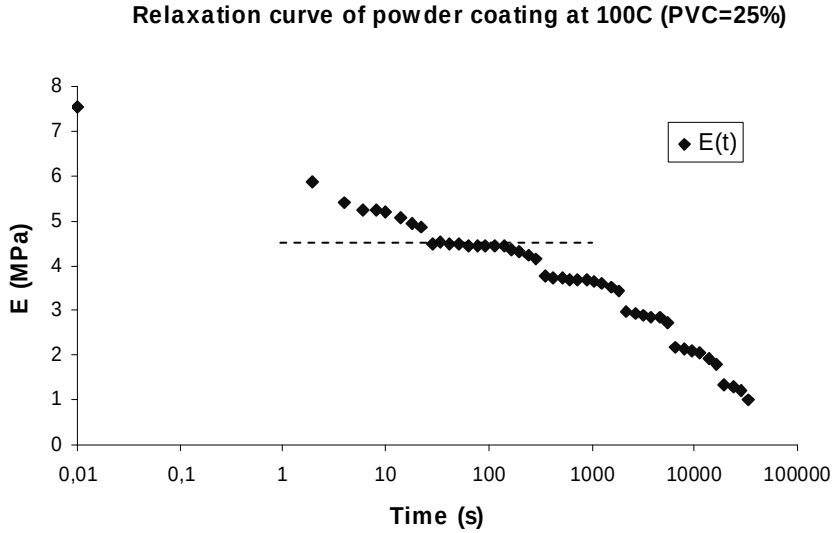

Figure 4.24 Experimentally obtained relaxation curve of powder coating at 100°C (PVC = 25%). The dotted line represents the imagined asymptotic

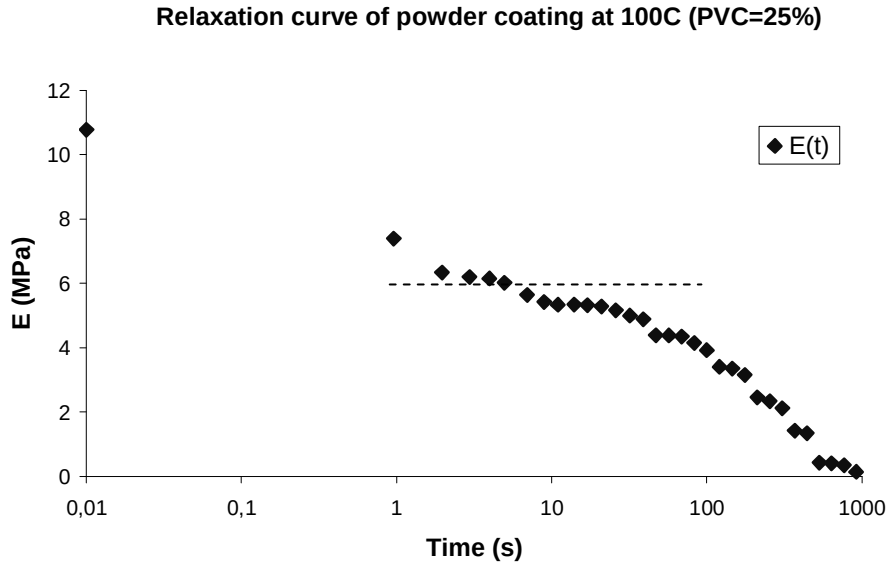

Figure 4.25 A second experimentally obtained relaxation curve of powder coating at 100°C (PVC = 25%). The dotted line represents the imagined asymptotic long-term value

The obtained values are listed in table 4.3 together with the simulated values and the corresponding percentage error.

Table 4.3 Comparison between experimental and simulated initial and long-term values of the powder coatings

Temperature	25°C	60°C	100°C
E_0 (MPa) (experimental)	3840	3370	9
E_0 (MPa) (simulated)	3424	2300	3.3
Error E_0 (%)	10.8	31.8	63.3
E_∞ (MPa) (experimental)	3350	60	5
E_∞ (MPa) (simulated)	3073	27	2.1
Error E_∞ (%)	8.3	55.0	58.0
Relaxation (%) (experimental)	13.0	98.2	44.4
Relaxation (%) (simulated)	10.3	98.8	36.4

Remarks: The accuracy of the simulated results varies a lot, which can be seen in table 4.3. One must remember though, the great distribution of the measurements of the binder material and the powder coating. More relaxation tests must be made to determine material data that is more statistical secure. Only then it is possible to make a just comparison of the

The error is much lower at room temperature than at higher temperatures, which might be due to a greater distribution among the measurements at elevated temperatures. The percentage relaxation of the experimental and simulated results agrees well but is not a result of the model but is more of a verification of the agreement between the relaxation measurements of the binder material and the powder coating.

4.2 CLAMPING FORCE LOSS SIMULATIONS

The results from the clamping force loss simulations are presented for the polyester binder and the two extreme binder materials. Since the glass transition temperature of the polyester binder is approximately 70°C [2] the initial value of Poisson's ratio for the binder is assumed to have the same magnitude below this temperature. But for the simulations at 100°C different initial values of Poisson's ratio will be examined to investigate its influence.

As mentioned in section *3.2.1.5 Material data input*, the simulations containing the polyester binder are performed at different temperatures for particle volume concentrations of 15% and 25%. The simulations containing the extreme binder materials are performed at room temperature only and for a particle volume concentration of 25% and a coating thickness of 110 µm.

The experimental results in this section can be found in [2] and are presented, if there is a corresponding experimental result, for the respective temperature. The initial and long-term values of the material properties are collected from the micromechanical simulations.

4.2.1 Extreme binder materials at 25°C

The values that are presented in table 4.1 were used for this simulation and the final clamping forces for the two cases are listed in table 4.4.

Table 4.4 Clamping force loss results for the two extreme binder materials

Simulation case	B-polypropylene	B-epoxy
Initial clamping force (kN)	54.0	54.0
Final clamping force (kN)	53.67	53.995
Remaining clamping force (%)	99.40	99.99

Remarks: As expected, the loss in clamping force is less for the epoxy powder coating than for the polypropylene coating. The figures, however, can not be verified as no experiments have been performed. Nevertheless, one conclusion is that the magnitude of the clamping force loss for the polyester powder coating should be somewhere between these figures.

4.2.2 Polyester binder at 25°C

Four different setups of the material data were used for the simulations and the values are presented in table 4.5. The two A-cases simulates a PVC of 15% and consist of two versions; A-1 where the initial value of Poisson's ratio for the binder is set to 0.38 and A-2 where the same parameter is set to 0.40. The two B-cases are for PVC = 25% and are divided in the same two sub-cases as for the A-cases. The results from the clamping force loss simulations are presented in table 4.6.

Table 4.5 Material properties for the clamping force simulations at 25°C

Simulation case	A-1	A-2	B-1	B-2
$\nu_{0,\text{ polyester @ 25°C}}$	0.380	0.380	0.380	0.380
$E_{0\text{ @ 25°C}}$	2883	2888	3424	3429
$\nu_{0\text{ @ 25°C}}$	0.374	0.393	0.370	0.390
$\nu_{0,\text{ polyester @ 25°C}}$	0.380	0.380	0.380	0.380
$E_{\infty\text{ @ 25°C}}$	2584	2585	3073	3073
$\nu_{\infty\text{ @ 25°C}}$	0.386	0.404	0.382	0.400

Table 4.6 Simulated clamping force loss results at 25°C

Simulation case	A-1	A-2	B-1	B-2
Initial clamping force (kN)	54.0	54.0	54.0	54.0
Final clamping force (kN)	53.972	53.972	53.974	53.952
Remaining clamping force (%)	99.95	99.95	99.95	99.97

The corresponding experimental results show no loss in clamping force, i.e. the remaining clamping force is 100% of the initial force.

Remarks: The simulated clamping force losses agree very well with the experimental results and are between the upper and lower levels obtained from the extreme binder materials. No major difference is observed between the two different values of the initial value of Poisson's ratio for the polyester binder.

4.2.3 Polyester binder at 100°C

This simulation describes the process when the screw joint reinforcement is tightened at room temperature and then placed in an oven with a temperature of 100°C. The initial value of Poisson's ratio for the polyester binder is set to 0.38 at room temperature but is varied at 100°C. This is done because of the fact that the initial value of Poisson's ratio for the polyester binder is not known at 100°C, and this way it is possible to examine how the final clamping force is influenced by Poisson's ratio.

The initial values of Poisson's ratio that are examined are; 0.38, 0.40, 0.48 and 0.49. This gives the input material properties that are presented in tables 4.7 and 4.8. The results from the clamping force loss simulations are presented in tables 4.9 and 4.10.

Table 4.7 Material properties for the clamping force simulations at 100°C, case: D

Simulation case	D-1	D-2	D-3	D-4
$v_{0,\text{ polyester @ 25°C}}$	0.380	0.380	0.380	0.380
$E_{0\text{ @ 25°C}}$	2883	2883	2883	2883
$v_{0\text{ @ 25°C}}$	0.374	0.374	0.374	0.374
$v_{0,\text{ polyester @ 100°C}}$	0.380	0.400	0.480	0.490
$E_{\infty\text{ @ 100°C}}$	1.69	1.70	1.78	1.75
$v_{\infty\text{ @ 100°C}}$	0.428	0.440	0.488	0.494

Table 4.8 Material properties for the clamping force simulation at 100°C, case: E

Simulation case	E-1	E-2	E-3	E-4
$v_{0,\text{ polyester @ 25°C}}$	0.380	0.380	0.380	0.380
$E_{0\text{ @ 25°C}}$	3424	3424	3424	3424
$v_{0\text{ @ 25°C}}$	0.393	0.393	0.393	0.393
$v_{0,\text{ polyester @ 100°C}}$	0.380	0.400	0.480	0.490
$E_{\infty\text{ @ 100°C}}$	2.04	2.04	2.14	2.11
$v_{\infty\text{ @ 100°C}}$	0.425	0.437	0.487	0.494

Table 4.9 Simulated clamping force loss results at 100°C, case: D

Simulation case	D-1	D-2	D-3	D-4
Initial clamping force (kN)	54	54	54	54
Final clamping force (kN)	3.35	3.85	14.3	21.9
Remaining clamping force (%)	6.2	7.1	26.5	40.6

The experimentally obtained final clamping force for case D (PVC = 15%) is 92% of the initial clamping force [2].

Table 4.10 Simulated clamping force loss results at 100°C, case: E

Simulation case	E-1	E-2	E-3	E-4
Initial clamping force (kN)	54	54	54	54
Final clamping force (kN)	4.01	4.58	16.3	24.3
Remaining clamping force (%)	7.4	8.5	30.1	44.9

The experimentally obtained final clamping force for case E (PVC = 25%) is 96% of the initial clamping force [2].

The results from tables 4.9 and 4.10 are shown together with the experimental results in the diagram in figure 4.26. It is clearly observed that the simulated results do not agree with the experimental results.

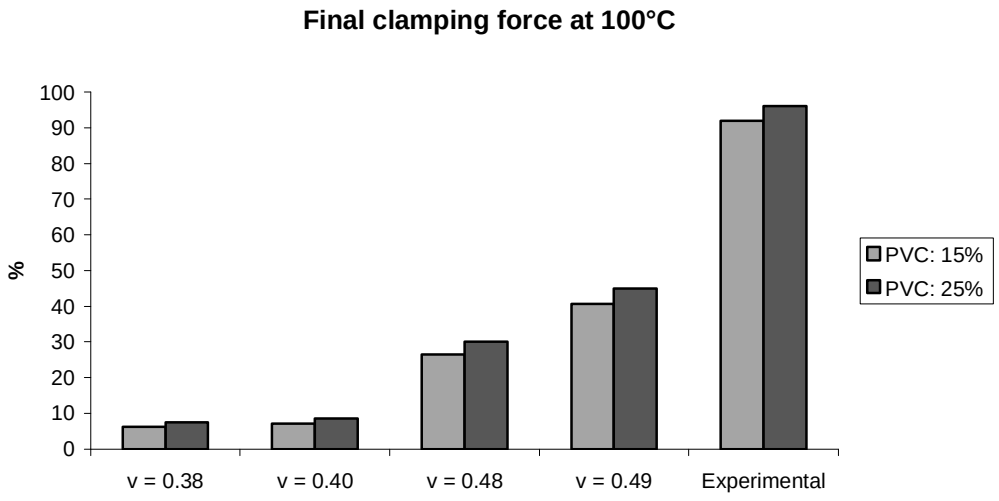

Figure 4.26 Comparison or simulated and experimental clamping force results

Remarks: The simulated results are lower than the experimental results, but once again it is important to emphasize that the relaxation measurements of the binder material are too few to give a statistical security of the material input data.

A problem is that the initial value of Poisson's ratio for the polyester binder is not known at 100°C. In fact, the overall behavior of the binder, including Poisson's ratio, is not known above the glass transition temperature. The initial value of Poisson's ratio for the polyester binder was therefore varied to examine its influence on the final clamping force, and the results are clearly visible in the diagram in figure 4.25. In spite of the fact that Poisson's ratio is chosen to be 0.49, the final clamping force does not even reach 50% of the initial clamping force, while the experimental results are 92% and 96% for PVC = 15% and PVC = 25%, respectively. If Poisson's ratio is close to 0.5, which is the value for rubber for example, a final clamping force that is of the same magnitude as the experimental results can be obtained.

However, if Poisson's ratio for the polyester binder is close to 0.5 at 100°C, even the pure binder would, probably, show a low clamping force loss. This is, however, not the case in reality and the low clamping force loss for the powder coatings must therefore be due to something else than only Poisson's ratio for the binder. Some ideas that could explain this difference are presented below.

Contact might occur between the stiff filler particles due to the low stiffness of the binder material at this temperature. One could imagine that the filler particles are assembled and form a heap that the surfaces of the steel parts rest on.

The powder coating is stabilized by adhesion between the filler particles and the binder. Many small particles give rise to a stiffer composite than large particles, but this model does not distinguish between these two cases.

Thermoplastic sections in the binder material might exist. This causes the pure binder to relax more than the powder coating, and consequently leads to larger losses in the simulations.

The difference in mechanical properties of the powder coating for tensile stress and compressive stress could be a possible explanation of the differences between the simulated and experimental clamping force losses. The step-like drops in the relaxation curves in figures 4.24 and 4.25 could be caused by cracks in the powder coating, cracks that might not appear if the coatings are exposed to a compressive load instead.

4.2.4 Polyester binder at 60°C

This simulation describes the process when the screw joint reinforcement is tightened at room temperature and then placed in an oven with a temperature of 60°C. The initial value of Poisson's ratio for the polyester binder is set to 0.38 and the particle volume concentration is 25%. The material properties that are used as input data are listed in table 4.11, where the initial values represent the properties at room temperature and the final values represent the long-term properties at 60°C.

Table 4.11 Material properties for the clamping force simulation at 60°C

Simulation case	C
$v_{0,\text{ polyester @ 25°C}}$	0.380
$E_{0\text{ @ 25°C}}$	2883
$v_{0\text{ @ 25°C}}$	0.374
$v_{0,\text{ polyester @ 60°C}}$	0.380
$E_{\infty\text{ @ 60°C}}$	27.1
$v_{\infty\text{ @ 60°C}}$	0.498

The results from the clamping force loss simulations are presented in table 4.12 where the final clamping force is listed partly as the result from the material properties and partly as a result from the material properties and also the temperature increase.

Table 4.12 Simulated clamping force loss results at 60°C

Simulation case	C
Initial clamping force (kN)	54.0
Final clamping force (without heating effect)(kN)	53.1
Remaining clamping force (without heating effect) (%)	98.3
Final clamping force (with heating effect)(kN)	54.0
Remaining clamping force (with heating effect) (%)	100

Remarks: No experimental results of this simulation are available and a comparison can therefore not be performed. The increase in clamping force caused by the heating in the simulation is quite strong and it is therefore important to verify the coefficient of thermal expansion for the polyester binder since it can influence results strongly.

Although the relaxation of both the binder and the powder coating is very strong the clamping force loss is very weak in the simulation. This is because of the fact that the bulk modulus is kept constant, which is expressed as a large value of Poisson's ratio for the final material properties in table 4.11. If experiments should show that only a weak clamping force loss occurs at 60°C it might verify that the bulk modulus is in fact constant.

4.3 APPLICATION TO AN EXISTING MODEL

Since the results of the clamping force loss simulations at 100°C were not close to the experimental results it was decided to perform this simulation at room temperature only.

The applied powder coating has a particle volume concentration of 20% and its initial and long-term material properties are listed in table 4.13. Two initial values of Poisson's ratio for the polyester binder were used, namely: 0.38 and 0.40. The results from the simulation are listed in table 4.14.

Table 4.13 Material properties for the clamping force simulation, case: F

Simulation case	F-1	F-2
$\nu_{0,\text{ polyester @ 25°C}}$	0.380	0.400
$E_{0\ @\ 25°C}$	3148	3153
$\nu_{0\ @\ 25°C}$	0.371	0.391
$\nu_{0,\text{ polyester @ 25°C}}$	0.380	0.400
$E_{\infty\ @\ 25°C}$	2824	2824
$\nu_{\infty\ @\ 25°C}$	0.384	0.402

Table 4.14 Simulated clamping force loss results, case: F

Simulation case	F-1	F-2
Initial clamping force (kN)	110	110
Final clamping force (kN)	109.85	109.89
Remaining clamping force (%)	99.86	99.90

Remarks: The results agree well with the results at room temperature presented in the previous section. They also show that the clamping force loss is minimal at room temperature for a screw joint reinforcement with dimensions different from the test equipment that was used in the previous section.

5 CONCLUSIONS

A method that links micromechanics with structural performance has been developed, i.e. a method that starts with an examination of the micromechanical properties of a powder coating and in the end calculates the clamping force loss in a screw joint reinforcement. The method is still in its very first phase but have the potential to be developed further, for example by varying the shape and orientation of the filler particle, which was not managed to accomplish within the time limits of this project.

Since the distribution of the relaxation measurements of the binder material and the powder coating was large, more relaxation measurements must be performed before a just validation of the method can be done. The method has two potential main sources of error; the micromechanical and macromechanical models, where, presumably, the micromechanical model has the strongest influence on the final results. It would help a lot to verify one of the models as the source of error could be isolated and treated in detail.

With the obtained relaxation measurements as starting point, it is, however, observed that the simulated results do not fully agree with the experimental results, neither for the micromechanical case nor the macromechanical case. The simulated results at room temperature, however, are close (micromechanical simulation) to the experimental results or even exactly the same (clamping force loss simulation). One must also keep in mind that the micromechanical model is strongly simplified, mainly by the simplification of the microstructure, the homogenization of the powder coating and the assumption of linear viscoelasticity of the binder material.

The simulated clamping force losses at 100°C are greater than the experimentally obtained ones. This indicates the existence of some properties of the powder coating that the developed method can not simulate. Some ideas that can explain the difference between the simulated and experimental results are presented below:

A. Contact might occur between the stiff filler particles due to the low stiffness of the binder material at this temperature. One could imagine that the filler particles are assembled and form a heap that the surfaces of the steel parts rest on.

B. The powder coating is stabilized by adhesion between the filler particles and the binder. Many small particles give rise to a stiffer composite than large particles, but this method does not distinguish between these two cases.

C. Thermoplastic sections in the binder material might exist. This causes the pure binder to relax more than the powder coating, and consequently leads to larger losses in the simulations.

D. The difference in mechanical properties of the powder coating for tensile stress and compressive stress could be a possible explanation of the differences between the simulated and experimental clamping force losses. The step-like drops in the relaxation curves in figures 4.24 and 4.25 could be caused by cracks in the powder coating, cracks that might not appear if the coatings are exposed to a compressive load instead.

Although the exact figures of the results were not obtained the relative relaxation in the simulated cases show a good accordance with the experimental results, which consequently verifies the relaxation measurements of the binder and powder coating. And in spite of the fact that the figures of the results do not agree it is still possible to examine the relative behavior of a powder coating when the particle volume concentration, Poisson's ratios, binder material, filler material etc. are altered. This way it is possible to relatively compare a number of powder coating structures, and determine the most suitable one for a certain case.

Finally it was shown that it is possible to apply this method to existing FE models and use the method in real FE analyses.

6 FURTHER WORK

The most important task to do next is to perform more material measurements until a sufficient accuracy of the measurements is obtained. Only then it is possible to determine the exactness of the micro- and macromechanical simulations.

Since the polyester binder is in its rubber state at 100°C, above the glass transition temperature, it is difficult to obtain its proper material data, such as Poisson's ratio and coefficient of thermal expansion. It would therefore be better to perform more experiments and simulations at 60°C where the binder acts more stable but still shows a large relaxation.

Only when this is done it would be worth examining different boundary conditions of the unit cell, since their influence is much weaker than the influence from the distribution of the experimental material measurements.

One suggestion is also to extend the analysis by adding oriented filler particles, leading to a non-isotropic behavior of the coating, which is the case for certain fillers, such as wollastonite for example.

7 ACKNOWLEDGMENTS

First of all I would like to thank my supervisor Kristofer Gamstedt at the Department of Solid Mechanics at KTH, not only because of his excellent support and guidance throughout this project, but also for making me feel welcome to the department and making my stay a nice and funny one.

I also would like to thank Eva Iverfeldt and Daniel Ståhlberg at Scania CV AB for accepting me as a Master's thesis student and for making me feel welcome to the company. I also thank Daniel for our discussions and his support and help on the project and report.

Thanks a lot to the people at the Department of Solid Mechanics at KTH who helped me and came up with ideas. No one mentioned, no one forgotten.

And finally, special thanks to my family, my friends and Anna.

8 REFERENCES

[1] Powder Coating Online (2005-03-03) http://www.powdercoatingonline.com/whatispowdercoating.html.

[2] Ståhlberg, Daniel, *Thermoset Polymers and Coatings Subjected to High Compressive Loads*, Licentiate Thesis, 2004.

[3] Atlas Copco (2005-03-03), http://www.atlascopco.com/tools/products/website.nsf/0/2cd20ab5cce54542c1256c5c002fc555/$FILE/Tightening%20technique.pdf.

[4] Tschoegl, Nicholas W., *The Phenomenological Theory of Linear Viscoelastic Behavior: An Introduction*, 1989.

[5] Gudmundson, Peter, *Material Mechanics*, 2004.

[6] McCrum, N. G., Buckley, C. P., Bucknall, C. B., *Principles of Polymer Engineering*, 1988.

[7] Storåkers, Bertil, *Introduktion Till Linjär Viskoelasticitetsteori*, 1977.

[8] Ward, I. M., Hadley, D. W., *An Introduction to the Mechanical Properties of Solid Polymers*, 1993.

[9] *CRC Handbook of Chemistry and Physics*, 2001.

[10] Ravindran, P., Fast, L., Korzhavyi, P. A., Johansson, B., Wills, J., Eriksson, O., *Density Functional Theory for Calculation of Elastic Properties of Orthorhombic Crystals: Application to* $TiSi_2$, Journal of Applied Physics, 1998. 84(9), 4891-4904.

[11] Sundström, Bengt, *Handbok och formelsamling i Hållfasthetslära*, 1999.

[12] Krupička, A., Johansson, M., Hult, A., *Viscoelasticity in Polymer Films on Rigid Substrates*, Macromolecular Materials and Engineering, 2003. 288(2), 108-116.

[13] Qvale, D., Ravi-Chandar, K., *Viscoelastic Characterization of Polymers Under Multiaxial Compression*, Mechanics of Time-Dependent Materials, 2004. 8, 193-214.

[14] Clements, B. E., Mas, E. M., *Dynamic Mechanical Behavior of Filled Polymers. I. Theoretical Developments*, Journal of Applied Physics, 2001. 90(11), 5522-5534.

[15] Kytopoulos, V. N., Bourkas, G. D., Sideridis, E., *Some New Operational Modes and Parameters of Stress Relaxation for the Viscoelastic Characterization of Solid Polymers. I. The "Virtual Modulus" Mode*, Journal of Applied Polymer Science, 2003. 87, 121-137.

[16] Bandyopadhyay, G. G., Bhagawan, S. S., Ninan, K. N., Thomas, Sabu, *Viscoelastic Behavior of Polypropylene/Nitrile Rubber Thermoplastic Elastomer Blends: Application of Kerner's Models for Reactively Compatibilized and Dynamically Vulcanized Systems*, Journal of Polymer Science: Part B: Polymer Physics, 2004. 42, 1417-1432.

[17] Yeong K. Kim and Scott R. White, *Stress Relaxation Behavior of 3501-6 Epoxy Resin During Cure*, Polymer Engineering and Science, 1996. 36(23), 2852-2862.

[18] Hugh A. Bruck - Barry H. Rabin, *An Evaluation of Rule-of-Mixtures Predictions of Thermal Expansion in Powder Processed Ni-Al_2O_3 Composites.*

[19] Uschitsky, M., Suhir, E., Kammlott, G. W., *Thermoelastic Behavior of Filled Molding Compounds: Composite Mechanics Approach*, Journal of Electronic Packaging, 2001. 123, 260-267.

[20] Thomas J. Ahrens, *Mineral Physics & Crystallography: A Handbook of Physical Constants*, 1995.

[21] Rob van der Linde, Eim G. Belder, Dan Y. Perera, *Effect of physical aging and thermal stress on the behavior of polyester/TGIC powder coatings*, Progress in Organic Coatings, 2000. 40, 215-224.

[22] *ABAQUS/Standard User's manual, Version 6.4*, 2002.

[23] Bäcklund, Jonas, *Methods of Plane Fatigue Crack Propagation Analysis in Three Dimensions,* Master's Thesis, 2003.

APPENDIX A

Figures showing the von Mises stress distribution for the hydrostatic and shear models.

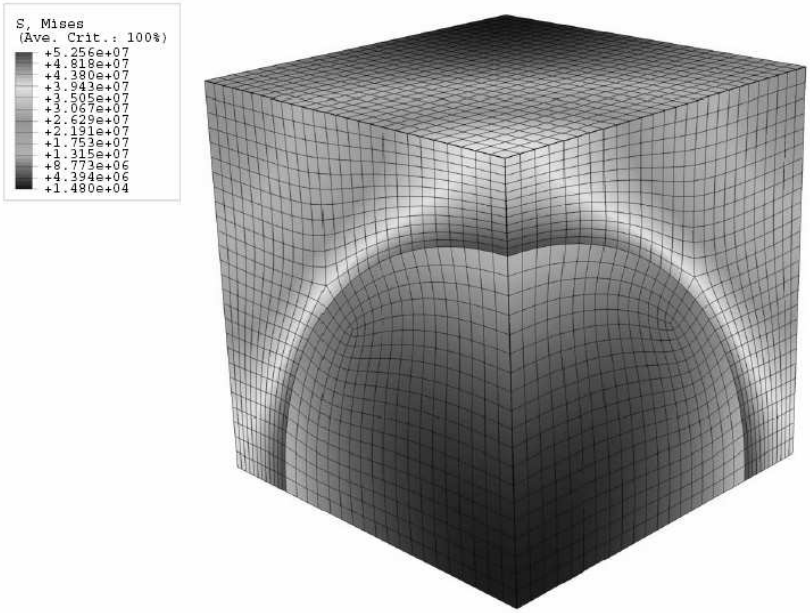

Figure A.1 von Mises stress distribution for the hydrostatic model

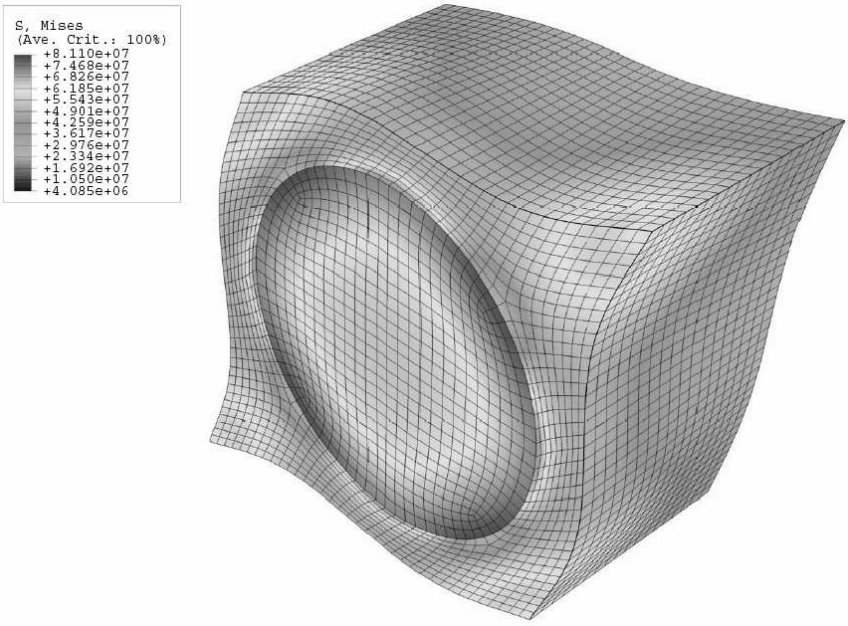

Figure A.2 von Mises stress distribution for the shear model

APPENDIX B

This appendix contains the relaxation curves for the polyester binder at 100°C. The material input parameters that are obtained and calculated from these curves are tabulated too. Section *3.1.2.5.2* describes in detail how these curves are treated and how the parameters are obtained.

Figure B.1 shows the experimentally obtained relaxation curve of the polyester binder at 100°C. The initial value is used straight off for the simulation. An asymptotic long-term value is calculated as the average value of the last points of measuring. With the long-term value added to the relaxation curve it takes the appearance of the curve that is shown in figure B.2.

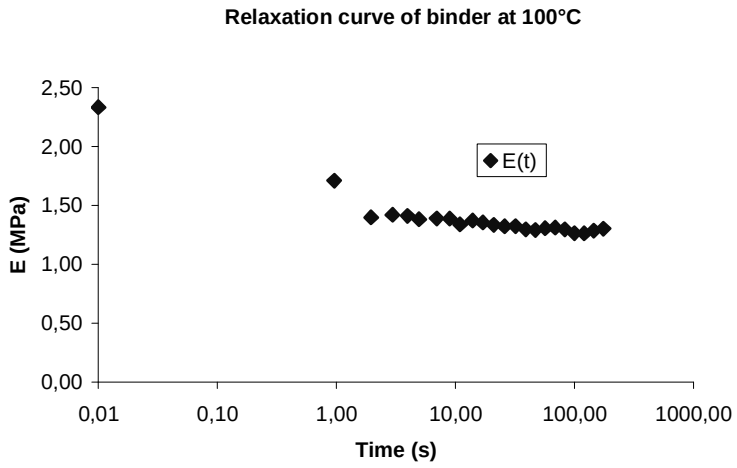

Figure B.1 Relaxation curve of the binder at 100°C

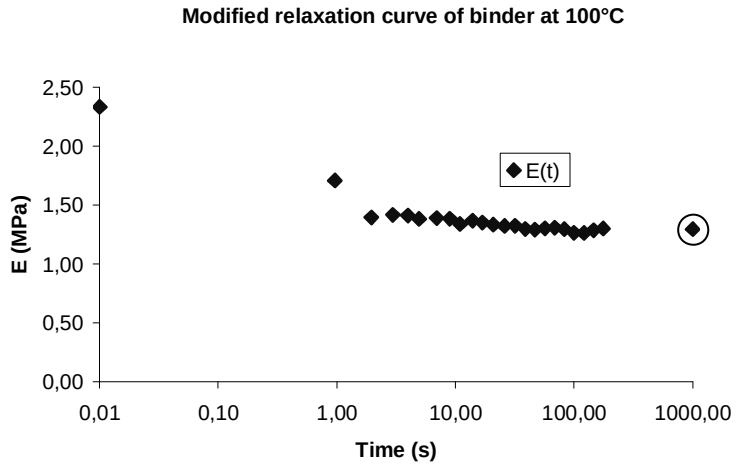

Figure B.2 Modified relaxation curve of the binder at 100°C. The encircled

The material input parameters that are used in the simulations are obtained from the modified relaxation curve. Since the relaxation curves are obtained from uniaxial tension tests they represent the relaxation of the elastic modulus. The input parameters must, however, describe relaxation of the shear modulus and the relaxation data must therefore be transformed. The data from this transformation is presented in the tables B.1 to B.4 where the grey-shaded areas represent the parameters that are actually used in ABAQUS, the other areas are necessary for the calculations though. The parameters are calculated for different initial values of Poisson's ratio for the binder.

Table B.1 Transformed data from E to G using $v = 0.38$ as the initial value of Poisson's ratio for the binder. Grey-shaded areas are used as input parameters in ABAQUS

Time (s)	$E(t)$ (MPa)	$K(t)$ (MPa)	$v(t)$	$G(t)$ (MPa)	$\alpha_i(t)$
0	2.33	3.24	0.3800	0.85	0.999999
1	1.71	3.24	0.4121	0.61	0.715909
2	1.40	3.24	0.4282	0.49	0.578265
3	1.42	3.24	0.4271	0.50	0.587414
4	1.41	3.24	0.4274	0.49	0.584510
5	1.38	3.24	0.4290	0.48	0.571458
7	1.39	3.24	0.4285	0.49	0.575321
9	1.39	3.24	0.4287	0.48	0.573491
11	1.34	3.24	0.4312	0.47	0.552719
14	1.37	3.24	0.4296	0.48	0.566243
17	1.35	3.24	0.4304	0.47	0.559289
21	1.33	3.24	0.4314	0.47	0.550931
26	1.32	3.24	0.4320	0.46	0.545867
32	1.32	3.24	0.4319	0.46	0.546529
39	1.30	3.24	0.4332	0.45	0.535593
47	1.29	3.24	0.4335	0.45	0.533093
57	1.30	3.24	0.4330	0.45	0.538025
69	1.31	3.24	0.4327	0.46	0.540389
83	1.30	3.24	0.4334	0.45	0.534691
100	1.27	3.24	0.4349	0.44	0.521445
121	1.26	3.24	0.4351	0.44	0.519773
146	1.29	3.24	0.4339	0.45	0.530167
176	1.30	3.24	0.4331	0.45	0.537006
∞	1.29	3.24	0.4335	0.45	0.533666

Table B.2 Transformed data from E to G using v = 0.40 as the initial value of Poisson's ratio for the binder. Grey-shaded areas are used as input parameters in ABAQUS

Time (s)	$E(t)$ (MPa)	$K(t)$ (MPa)	$v(t)$	$G(t)$ (MPa)	$\alpha_i(t)$
0	2.33	3.89	0.4000	0.83	0.999999
1	1.71	3.89	0.4267	0.60	0.718827
2	1.40	3.89	0.4402	0.48	0.581770
3	1.42	3.89	0.4393	0.49	0.590897
4	1.41	3.89	0.4395	0.49	0.588000
5	1.38	3.89	0.4408	0.48	0.574978
7	1.39	3.89	0.4404	0.48	0.578833
9	1.39	3.89	0.4406	0.48	0.577007
11	1.34	3.89	0.4427	0.46	0.556274
14	1.37	3.89	0.4413	0.47	0.569774
17	1.35	3.89	0.4420	0.47	0.562832
21	1.33	3.89	0.4429	0.46	0.554488
26	1.32	3.89	0.4434	0.46	0.549432
32	1.32	3.89	0.4433	0.46	0.550093
39	1.30	3.89	0.4444	0.45	0.539171
47	1.29	3.89	0.4446	0.45	0.536673
57	1.30	3.89	0.4441	0.45	0.541600
69	1.31	3.89	0.4439	0.45	0.543961
83	1.30	3.89	0.4445	0.45	0.538269
100	1.27	3.89	0.4458	0.44	0.525035
121	1.26	3.89	0.4459	0.44	0.523364
146	1.29	3.89	0.4449	0.44	0.533750
176	1.30	3.89	0.4442	0.45	0.540582
∞	1.29	3.89	0.4446	0.45	0.537246

Table B.3 Transformed data from E to G using v = 0.48 as the initial value of Poisson's ratio for the binder. Grey-shaded areas are used as input parameters in ABAQUS

Time (s)	$E(t)$ (MPa)	$K(t)$ (MPa)	$v(t)$	$G(t)$ (MPa)	$\alpha_i(t)$
0	2.33	19.44	0.4800	0.79	0.999999
1	1.71	19.44	0.4853	0.58	0.729920
2	1.40	19.44	0.4880	0.47	0.595226
3	1.42	19.44	0.4879	0.48	0.604259
4	1.41	19.44	0.4879	0.47	0.601393
5	1.38	19.44	0.4882	0.46	0.588498
7	1.39	19.44	0.4881	0.47	0.592317
9	1.39	19.44	0.4881	0.47	0.590509
11	1.34	19.44	0.4885	0.45	0.569944
14	1.37	19.44	0.4883	0.46	0.583339
17	1.35	19.44	0.4884	0.45	0.576454
21	1.33	19.44	0.4886	0.45	0.568170
26	1.32	19.44	0.4887	0.44	0.563147
32	1.32	19.44	0.4887	0.44	0.563804
39	1.30	19.44	0.4889	0.44	0.552944
47	1.29	19.44	0.4889	0.43	0.550459
57	1.30	19.44	0.4888	0.44	0.555360
69	1.31	19.44	0.4888	0.44	0.557708
83	1.30	19.44	0.4889	0.44	0.552047
100	1.27	19.44	0.4892	0.42	0.538869
121	1.26	19.44	0.4892	0.42	0.537204
146	1.29	19.44	0.4890	0.43	0.547549
176	1.30	19.44	0.4888	0.44	0.554347
∞	1.29	19.44	0.4889	0.43	0.551028

Table B.4 Transformed data from E to G using $v = 0.49$ as the initial value of Poisson's ratio for the binder. Grey-shaded areas are used as input parameters in ABAQUS

Time (s)	$E(t)$ (MPa)	$K(t)$ (MPa)	$v(t)$	$G(t)$ (MPa)	$\alpha_i(t)$
0	2.33	38.89	0.4900	0.78	0.999999
1	1.71	38.89	0.4927	0.57	0.731246
2	1.40	38.89	0.4940	0.47	0.596848
3	1.42	38.89	0.4939	0.47	0.605869
4	1.41	38.89	0.4940	0.47	0.603006
5	1.38	38.89	0.4941	0.46	0.590128
7	1.39	38.89	0.4940	0.47	0.593943
9	1.39	38.89	0.4941	0.46	0.592136
11	1.34	38.89	0.4943	0.45	0.571594
14	1.37	38.89	0.4941	0.46	0.584975
17	1.35	38.89	0.4942	0.45	0.578097
21	1.33	38.89	0.4943	0.45	0.569822
26	1.32	38.89	0.4943	0.44	0.564803
32	1.32	38.89	0.4943	0.44	0.565460
39	1.30	38.89	0.4944	0.43	0.554608
47	1.29	38.89	0.4945	0.43	0.552125
57	1.30	38.89	0.4944	0.44	0.557023
69	1.31	38.89	0.4944	0.44	0.559369
83	1.30	38.89	0.4944	0.43	0.553712
100	1.27	38.89	0.4946	0.42	0.540542
121	1.26	38.89	0.4946	0.42	0.538878
146	1.29	38.89	0.4945	0.43	0.549217
176	1.30	38.89	0.4944	0.44	0.556011
∞	1.29	38.89	0.4945	0.43	0.552694

APPENDIX C

This appendix contains the relaxation curves for the polyester binder at 60°C. The material input parameters that are obtained and calculated from these curves are tabulated too. Section *3.1.2.5.2* describes in detail how these curves are treated and how the parameters are obtained.

Figure C.1 shows the experimentally obtained relaxation curve for the polyester binder at 60°C. As seen in the figure, the elastic modulus increases in the beginning and decreases later. The increase is not normal and is due to the test equipment and will be disregarded. The measurement is stopped too early to let the binder relax completely but an asymptotic long-term value is estimated. With these modifications the curve that is used in the simulation has the appearance shown in figure C.2.

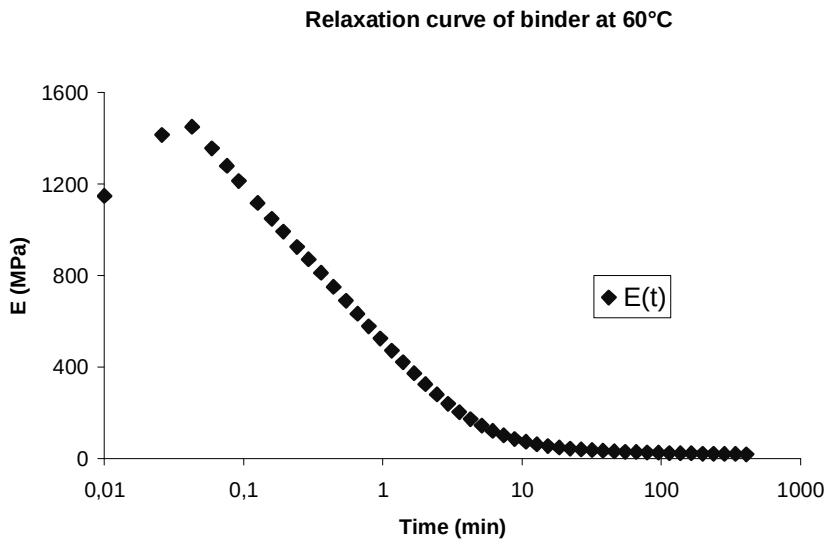

Figure C.1 Relaxation curve of the binder at 100°C

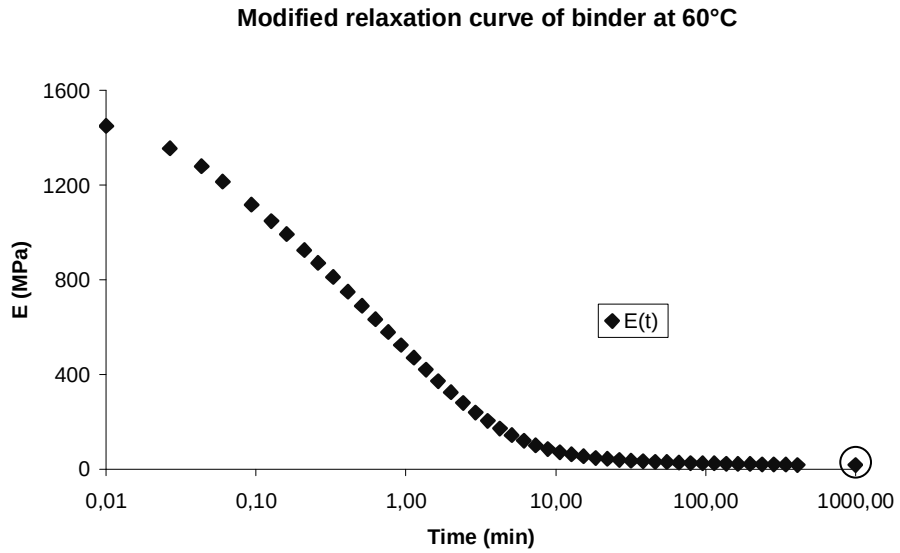

Figure C.2 Modified relaxation curve of the binder at 60°C. The encircled dot represents the relaxed value

The material input parameters that are used in the simulations are obtained from the modified relaxation curve. Since the relaxation curves are obtained from uniaxial tension tests they represent the relaxation of the elastic modulus. The input parameters must, however, describe relaxation of the shear modulus and the relaxation data must therefore be transformed. The data from this transformation is presented in tables C.1 to C.2 where the grey-shaded areas represent the parameters that are actually used in ABAQUS, the other areas are necessary for the calculations though. The parameters are calculated for different initial values of Poisson's ratio for the binder.

Table C.1 Transformed data from E to G using $v = 0.38$ as the initial value of Poisson's ratio for the binder. Grey-shaded areas are used as input parameters in ABAQUS

Time (min)	$E(t)$ (MPa)	$K(t)$ (MPa)	$v(t)$	$G(t)$ (MPa)	$\alpha_i(t)$
0.01	1451	2015	0.3800	526	0.999999
0.03	1356	2015	0.3878	489	0.929766
0.04	1280	2015	0.3941	459	0.873517
0.06	1214	2015	0.3995	434	0.825419
0.09	1118	2015	0.4075	397	0.755399
0.13	1048	2015	0.4133	371	0.705484
0.16	993	2015	0.4179	350	0.665913
0.21	926	2015	0.4234	325	0.618530
0.26	871	2015	0.4279	305	0.580346
0.33	811	2015	0.4329	283	0.538553

0.41	750	2015	0.4380	261	0.496137
0.51	690	2015	0.4429	239	0.454959
0.63	633	2015	0.4476	219	0.415942
0.76	579	2015	0.4521	199	0.379365
0.93	524	2015	0.4566	180	0.342389
1.13	471	2015	0.4611	161	0.306563
1.36	420	2015	0.4652	143	0.272971
1.64	372	2015	0.4693	126	0.240532
1.99	324	2015	0.4732	110	0.209234
2.41	280	2015	0.4768	95	0.180392
2.91	240	2015	0.4802	81	0.154215
3.51	204	2015	0.4832	69	0.130613
4.23	171	2015	0.4858	58	0.109793
5.09	143	2015	0.4881	48	0.091710
6.13	120	2015	0.4901	40	0.076409
7.36	100	2015	0.4917	34	0.063830
8.84	84	2015	0.4930	28	0.053687
10.63	72	2015	0.4941	24	0.045632
12.76	62	2015	0.4949	21	0.039190
15.33	54	2015	0.4956	18	0.034122
18.41	47	2015	0.4961	16	0.030190
22.11	43	2015	0.4965	14	0.027176
26.54	39	2015	0.4968	13	0.024644
31.86	35	2015	0.4971	12	0.022438
38.24	33	2015	0.4973	11	0.020827
45.91	31	2015	0.4975	10	0.019535
55.11	29	2015	0.4976	10	0.018301
66.14	27	2015	0.4978	9	0.017207
79.39	26	2015	0.4979	9	0.016423
95.29	25	2015	0.4980	8	0.015619
114.36	23	2015	0.4981	8	0.014837
137.24	23	2015	0.4981	8	0.014411
164.71	21	2015	0.4982	7	0.013638
197.66	21	2015	0.4983	7	0.013188
237.21	20	2015	0.4983	7	0.012744
284.66	19	2015	0.4984	6	0.012330
341.61	19	2015	0.4984	6	0.011921
409.94	18	2015	0.4985	6	0.011267
∞	17	2015	0.4986	6	0.010791

Table C.2 Transformed data from E to G using $\nu = 0.40$ as the initial value of Poisson's ratio for the binder. Grey-shaded areas are used as input parameters in ABAQUS

Time (min)	$E(t)$ (MPa)	$K(t)$ (MPa)	$\nu(t)$	$G(t)$ (MPa)	$\alpha_i(t)$
0.01	1451	2418	0.4000	518	0.999999
0.03	1356	2418	0.4065	482	0.930700
0.04	1280	2418	0.4118	453	0.875098
0.06	1214	2418	0.4163	429	0.827483
0.09	1118	2418	0.4230	393	0.758048
0.13	1048	2418	0.4277	367	0.708465
0.16	993	2418	0.4316	347	0.669106
0.21	926	2418	0.4362	322	0.621920
0.26	871	2418	0.4399	303	0.583846
0.33	811	2418	0.4441	281	0.542127
0.41	750	2418	0.4483	259	0.499734
0.51	690	2418	0.4524	238	0.458529
0.63	633	2418	0.4564	217	0.419442
0.76	579	2418	0.4601	198	0.382759
0.93	524	2418	0.4639	179	0.345636
1.13	471	2418	0.4675	160	0.309630
1.36	420	2418	0.4710	143	0.275836
1.64	372	2418	0.4744	126	0.243170
1.99	324	2418	0.4777	110	0.211624
2.41	280	2418	0.4807	95	0.182530
2.91	240	2418	0.4835	81	0.156102
3.51	204	2418	0.4860	69	0.132256
4.23	171	2418	0.4882	58	0.111207
5.09	143	2418	0.4901	48	0.092915
6.13	120	2418	0.4917	40	0.077431
7.36	100	2418	0.4931	34	0.064696
8.84	84	2418	0.4942	28	0.054423
10.63	72	2418	0.4951	24	0.046263
12.76	62	2418	0.4958	21	0.039736
15.33	54	2418	0.4963	18	0.034600
18.41	47	2418	0.4967	16	0.030614
22.11	43	2418	0.4971	14	0.027559
26.54	39	2418	0.4973	13	0.024993
31.86	35	2418	0.4976	12	0.022756
38.24	33	2418	0.4977	11	0.021123
45.91	31	2418	0.4979	10	0.019812
55.11	29	2418	0.4980	10	0.018562
66.14	27	2418	0.4981	9	0.017453
79.39	26	2418	0.4982	9	0.016657

95.29	25	2418	0.4983	8	0.015842
114.36	23	2418	0.4984	8	0.015048
137.24	23	2418	0.4984	8	0.014617
164.71	21	2418	0.4985	7	0.013832
197.66	21	2418	0.4986	7	0.013377
237.21	20	2418	0.4986	7	0.012926
284.66	19	2418	0.4987	6	0.012507
341.61	19	2418	0.4987	6	0.012091
409.94	18	2418	0.4988	6	0.011428
∞	17	2418	0.4988	6	0.010945

APPENDIX D

Table D.1 Transformed data from E to G using $v = 0.40$ as the initial value of Poisson's ratio for the binder. Grey-shaded areas are used as input parameters in ABAQUS

Time (s)	$E(t)$ (MPa)	$K(t)$ (MPa)	$v(t)$	$G(t)$ (MPa)	$\alpha_i(t)$
0	2251	3751	0.4000	804	0.999999
2	2237	3751	0.4006	799	0.993381
4	2227	3751	0.4011	795	0.988646
6	2218	3751	0.4015	791	0.984474
10	2209	3751	0.4019	788	0.979953
14	2201	3751	0.4022	785	0.976217
18	2198	3751	0.4023	784	0.975083
24	2194	3751	0.4025	782	0.973053
30	2188	3751	0.4028	780	0.970402
38	2177	3751	0.4033	776	0.965055
48	2167	3751	0.4037	772	0.960390
60	2160	3751	0.4040	769	0.956839
74	2163	3751	0.4039	770	0.958273
90	2150	3751	0.4045	765	0.952117
110	2146	3751	0.4047	764	0.950315
134	2146	3751	0.4046	764	0.950362
162	2139	3751	0.4050	761	0.947147
196	2124	3751	0.4056	755	0.939810
238	2126	3751	0.4055	756	0.941057
288	2116	3751	0.4060	753	0.936151
348	2122	3751	0.4057	755	0.938753
420	2119	3751	0.4059	754	0.937563
506	2119	3751	0.4059	754	0.937525
610	2115	3751	0.4060	752	0.935538
734	2115	3751	0.4060	752	0.935580
882	2120	3751	0.4058	754	0.938191
1060	2123	3751	0.4057	755	0.939659
1274	2114	3751	0.4061	752	0.935259
1530	2114	3751	0.4061	752	0.935326
1838	2107	3751	0.4064	749	0.931943
2208	2100	3751	0.4067	746	0.928401
2652	2101	3751	0.4067	747	0.928985
3184	2089	3751	0.4072	742	0.923178
3822	2077	3751	0.4077	738	0.917691
4588	2068	3751	0.4081	734	0.913333
5508	2057	3751	0.4086	730	0.908097

7936	2034	3751	0.4096	722	0.897628
9526	2009	3751	0.4107	712	0.885856
11434	2005	3751	0.4109	710	0.883808
13722	1984	3751	0.4119	703	0.873958
16468	1981	3751	0.4120	701	0.872634
19764	1981	3751	0.4120	701	0.872652
23718	1994	3751	0.4114	707	0.878982
28464	2005	3751	0.4109	710	0.883738
34158	2003	3751	0.4110	710	0.882857
40992	2000	3751	0.4111	709	0.881723
43194	1990	3751	0.4116	705	0.876987
∞	1994	3751	0.4114	706	0.878592

APPENDIX E

This appendix includes an example of the program code that collects and treats the results from the dat-files that are generated by ABAQUS. The program code must be modified depending on properties of the dat-files.

```
%% Reads the dat-file for the hydrostatic simulation of
%% PVC=25% at temperature=60C. Creates a vector with all
%% time increments in the simulation.

[status, output_rows]=dos('find /N "TOTAL TIME COMPLETED"
C:\junestam\slutlig\Hydro25_60C_relaxation.dat');
n=1;
i=1;
while n<length(output_rows)
    if output_rows(n)=='['
        k=n;
        t(i)=str2num(output_rows([k+70:k+83]));
        i=i+1;
    end
    n=n+1;
end


%% Collects the sums of the reaction forces RF1, RF2 and
%% RF3 from the same dat-file as above for all time
%% increments

[status, output_rows]=dos('find /N " TOTAL        -"
C:\junestam\slutlig\Hydro25_60C_relaxation.dat');
n=1;
i=1;
while n<length(output_rows)
    if output_rows(n)=='['
        k=n;
        f(i)=str2num(output_rows([k+20:k+32]));
        i=i+1;
    end
    n=n+1;
end


%% Transforms the forces into stresses by dividing the
%% forces by the surface area of the unit cell

s=f/(50*50);


%% Sorts the stress components s11, s22 and s33 into
%% individual vectors

k=1;
i=1;
```

```
    s11(i)=s(k);
    i=i+1;
    k=k+3;
end

k=2;
i=1;
for q=1:length(t)
    s22(i)=s(k);
    i=i+1;
    k=k+3;
end

k=3;
i=1;
for q=1:length(t)
    s33(i)=s(k);
    i=i+1;
    k=k+3;
end


%% Calculates K(t) for every time increment with
%% equation 3.1 in the report (MPa)

i=1;
for q=1:length(t)
    K(i)=(s11(i)+s22(i)+s33(i))/(3e6*(-0.01+(-0.01)+(-
0.01)));
    i=i+1;
end


%% Reads the dat-file for the shear simulation of
%% PVC=25% at temperature=60C. Collects the sums of the
%% reaction forces for all time increments in the
%% simulation

dat=fopen('Shear25_60C_relaxation.dat');
tline=fgetl(dat);
j=1;
while ~feof(dat)
    tline=fgetl(dat);
    if length(tline)==82 & tline='   THE FOLLOWING TABLE
IS PRINTED FOR NODES BELONGING TO NODE SET
ASSEMBLY_SIGMA12'

        for i=1:715
            tline=fgetl(dat);
        end
        f(j)=str2num(tline(16:25));
        j=j+1;
    end
end
fclose(dat);
```

```
%% Transforms the forces into stresses by dividing the
%% forces by the surface area of the unit cell

s=f/(100*50);


%% Calculates G(t) for every time increment with
%% equation 2.31 %% in the report (MPa)

i=1;
for q=1:length(t)
    G(q)=s(q)/(2e6*0.01);
end


%% Calculates E(t) for every time increment with
%% equation 3.2 in the report (MPa)

i=1;
for i=1:length(t)
    E(i)=(9*G4(i)*K(i))/(3*K(i)+G(i));
end


%% Calculates v(t) for every time increment with
%% equation 2.19 %% in the report

i=1;
for i=1:length(t)
    v(i)=(3*K(i)-2*G(i))/(2*(3*K(i)+G(i)));
end
```

APPENDIX F

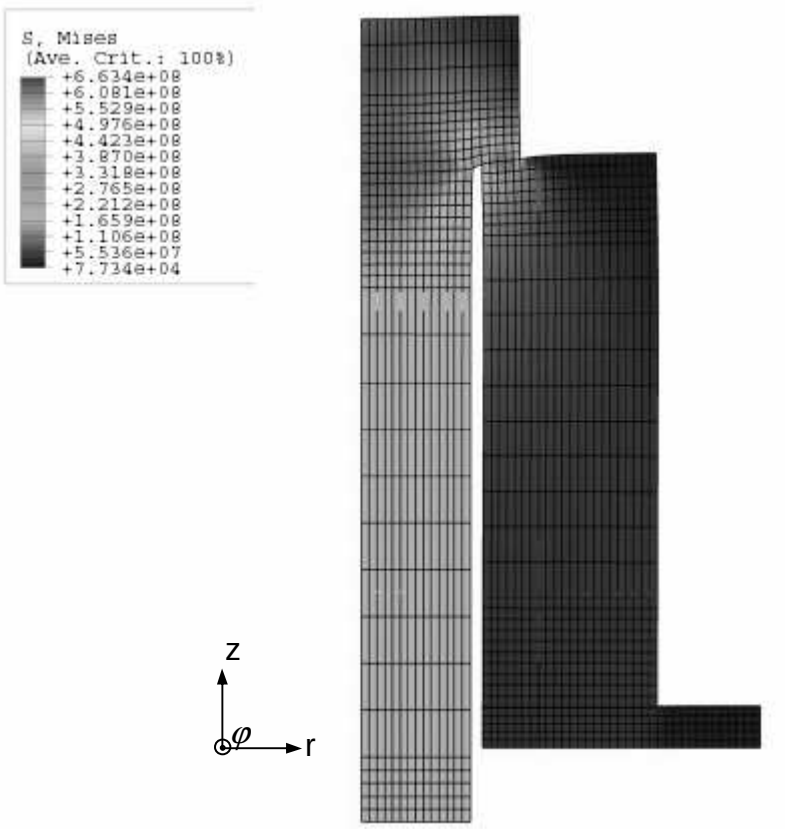

Figure F.1 von Mises stress distribution for the screw joint reinforcement used in section 3.2

APPENDIX G

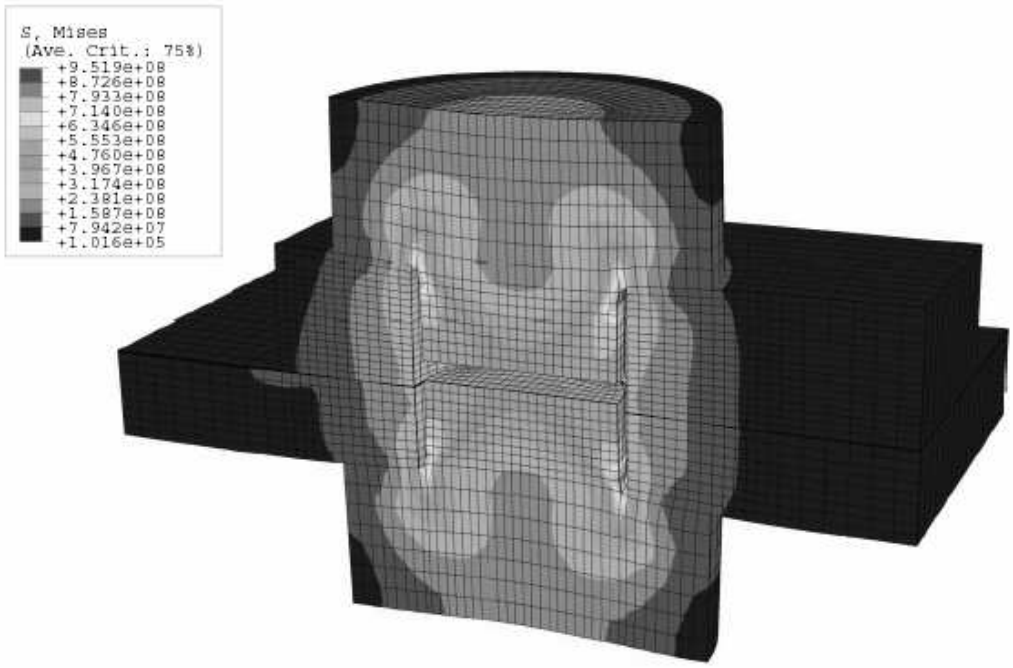

Figure G.1 von Mises stress distribution for the screw joint reinforcement used in section 3.3

APPENDIX H

Most results from the micromechanical simulations with the polyester binder material are presented in tables H.1 to H.4 in this appendix. Since the main interest is to use the initial values at room temperature and the long-term values at the other temperatures, only these values are tabulated.

Table H.1 Initial and long-term values of the material properties of the powder coating for different values of PVC and at different temperatures. The initial value of Poisson's ratio for the polyester binder is 0.38

PVC (%)	10	15	20	25	30
K_0 (25°C) (MPa)	3553	3801	4078	4392	4753
K_∞ (25°C) (MPa)	3541	3783	4053	4358	4709
K_∞ (100°C) (MPa)	3.67	3.92	4.20	4.53	4.90
K_∞ (60°C) (MPa)				2654	
G_0 (25°C) (MPa)	975	1050	1148	1249	1369
G_∞ (25°C) (MPa)	865	932	1020	1111	1218
G_∞ (100°C) (MPa)	0.55	0.59	0.65	0.71	0.79
G_∞ (60°C) (MPa)				9.06	
E_0 (25°C) (MPa)	2679	2883	3148	3424	3746
E_∞ (25°C) (MPa)	2401	2584	2824	3073	3365
E_∞ (100°C) (MPa)	1.57	1.69	1.86	2.04	2.25
E_∞ (60°C) (MPa)				27.1	
v_0 (25°C)	0.374	0.374	0.371	0.370	0.369
v_∞ (25°C)	0.387	0.386	0.384	0.382	0.381
v_∞ (100°C)	0.429	0.428	0.426	0.425	0.424
v_∞ (60°C)				0.498	

Table H.2 Initial and long-term values of the material properties of the powder coating for different values of PVC and at different temperatures. The initial value of Poisson's ratio for the polyester binder is 0.40

PVC (%)	10	15	20	25	30
K_0 (25°C) (MPa)	4233	4513	4824	5176	5579
K_∞ (25°C) (MPa)	4222	4495	4800	5143	5537
K_∞ (100°C) (MPa)	4.39	4.68	5.01	5.39	5.83
K_∞ (60°C) (MPa)				3176	
G_0 (25°C) (MPa)	962	1036	1133	1234	1351
G_∞ (25°C) (MPa)	854	920	1007	1097	1202
G_∞ (100°C) (MPa)	0.54	0.59	0.65	0.71	0.78
G_∞ (60°C) (MPa)				9.05	
E_0 (25°C) (MPa)	2683	2888	3153	3429	3752
E_∞ (25°C) (MPa)	2401	2585	2824	3073	3365
E_∞ (100°C) (MPa)	1.57	1.70	1.86	2.04	2.25
E_∞ (60°C) (MPa)				27.1	
v_0 (25°C)	0.394	0.393	0.391	0.390	0.388
v_∞ (25°C)	0.405	0.404	0.402	0.400	0.399
v_∞ (100°C)	0.440	0.440	0.438	0.437	0.436
v_∞ (60°C)				0.499	

Table H.3 Long-term values of the material properties of the powder coating with a PVC of 15% at 100°C. The following initial values of Poisson's ratio for the polyester binder are used: 0.48 and 0.49

PVC (%)	15	15
$v_{0,\ polyester}$	0.48	0.49
K_∞ (100°C) (MPa)	24.9	47.7
G_∞ (100°C) (MPa)	0.60	0.59
E_∞ (100°C) (MPa)	1.78	1.75
v_∞ (100°C)	0.488	0.494

Table H.4 Long-term values of the material properties of the powder coating with a PVC of 25% at 100°C. The following initial values of Poisson's ratio for the polyester binder are used: 0.48 and 0.49

PVC (%)	25	25
$v_{0,\ polyester}$	0.48	0.49
K_∞ (100°C) (MPa)	28.3	54.2
G_∞ (100°C) (MPa)	0.72	0.71
E_∞ (100°C) (MPa)	2.14	2.11
v_∞ (100°C)	0.487	0.494

APPENDIX I

The mechanical properties of the powder coatings are plotted against PVC for two different initial values of Poisson's ratio for the polyester binder. The diagrams confirm the observations in section 4.1 where it is concluded that the two different initial values of Poisson's ratio for the polyester binder barely affect *G* and *E* of the powder coating, but has a strong affect on *K* and *v*.

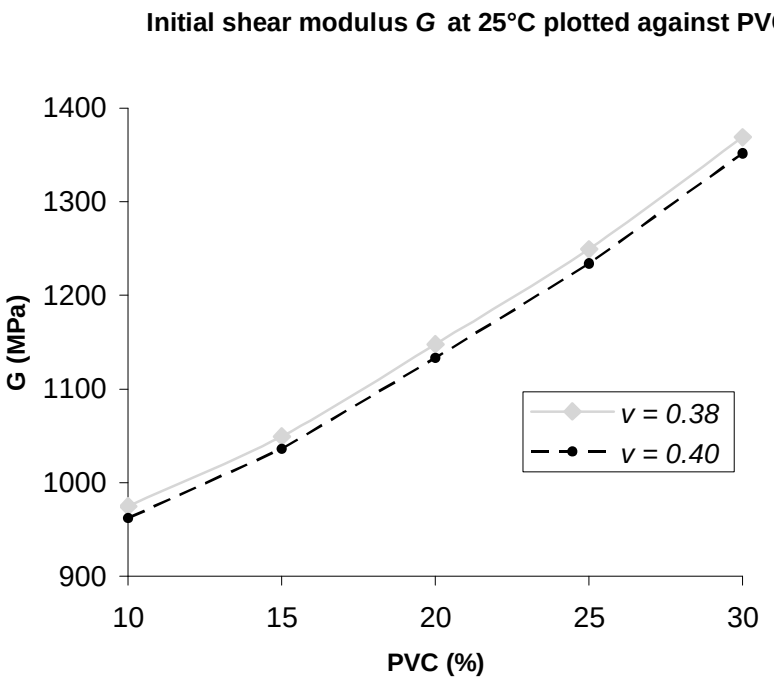

Figure I.1 Initial shear modulus *G* at 25°C plotted against PVC

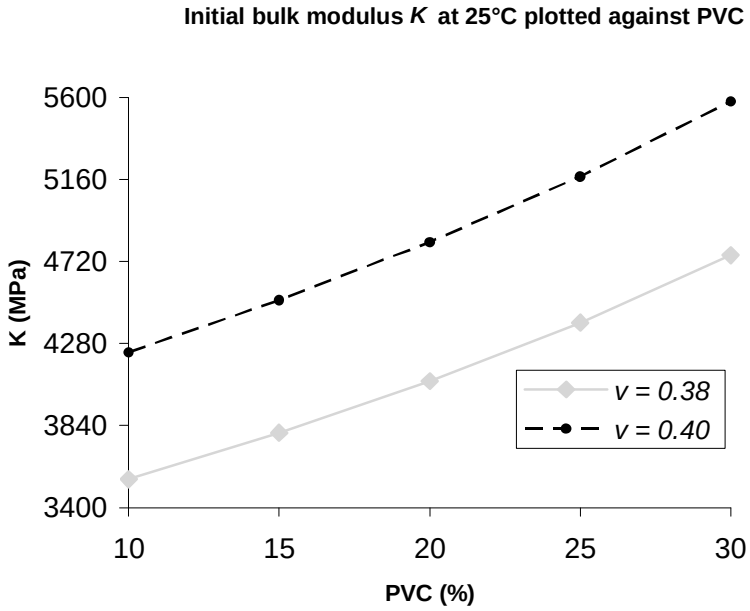

Figure I.2 Initial bulk modulus *K* at 25°C plotted against PVC

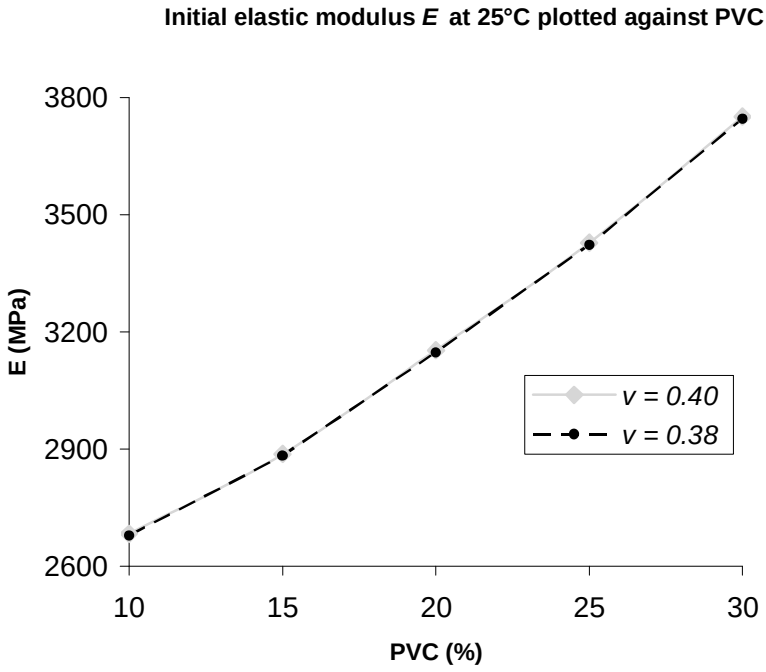

Figure I.3 Initial elastic modulus *E* at 25°C plotted against PVC

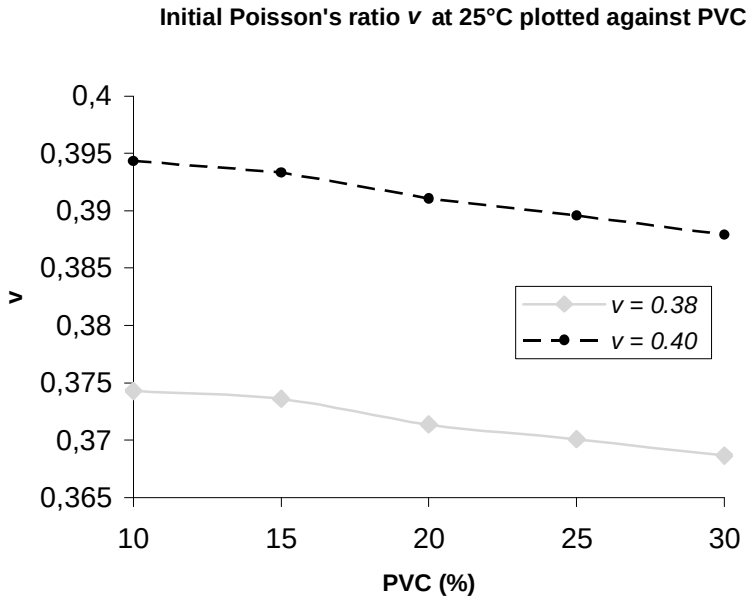

Figure I.4 Initial value of Poisson's ratio *v* at 25°C plotted against PVC

NOTATIONS

Symbols used throughout the report are listed. Complex nameless functions as well as variables used in certain places are defined where they appear. Variables are identified by italic type in the text and vectors by bold type.

Variables and symbols

a	measure of length
b	measure of length
c_{ij}	crystal elastic constant
e_{ij}	strain deviator
E	elastic modulus
E_i	arbitrary value in relaxation curve, elastic modulus / arbitrary spring, Generalized Maxwell model
E_0	initial value, elastic modulus
E_∞	relaxed (long-term) value, elastic modulus
G	shear modulus
G_i	arbitrary value in relaxation curve, shear modulus / arbitrary spring, Generalized Maxwell model
G_R	Reuss shear modulus
G_v	Voigt shear modulus
G_0	initial value, shear modulus
G_∞	relaxed (long-term) value, shear modulus
K	bulk modulus
K_R	Reuss bulk modulus
K_v	Voigt bulk modulus
K_0	initial value, bulk modulus
K_∞	relaxed (long-term) value, bulk modulus
l	length
r	radius
s_{ij}	stress deviator
t	thickness
u	arbitrary displacement
w	width
α	coefficient of thermal expansion
α_c	coefficient of thermal expansion for the composite
α_i	ratio between G_i and G_0, Generalized Maxwell model
α_m	coefficient of thermal expansion for the matrix

α_p coefficient of thermal expansion for the particle
ε_v relative volume change
ε_{ij} shear strain
η_i arbitrary damper, Generalized Maxwell model
v Poisson's ratio
v_0 initial value, Poisson's ratio
v_∞ relaxed (long-term) value, Poisson's ratio
σ arbitrary stress
σ_h hydrostatic stress
τ_i ratio between η_i and G_i, Generalized Maxwell model
τ_{ij} shear stress

Matrices and vectors

e strain deviator vector
s stress deviator vector
S compliance constants matrix

Abbreviations

CTE coefficient of thermal expansion
FE finite element
FEM finite element method
PVC particle volume concentration

GLOSSARY

Some technical terms that are used without further notice in the text are explained. Most terms are FEM-related and basic terms of solid mechanics are not handled. The explanations are cited from [23].

Boundary conditions

Those physical and/or mechanical conditions existing around the surfaces and limits of a structural body.

Compliance

The inverse of the stiffness in a uniaxial case, simply displacement divided by force.

Element

A separate and distinct structural element, one of many which together form a structural idealization or mathematical model of an actual continuous structure.

Fatigue

The phenomenon leading to fracture under repeated or fluctuating stresses having a maximum value less than the tensile strength of the material.

Finite element method (FEM)

An approximate numerical method for modeling and solving the engineering problems of mechanics. The system being solved is replaced by means of small interconnected parts (elements) whose stiffness, damping and inertia properties are expressed in matrix form.

Mesh

Subdivision of model geometry into elements.

Model

Computer based description of a problem to be analyzed.

Node

Vertices of elements that define the position of the element in 3D space; e.g. a node has x, y and z coordinates.